Electrostatic Bifurcation In-Plane Sensors

by

Mohamed Arabi

A thesis
presented to the University of Waterloo
in fulfillment of the
thesis requirement for the degree of
Doctor of Philosophy
in
Systems Design Engineering

Waterloo, Ontario, Canada, 2022

Examining Committee Membership

The following served on the Examining Committee for this thesis. The decision of the Examining Committee is by majority vote.

External Member: Yu Sun
Professor, Dept. of Mechanical & Industrial Engineering,
Canada Research Chair in Micro and Nano Engineering Systems,
University of Toronto

Internal-External Member: Alex Penlidis
Professor, Dept. of Chemical Engineering,
University of Waterloo

Internal Member(s):   Glenn Heppler
Professor, Dept. of Systems Design Engineering,
University of Waterloo

Parsin Haji Reza
Assistant Professor, Dept. of Systems Design Engineering,
University of Waterloo

Supervisor(s):   Eihab Abdel-Rahman
Professor, Dept. of Systems Design Engineering,
University of Waterloo

Mustafa Yavuz
Professor, Dept. of Mechanical and Mechatronics Engineering,
University of Waterloo

Author's Declaration

I hereby declare that I am the sole author of this thesis. This is a true copy of the thesis, including any required final revisions, as accepted by my examiners.

I understand that my thesis may be made electronically available to the public.

Abstract

Electrostatic MEMS sensors are known for their high sensitivity, wide range of operation, and quick response. These unique attributes give Electrostatic MEMS sensors an edge over other MEMS transduction mechanisms (electrothermal, piezoresistive, piezoelectric, electromagnet, etc.) in many applications. The nonlinearity encountered in electrostatic MEMS is frequently considered a disadvantage. But it can also become a huge advantage when put to intelligent use, such as the case with bifurcation detection mechanisms. In this research, electrostatic MEMS sensors are deployed to detect various physical quantities.

The motions of most MEMS sensors occur either in-plane, parallel to a ground plane or a substrate, or out-of-plane, perpendicular to it. In-plane sensors can alleviate the impact of the major damping source in MEMS, squeeze film damping. They can, therefore, provide higher quality factors than out-of-plane sensors. This is an advantage that has recently attracted interest. However, optical characterization of in-plane motions is challenging. We introduce a novel technique to measure both in-plane and out-of-plane motions of MEMS using a one-dimensional (out-of-plane) LDV. The technique's efficiency is demonstrated by evaluating an interdigitated comb-drive actuator's in-plane, out-of-plane modal response and frequency-response. We also investigate the validity of observing planar modes of vibration outside their dominant plane of motion and find that it leads to erroneous results. Planar modes must be evaluated in their plan of motion.

Various ideas have been proposed to improve the quality factor further and reduce the actuation voltage of in-plane sensors. We undertook a comparative experimental study of two of these approaches to investigate their impact on the actuation voltage and sensitivity of in-plane sensors. Namely, placing actuation electrodes on both sides of the sensor to reduce actuation voltage vs. one side only to reduce damping. To improve sensitivity, building the sensors out of stiffer solid beams or lighter cavitary beams was also investigated.

To investigate the effect of squeeze film damping on the behavior of electrostatic in-plane MEMS sensors, we solved the coupled nonlinear partial differential equations representing an electrostatically actuated sensor and a fluidic medium in the channel between the sensor and its actuation electrode. An Euler-Bernoulli beam model representing the sensor motions was coupled with a one-dimensional compressible Reynolds equation representing the fluid motions. The system was solved for the sensors in air and underwater using a Reduced Order Modeling approach.

To demonstrate the versatility of electrostatic in-plane MEMS sensors, they were deployed for three applications in this work, namely pressure sensing, gas sensing, and underwater sensing. First, a novel electrostatic bifurcation pressure sensor is introduced. The

sensor is made of a simple microstructure, cantilever, not diaphragm, that can easily be fabricated using a standard multiuser or a custom fabrication process. It does not need wafer bonding, sealing, or any complex microfabrication process to produce the pressure chamber. It overcomes the limitations of temperature in the other traditional diaphragm pressure sensors. Experimental results show that the electrostatic bifurcation pressure sensor has higher sensitivity and resolution than traditional MEMS diaphragm sensors.

Second, electrostatic bifurcation gas sensors were designed and fabricated to detect toxic gases in air. The sensors were functionalized using a new deposition technique and two detector polymers. The sensors were used to detect three VOCs: formaldehyde, benzene, and hydrogen sulfide. The gas sensors showed good sensitivity for all three gases and selectivity for a target gas (formaldehyde) in the presence of an interferent gas (benzene).

Finally, we present new bifurcation MEMS sensors to detect hazardous chemicals underwater. A special test chamber was fabricated to allow for testing the sensor underwater while measuring its response optically and electrically. The sensor was tested in air and underwater, and electrical measurements were recorded underwater. The results show that the sensor moves underwater, and two natural frequencies were observed, each represented by a $\sim 180°$ phase shift.

Acknowledgements

First and foremost, I would like to praise Allah, The Beneficent, The Merciful, The Watchful, The Provider, for His blessing given to me during my study and in completing this thesis. May Allah's blessing goes to His final Prophet Muhammad (peace be upon him), his family, companions, and followers.

I have been privileged to study in the Department of Systems Design Engineering for four years and Mechanical and Mechatronics Engineering for two years at the University of Waterloo. With gratitude, I acknowledge the following for their help and encouragement during this whole period:

My professors and thesis advisors, Dr. Eihab Abdel Rahaman and Mustafa Yavuz, Professors of Systems Design Engineering and Mechanical and Mechatronics Engineering, welcomed and supervised my research when I first came to the University of Waterloo. They kindly gave me the opportunity, guidance, financial support, and a generous allotment of time to start and complete this thesis. Dr. Abdel Rahman and Dr. Yavuz were always so kind and helpful, and they offered a lot of help when I was struggling in my research and personal life. Their deep and robust knowledge of MEMS sensors helped me proceed with my research and overcome all the challenges.

To my friends, who I always call brothers. Without my brothers, I wouldn't start or do anything. Sometimes I gave up on myself, but they never gave up on me. You were always encouraging, supporting, and motivating me. You were spreading your positive energy over everything. For my brothers I would like to say:

Thank you, Dr. Mahmoud Khater.
Thank you, Dr. Majed Al Ghamdi
Thank you, Dr. Ahmed Desoky
Thank you, Dr. Sangtak Park
Thank you, Dr. Resul Sartis
Thank you, Dr. Ayaman Sadoun
Thank you, Dr. Mohamed Eltaher.
Thank you, Dr. Abdallah Kabeel
Thank you, Dr. Mostafa Osman
Thank you, Dr. Ahmed Ali

I would also like to thank my committee members, Prof. Yu Sun, Prof. Alexander Penlidis, Prof. Glenn Heppler, and Prof. Parsin Haji Reza, for serving as my committee

members. I want to thank you for letting my defense be an enjoyable moment. Your close reading of my thesis and subsequent responses helped me make substantial improvements.

Finally, My ultimate and special thanks are due to my beloved family for the years of encouragement and support whenever necessary. You are the most precious thing in my life, and I love you all.

Dedication

To *Allah*, may You accept my work and make it beneficial for the others

To my *Father* and my *Mother*

To my Children *Rokia* and *Hamza*

Table of Contents

List of Tables

List of Figures

xvi

List of Abbreviations

List of Symbols

Chapter 1

Introduction

1.1   Electrostatic Bifurcation MEMS Sensors

MicroElectroMechanical Systems (MEMS) is a batch-fabricated microscale system that performs actuation or sensing functions. It can convert a physical quantity or event into mechanical motion or electrical signal and vice versa[1, 2]. The first known use of MEMS dates back to the early 1960s where MEMS sensors were fabricated from piezoresistive silicon to measure pressure and stress [3, 4, 5, 6].

MEMS can be used as an actuator or a sensor. In the case of using MEMS as a sensor, the physical quantity is converted to an electrical signal easily read out. The MEMS sensors have many applications such as accelerometers, gyroscopes, magnetometers, pressure sensors, flow sensors, temperature sensors, and gas sensors where the physical quantities measured are accelerations, angles, magnetic fields, pressures, flow rates, temperatures, and concentration of gases, respectively.

MEMS are transducers as they transfer the energy between at least two domains[7]. The transduction methods (actuation methods) in MEMS can be electrothermal, electromagnetic, piezoelectric, piezoresistive, and electrostatic methods [2]. While the sensing methods include the piezoelectric, piezoresistive, and electrostatic methods. The applications of using piezoelectric transactions include strain sensors [8], accelerometers [9], pressure sensors [10], density and viscosity sensing [11], and so on. The piezoresistive materials can be used to detect strain[8], temperature [12], humidity [13].

Electrostatic transduction is the most popular actuation and sensing method in MEMS [2]. The electrostatic force is generated when two parallel plates are connected to an electrical potential difference (capacitor). This force tends to attract the two plates causing

1

a change in the force, or displacement [2, 7]. These plates can be fabricated using any microfabrication method and do not require special material like the other transduction methods. Electrostatic transduction is fast and has low power consumption when compared to electrothermal transduction [2]. It doesn't need an external field source as the electromagnetic transduction[2]. Electrostatic sensing transforms the displacement resulting from the physical quantity into a change of the capacitance between the parallel-plate capacitor. In this research, we will use electrostatic transduction for the proposed sensors. Electrostatic MEMS sensors are widely used in many applications, such as accelerometers [14], gyroscopes [15], pressure [16] and gas sensing [17]

Sensing mechanisms in MEMS sensors can be classified into analog (quantitative measurement) and binary (qualitative measurement)[18, 19, 20]. In analog sensing, the sensor measures the change in the stimulus quantity and shows this change as a specific value on the sensor's scale. In contrast, the binary sensor acts as an ON/OFF switch. The sensor usually is OFF unless a threshold in the stimulant is reached, then it goes ON. To understand the difference between the two sensing mechanisms, we consider the binary and analog gas sensors. The analog gas sensor can detect the concentration of the target gas in the surrounding environment. The binary gas sensor detects the presence of the target gas at a specific concentration in the surrounding environment. Although the analog sensors continuously measure the change in the stimulus, the binary sensors have higher sensitivity. Khater et al. [19, 21] and Al-Ghamdi et al. [18] used binary gas sensors to detect very small concentrations of gases.

Bifurcation is defined as a change in the stable response of the system[22]. Bifurcation can be static where the equilibrium points change or dynamic where the attractors (stable periodic orbits) change [17, 20]. This change may be quantitative, where the number of the equilibrium points change, or qualitative, where the state of equilibrium changes. The bifurcation point is the point at which this change takes place. In MEMS, static and dynamic bifurcations detection can be used to improve the sensitivity of the sensors [17, 21]. Thus, we used the static and dynamic bifurcation mechanisms as the main detection mechanism in this research.

1.2   In-plane MEMS Sensors

By definition, MEMS structures have a mechanical motion. The MEMS motion may be out-of-plane, in-plane, or a combination of both motions (3D). Figure 1.1 shows in-plane and out-of-plane comb-drive actuators as MEMS devices. Typically, Electrostatic MEMS sensors are designed to move out-plane, perpendicular to the substrate. The layer-by-layer

2

nature of surface micromachining serves this actuation mode well. It enables the creation of large-area parallel-plate capacitors to serve as actuators, thereby reducing actuation voltage requirements. Conversely, the typical thin layers of this microfabrication approach put in-plane actuation, where the motion direction is parallel to the substrate, at a disadvantage since they result in a small capacitor (actuator) areas and prohibitively high actuation voltages.

(a) In-plane comb-drive actuators

(b) out-of-plane comb-drive actuators
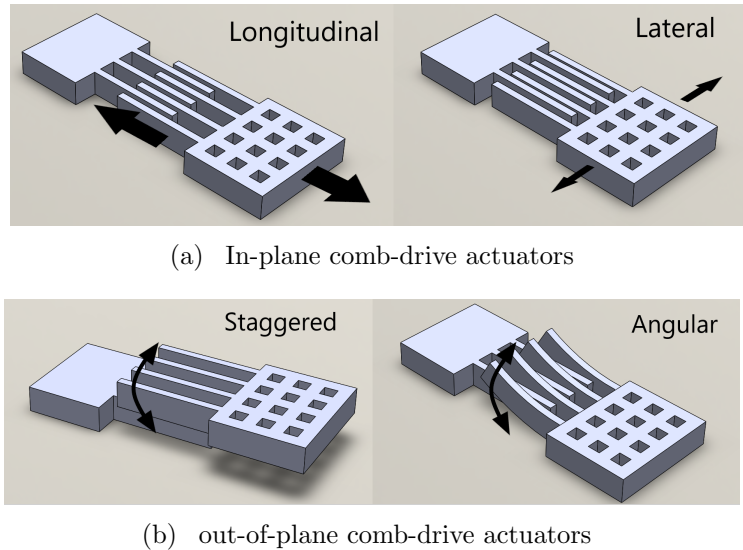
Figure 1.1: In-plane and out-of-plane MEMS structures (comb-drive actuators)

As a result, out-of-plane MEMS have seen a lot more interest than in-plane MEMS. However, squeeze film damping due to the air cushion between MEMS structure and the substrate may be developed for out-of-plane MEMS structures [2, 23]. Squeeze film damping is known as the major damping source in the out-of-plane MEMS structures [23, 24, 25, 26, 27]. To reduce the chance of squeeze film damping generation, the substrate beneath the beam may be etched away, creating holes in the movable plate [24] or vacuuming the MEMS encapsulation. The first option is not available for most standard microfabrication processes while creating holes might not be possible for some designs. Vacuum encapsulation has been successfully used to protect accelerometers, gyroscopes, and magnetic field sensors against those energy losses, but it is not feasible for gas and fluidic sensors.

In-plane MEMS sensors have emerged as an alternative to overcome this difficulty [25, 28, 29]. Instead of acting against the air (or other fluid) column, they shear it and,

thereby, reduce energy losses. They also use Silicon on Insulator (SOI) fabrication processes to obtain a large structural layer that can increase the actuator area and, therefore, reduce the actuation voltage.

Testing the out-of-plane MEMS structures optically is well established; however, it is not the case in the in-plane structures. We are developing a new technique to measure the in-plane motions optically using a typical Laser Doppler Vibrometer (LDV), so the full range of the experimental work can be conducted.

1.3 Applications of Electrostatic Bifurcation In-Plane Sensors

We selected three applications to demonstrate the capabilities of electrostatic bifurcation in-plane MEMS sensors: pressure, gas, and underwater sensing. Pressure sensing is one of the original applications for which MEMS were developed [4, 5, 30]. In 1962, Tufte et al. [4] published their work on the first MEMS, made of a thin piezoresistive Si diaphragm, for pressure sensing. Capacitive pressure sensors were first introduced by Sander et al. of the Stanford Integrated Circuits Lab to improve the sensitivity and stability that is possible with piezoresistive pressure sensors [5, 31]. We introduce an electrostatic bifurcation in-plane pressure sensor. We used the cyclic-fold bifurcation as the detection mechanism of the proposed sensor.

Air, water, and soil are the main ingredients of our environment. This environment provides organisms like humans, animals, plants, etc., essential needs to live. Without a secure environment, these organisms will be in danger. The effects of an unsecured climate can be severe and lethal. Pollution is the primary source of danger to our environment. Pollutants can be produced from natural or human-made sources. Natural sources of pollutions include volcanic eruptions and forest fires. Transportations, industry, power generation, construction, etc., are the main human-made contributors to polluting our environment. They produce toxic gases that spread in air in addition to hazardous chemicals that dissolve in water. Consuming polluted air or water harms the organisms, so detecting these pollutants becomes necessary to secure our environment.

A system of sensors that are placed in air and underwater is required to monitor the environment. MEMS-based sensors can detect minimal concentrations of toxic gases. In this research, we used electrostatic bifurcation MEMS sensors to detect Volatile Organic Compounds (VOCs) in air and mercury underwater.

4

1.4 Scope

This research aims to study, design, and use electrostatic bifurcation in-plane MEMS sensors where static and dynamic bifurcations were considered detection methods. The structure of this thesis can be sectioned into two main parts, fundamentals and applications. In the fundamentals, we study and investigate the ability and feasibility of using in-plane sensors, Chapter 2, 3, and 4. The second part is the possible applications of the electrostatic bifurcation in-plane MEMS sensors, Chapter 5, 6, 7.

In Chapter 2, we present a new technique of measuring in-plane motion optically and prove its validity. The considerations and limitations of the method are discussed. The designing concepts and considerations of the electrostatic bifurcation in-plane MEMS sensors are discussed in Chapter 3. A coupled system of nonlinear partial differential equations was solved using Reduced Order Modeling (ROM) to investigate the effect of squeeze film damping on the electrostatic bifurcation in-plane MEMS sensors behavior in Chapter 4.

A novel electrostatic bifurcation in-plane pressure sensor that uses the tapping mode oscillation as a dynamic bifurcation detection mechanism is introduced in Chapter 5. Chapter 6 demonstrates using static bifurcation gas sensors to detect three VOCs in a dry nitrogen environment. The sensors were designed to move out-of-plane. A new method to functionalize the sensor with two detector polymers is introduced. We investigate the minimum detectable concentrations of the VOCs as well as the detection of a target gas in the presence of an interferent gas.

Developing an electrostatic bifurcation underwater sensor requires considering the huge damping added to the system due to working in a higher viscous fluid (water). In chapter 7, we introduced the design concepts and the basic characterization of an electrostatic bifurcation underwater sensor that will be used to detect mercury in water. The chapter also shows the experimental setup for testing the sensor underwater. Chapter 8, summarizes the main outcomes of this research, and it also introduces future work.

1.5 Contributions

The author of this thesis gratefully acknowledges the contributions of many collaborator who made this work possible. Specifically:

- Prof. Raafat Mansour and Mr. Matthew Ou, Centre for Integrated RF Engineering (CIRFE), University of Waterloo, fabricated the electrostatic bifurcation in-plane

Chapter 2

Measurement of In-Plane Motions

The dimensions of MEMS preclude the use of traditional inertial sensors, such as accelerometers, to measure their motions. Although electric parameters, such as capacitance [32] and current [33] can be employed to estimate the motions of MEMS indirectly, they have limitations. To begin with, separating features in the measured signal due to motions from those due to electric circuit interactions is nontrivial. Even where that is possible, the measured signal represents an integral-type estimate of the overall structure motion rather than a point-wise measurement of motion. As a result, the gold-standard for MEMS motion measurements has been non-contact optical techniques, such as LDV [34] and Digital Image Correlation (DIC) [35, 36].

Typical LDV detects out-of-plane motions by measuring the Doppler effect, the difference between the frequencies of the incident, and reflected laser beams at a surface point [35, 37] moving along the same direction. It can not detect in-plane motions because they do not result in a Doppler effect. Various techniques have been proposed to overcome this limitation and use LDV to measure the in-plane motions. They can be classified into on-axis, and off-axis techniques [38].

On-axis approaches place the incident laser beam and the photodetector receiving the reflected beam along an axis aligned with in-plane motions [38]. The main drawback of this technique is the complexity of the experimental setup required to access the sidewalls of moving MEMS. Further, the lack of an objective lens makes this approach feasible only for larger MEMS. Turner et al. [39] overcame these limitations by fabricating a 45° micromirror on the same substrate as the MEMS under-test to gain optical access to the side walls using a standard single-axis LDV. This approach requires significant fabrication capabilities not available in many standard microfabrication processes, and it also involves

substrate footprint to equip each MEMS under-test with a dedicated micromirror.

Off-axis approaches use photodetectors placed at an angle with respect to the incident laser beam. In 3D LDV [40, 41], an incident laser beam is directed at the top surface of a moving structure. At the same time, one photodetector is placed on-axis to measure out-of-plane motion, and two photodetectors are placed off-axis to measure in-plane motions [42]. This method allows for simultaneous measurement of in-plane and out-of-plane motions. However, it is a rather expensive technique, and the experimental setup is inflexible. Also, the measurement area and the maximum displacements that can be captured are limited.

A more complex off-axis approach deploys three single-axis LDVs at different angles with respect to a common surface to measure three velocity vectors and calculate its 3D motions out of them [42, 43]. Its main drawback is optical cross-talk between the three laser beams [42] which is hard to avoid at the microscale.

DIC measures in-plane motions using image processing techniques [35]. However, the bandwidth and resolution of its measurements are inferior to those of LDV. Therefore, it is desirable to develop methods to measure in-plane motions using single-axis LDV. This chapter demonstrates a simple and flexible method to measure in-plane motions using a standard single-axis LDV.

2.1   Methods

The Device-Under-Test (DUT) used in this study was a 59-finger comb-drive actuator fabricated using a single mask SOI fabrication process carried out at the QNFCF, University of Waterloo [44]. The wafer handle layer is $500\,\mu$m thick, the thermal oxide layer is $1\,\mu$m thick, and the device layer is $20\,\mu$m thick. The rotor is composed of 59 comb fingers and a backbone mass connecting by two crab-leg springs to two posts on either side of the center-line as shown in Figure 2.1. Each crab-leg spring has four beams $250\,\mu$m long and $3\,\mu$m wide.

Modal analysis was carried out on a model of the comb-drive actuator using FEM. SolidWorks software was used to determine the natural frequencies and mode shapes of the DUT. The first seven natural frequencies were found to correspond to four in-plane and three out-of-plane modes. The fundamental mode is an in-plane mode appearing at a natural frequency of $f_{i,1}$=5.1 kHz where the backbone mass translates in-plane (along the z-axis) and the actuator behaves as a longitudinal comb-drive, Figure 2.2(a). In the second and third in-plane modes, at $f_{i,2}$=33.5 kHz and $f_{i,3}$=34.4 kHz, the crab-leg springs move out-of-phase and in-phase, respectively, while the backbone mass remains almost

8
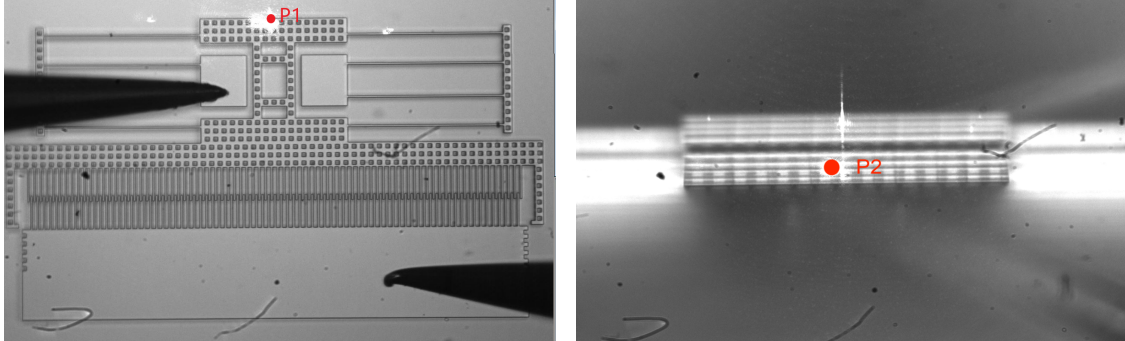
(a) Top view of the comb-drive. The red dot indicates the location of the laser beam spot while measuring out-of-plane

(b) Front view of the comb-drive. The red dot indicates the location of the laser beam spot while measuring in-plane

Figure 2.1: Top and front views of the comb-drive actuator

stationary, Figures 2.2(c) and (d). In the fourth in-plane mode, $f_{i,4}$=73 kHz, the springs and backbone mass move relative to the posts, Figure 2.2(f).

In the first ($f_{o,1}$=17 kHz) and second ($f_{o,2}$=57.4 kHz) out-of-plane modes, the backbone mass rotates about the x-axis and z-axis as shown in Figures 2.2 (b) and (e), respectively. In the third out-of-plane mode ($f_{o,3}$=84.3 kHz), the crab-leg springs bend out-of-plane along the y-axis. Simultaneously, the rotor-side of the comb finger rotates around the x-axis to move in the same direction.

Figure 2.3 (a) shows the working principle of typical LDV where the out-of-plane MEMS structure and incident laser waveforms are represented with dashed lines. The solid lines represent the final position and reflected laser waveform after the out-of-plane structure was displaced by x downward. The velocity of the sensor can be evaluated from the change in frequency between the incident and reflected laser beams.

MEMS moving in-plane, Figure 2.3(b), do not produce a frequency change and therefore their in-plane velocity cannot be measured. In principle, those motions can be measured by rotating the substrate by 90° to make sidewall motions appear out-of-plane to the LDV. However, this requires a clear line of sight to the moving wall unobstructed by other MEMS or anchors on the substrate.

Instead, we demonstrate a more practical method to measure in-plane motions regardless of the availability of a clear line of sight. A stage was designed and fabricated to hold the MEMS chip at an arbitrary angle with respect to the incident laser beam, as shown

(a) 1st in-plane mode shape at 5.1 kHz

(b) 1st out-of-plane mode shape at 17 kHz

(c) 2nd in-plane mode shape at 33.5 kHz

(d) 3rd in-plane mode shape at 34.4 kHz

(e) 2nd out-of-plane mode shape at 57.4 kHz

(f) 4th in-plane mode shape at 73 kHz

(g) 3rd out-of-plane mode shape at 84.3 kHz
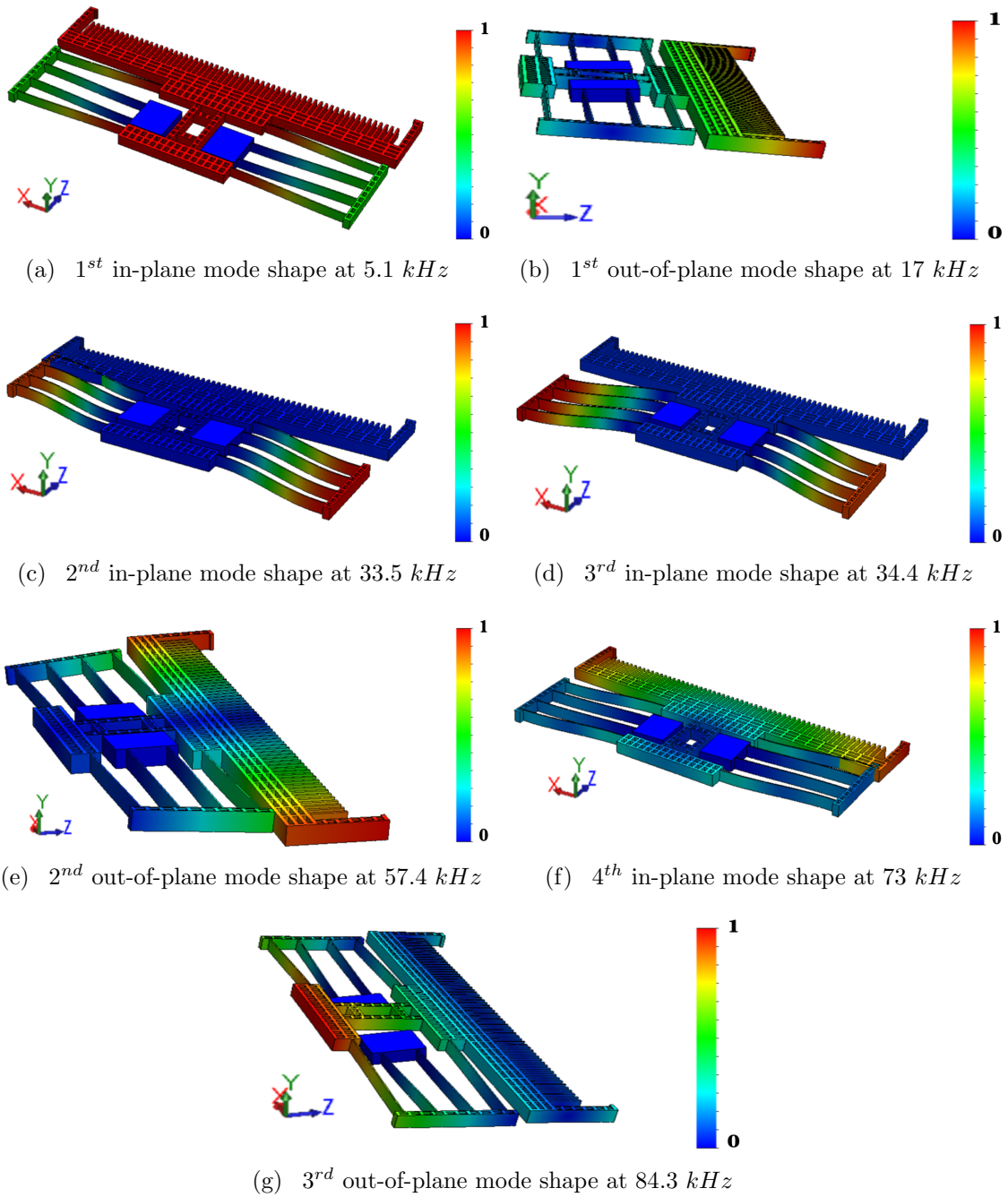
Figure 2.2: Mode shapes of the comb-drive actuator

10

schematically in Figure 2.3(c). The incident laser beam on the moving wall is reflected to the substrate, which reflects it back to the objective lens.

The tilt angle of the stage with respect to the horizontal is dubbed ϕ. The laser incidence angle on the sidewall equals ϕ. As the laser beam is reflected from the wall to the substrate, its incidence angle on the substrate is $\theta = 90° - \phi$. As a result, the laser beam reflected from the substrate to the objective lens will be parallel to the initial incident beam and vertical with respect to the horizontal. This setup is designed to maximize the intensity of the laser beam reflected into the objective lens, thereby maintaining the accuracy of measurements.

The relationship between the actual in-plane displacement x and the apparent displacement $\bar{x}$ measured by the LDV, Figure 2.3(c) and (d), measured by the LDV, can be derived as:

$$\bar{x} = x_2 + x_3 + x_5 - x_1 \tag{2.1}$$

where x_1 is the distance traveled by the laser beam at time instant t_{i-1} (original position) and $(x_2 + x_3 + x_5)$ is the distance traveled by the laser beam at time instant t_i (new position).

From the geometries of the incident and reflected laser beams interaction with the structure and substrate, respectively, we can find that:

$$x_1 = x_2 + x_3 \quad \Rightarrow \quad \bar{x} = x_5 \tag{2.2}$$

Therefore, the apparent displacement is equal to x_5. It can be calculated from the hatched triangles in Figure 2.3(c) as:

$$\bar{x} = x_4 \sin \phi$$
$$\frac{x_4}{\sin 2\phi} = \frac{x_2}{\sin \theta} \tag{2.3}$$

The in-plane displacement x can be related to x_2 by:

$$x = x_2 \sin \phi \tag{2.4}$$

Using Eq. (2.3) to substitute into Eq. (2.4), we find that:

$$x = \frac{\cos \phi}{\sin 2\phi} \bar{x} \tag{2.5}$$

where $(\cos \phi / \sin 2\phi)$ is the displacement correction factor. Figure 2.4 shows variation of the displacement correction factor with the tilt angle ϕ. In the case of measuring velocity,

(a) out-of-plane
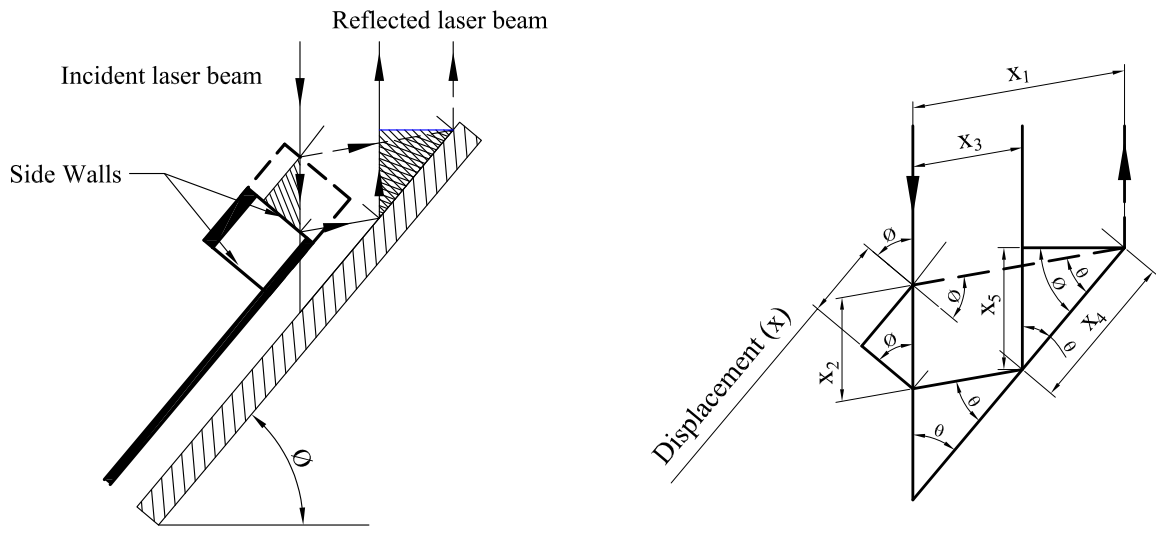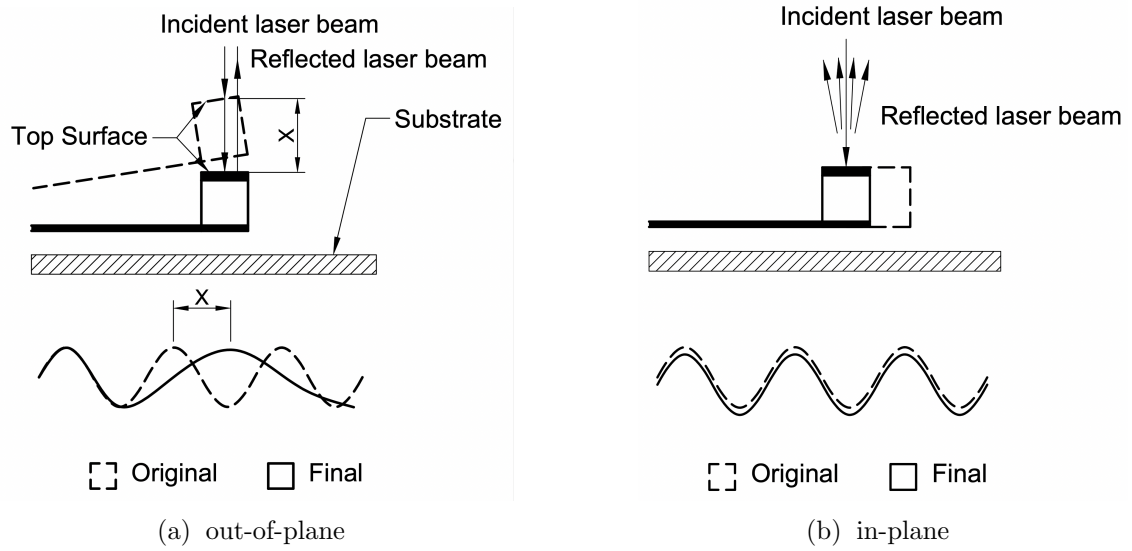
(b) in-plane

(c) Chip placed at an angle ϕ with repect to the horizon

(d) Relationship between displacement and apparent displacement

Figure 2.3: Measurement of in-plane motions

the LDV detects changes in the reflected laser beam frequency rather than changes in the length of the laser beam path. Consequently, the velocity correction factor is $(\sin \phi)$.
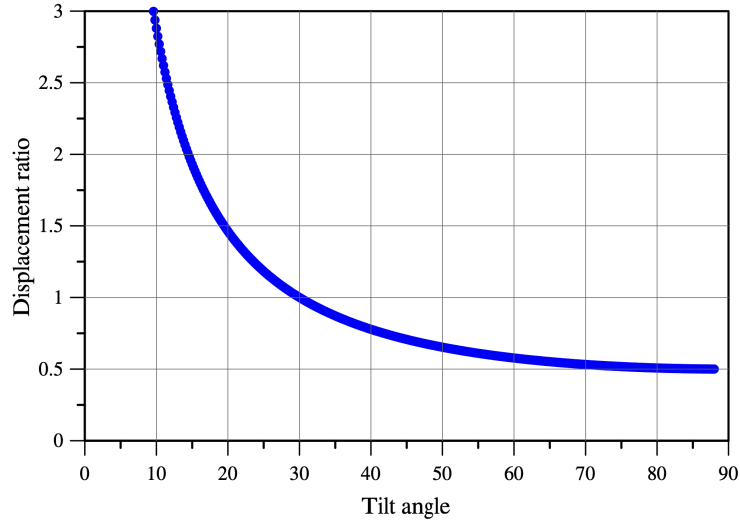
Figure 2.4: Variation of the displacement correction factor with the tilt angle ϕ

While Eq. (2.5) does not exclude the small tilt angles ϕ, it is impractical to use small angles because the reflected laser beam tends to be far from the incident laser beam. In this case, two possibilities are expected; the reflected laser beam might be interrupted by another structure or goes out of the objective lens. The same observation holds for the large angles closer from 90° where we lose the line of sight because other structures on the same chip may block the access to the sidewalls. Therefore we recommend using tilt angles between 45° and 75° to ease the measurement of the in-plane motions.

The point marked P1 in Figure 2.1(a) shows the location of the laser beam target used to measure the actuator's out-of-plane motions. It is located on the top surface of the midpoint along the back edge of the backbone. Its in-plane velocity lies at a right angle with respect to the incident laser beam rendering it unobservable by the LDV. The incident laser beam is focused at point P2 to observe the in-plane motions, Figure 2.1(b). It is located at the midpoint of the back edge's side wall, right below point P1. To gain access to point P2, the chip was tilted 70° with respect to the horizon as shown in Figure 2.5. Similar to the previous case, out-of-plane motions are unobservable by the LDV since they do not change the laser beam path length.

13
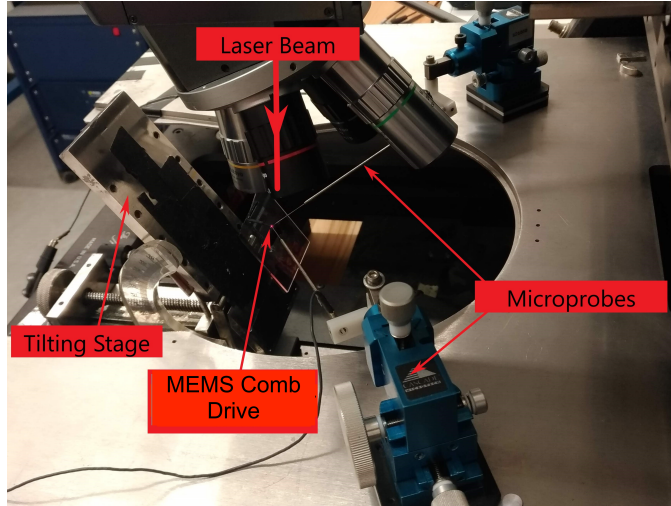
Figure 2.5: Experimental setup for in-plane measurements

2.2 Results

The velocity response of the DUT was investigated using MSV-400 from Polytec [45]. We obtained the comb-drive's out-of-plane and in-plane modal responses by observing the velocity of points P1 and P2, respectively, under a train of 75 V pulses with a frequency of 200 Hz and a duty cycle of 75%. The Fast Fourier Transforms (FFT) of the measured velocities are shown in Figure 2.6 in blue for point P_1 and orange for point P_2. Since these points are located at the back edge of the backbone, only those with pronounced motions were observable, namely the first in-plane bending mode and the third out-of-plane bending mode.

The first peak at $f_{i,1}$=5.1 kHz, observed in in-plane motions only, corresponds the first in-plane mode shown in Figure 2.2(a). The second peak at $f_{o,3}$=75.5 kHz, observed in out-of-plane motions only, corresponds to the third out-of-plane mode shape, Figure 2.2(g). The other mode shapes were not observed because they do not produce significant motions at the back edge of the backbone where points P_1 and P_2 are located. We note that the velocity amplitude of the first in-plane mode 108 mm/s is much higher than that of the third out-of-plane mode 1.8 mm/s. A third peak was observed in-plane at 81 kHz, corresponding to a coupling between the two active modes.

The frequency-response of the comb-drive was found by grounding the rotor and ap-
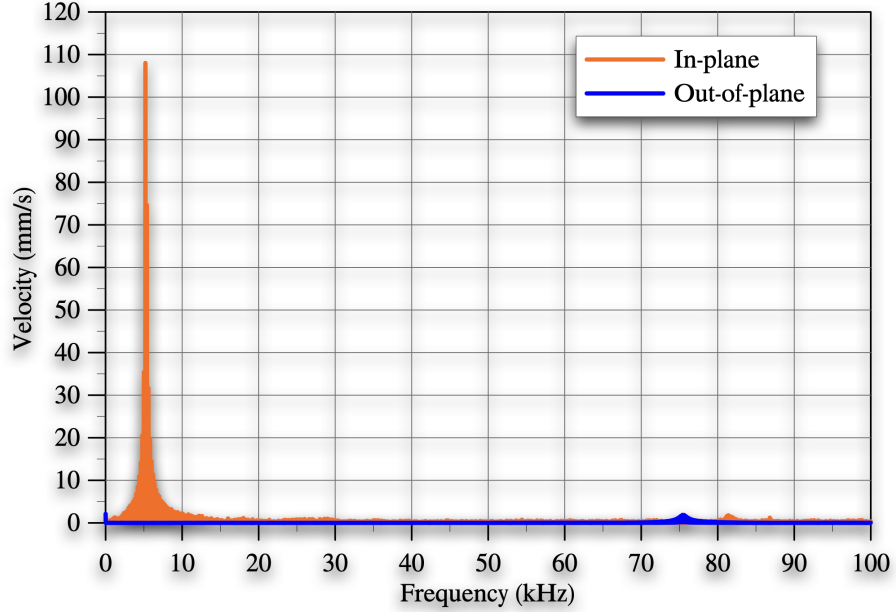
Figure 2.6: FFT of the measured out-of-plane and in-plane velocities of the back edge under a pulse train with an amplitude 150 V, $f = 200$ Hz, and a duty cycle of 1%

plying a unity modulation index $m_i = 1$ voltage signal to the stator

$$V(t) = V_\circ + V_\circ \cos(\Omega \ t) \tag{2.6}$$

where $V_\circ$ is the signal bias, amplitude, and Ω is the signal frequency. The LDV was used to record the time-history of the out-of-plane velocity (point P_1) and the in-plane velocity (point P_2) as the signal frequency was swept through the frequency range of interest. Frequency-response curves were constructed by evaluating the Root Mean Square (RMS) of the velocity over windows of 100 signal periods as a function of frequency.

Figure 2.7 shows the out-of-plane and in-plane frequency-response curves of the actuator under the excitation waveform $V_\circ = 7.5$ V as the frequency is swept from 2 kHz to 9 kHz. The peak of the in-plane frequency-response curve appears at $f_{i,1}=4.9$ kHz corresponding to the natural frequency observed in the modal analysis test, Figure 2.6. On the other hand, the peak of the out-of-plane frequency-response curve appears at 4.3 kHz. We also note that the Signal-to-Noise Ratio (SNR) of the in-plane frequency-response curve is higher, with the peak reaching 178 mm/s, than that of the out-of-plane curve, where the peak is 3 mm/s.

15

While the peak of the out-of-plane curve can still be resolved accurately, it would be erroneous to conclude that it corresponds to the resonance of the first in-plane bending mode. In fact, the out-of-plane curve drops to a minimum at the correct resonance frequency $f_{i,1}$=4.9 kH. This is expected since the out-of-plane frequency-response measures spurious motions associated with the in-plane mode. As a result, it drops towards a minimum at the impedance of the in-plane mode approaches a minimum at its resonance, thereby absorbing the energy in the actuator.
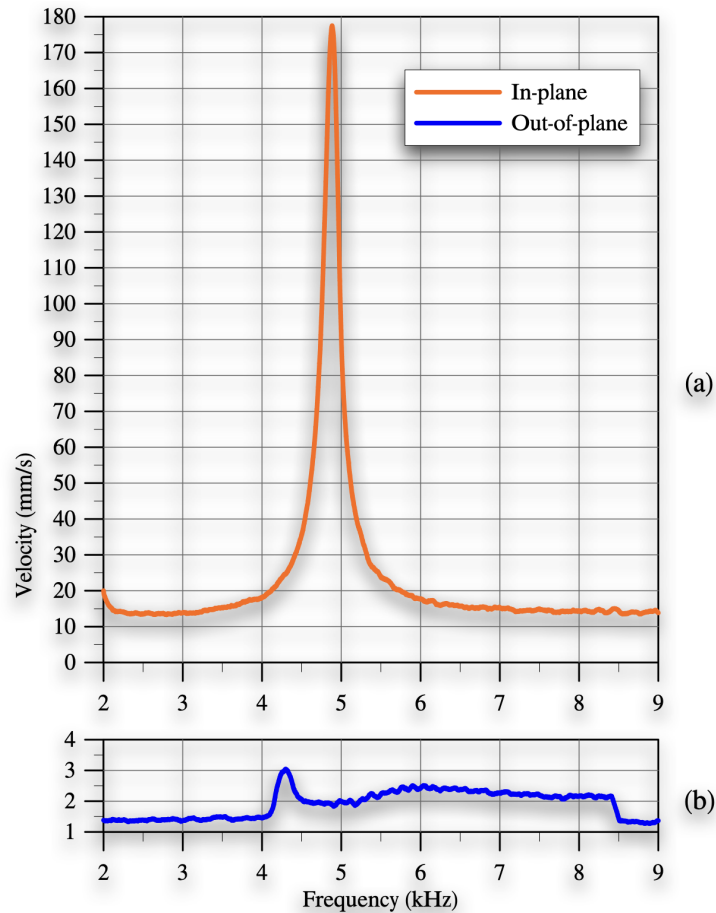
Figure 2.7: Frequency-response curves of the actuator under the excitation waveform $V_{\circ}$ = 7.5 V as the frequency is swept from 2 kHz to 9 kHz. (a) in-plane measurements, and (b) out-of-plane measurements

The frequency-response curves of the third out-of-plane bending mode under the same

excitation waveform were determined by sweeping the signal frequency from 75 kHz to 85 kHz, Figure 2.8. The velocity peak appears at 81.5 kHz in the out-of-plane curve, while the in-plane curve peak is found at 79.7 kHz. Both peaks appear at a higher frequency than that observed ion modal analysis at $f_{o,3}$=75.5 kHz. The out-of-plane motions of the comb fingers within the electrostatic field imposed by the voltage waver form are responsible for that stiffening effect [46].

The two peaks observed in out-of-plane and in-plane frequency responses offer competing estimates of the natural frequency. One of them only is correct since they are two observations of the same motion. Since the in-plane response, in this case, represents spurious motions associated with the out-of-plane mode, we conclude that the correct natural frequency under this voltage waveform is $f_{o,3}$=81.5 kHz. The fact that the SNR ratio of the out-of-plane frequency-response curve, where the peak reaches 101 mm/s, is higher than that of the in-plane frequency-response curve, where the peak reaches only 28 m/s, further confirms this fact.
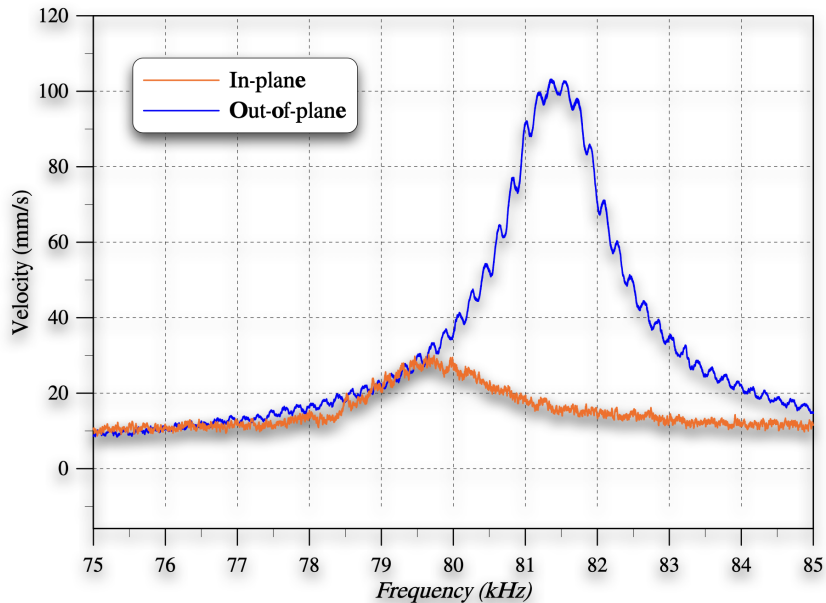
Figure 2.8: Out-of-plane and in-plane measurements of the frequency-response curves of the actuator under the excitation waveform $V_o = 7.5$ V as the frequency is swept from 75 kHz to 85 kHz.

2.3 Conclusions

We demonstrated a technique to measure in-plane motions of MEMS actuators using a typical out-of-plane LDV. It employs a tilt stage to align the sidewalls of MEMS actuators with the incident laser beam. Specifically, we demonstrated the deployment of our technique to measure modal response and frequency-response in-plane successfully.

Further, we compared the validity of using in-plane and out-of-plane measurement techniques to detect predominantly planar response modes. We found that measuring the response of a mode in a plane where it is not active leads to inferior and misleading results. The motions associated with a planar mode that appear outside its dominant plan are spurious, related to fabrication or actuation misalignments. As a result, they are not only small compared to those occurring in the primary plane of motion but also approach a minimum as the frequency of excitation approaches the natural frequency of the mode, thereby concentrating the actuator response in its dominant plane of motion. Therefore, predominantly planar modes should only be observed in their dominant plane. The measurement technique proposed here allows us to achieve that regardless of the plane of motion.

Chapter 3

In-Plane Sensor Design

The design of electrostatic in-plane MEMS is still an emerging field, and the state-of-the-art is still unsettled. Various ideas are being tried to improve the quality factor further and reduce the actuation voltage of in-plane gas and fluidic sensors. In this chapter, we undertake a comparative study of two of these approaches, namely placing actuation electrodes on both sides of the sensors (double-sided actuation) to reduce actuation voltage by strengthening the electrostatic field or just one side (one-sided actuation) and building the sensors out of stiffer solid beams or lighter cavitary beams to improve sensitivity. We investigate the impact of those design approaches on the quality factors and sensitivity of in-plane sensors experimentally.
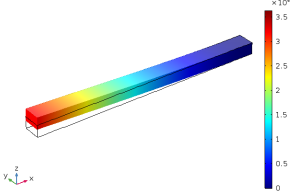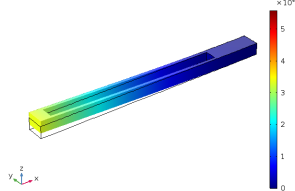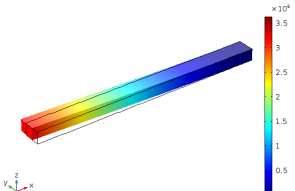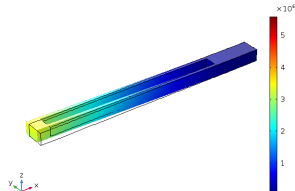
3.1 Methods

3.1.1 Sensor Design

SOI wafers, device layer thickness $30\,\mu$m, a buried oxide layer thickness of $2\,\mu$m, and a handle layer thickness of $400\,\mu$m, were used to fabricate the in-plane sensors. All sensors were designed as microcantilevers with the exact gross dimensions: $400\,\mu$m in length, $30\,\mu$m in width, and $23\,\mu$m in thickness. Four sensor variants were designed: solid one-sided actuation sensors, cavitary one-sided actuation sensors, solid double-sided actuation sensors, and cavitary double-sided actuation sensors. The etched cavities were $370\,\mu$m long, $12\,\mu$m wide, and $15\,\mu$m deep. Modal analysis was carried out on the solid and cavitary sensor variants using COMSOL software to predict their natural frequencies and

mode shapes. The first out-of-plane and in-plane natural frequencies and mode shapes are shown in Table 3.1.

Table 3.1: FEM predicted first out-of-plane and in-plane modes of the solid and cavitary sensors.

	Solid Sensor	Cavitary Sensor
1st out-of-plane mode	$f_{s,o}$=167 kHz,	$f_{c,o}$=183 kHz
1st in-plane mode	$f_{s,i}$=250 kHz,	$f_{c,i}$=292 kHz

3.1.2 Sensor Fabrication

The device layer is made of crystal silicon heavily doped with Arsenic, resistivity less than $0.005\,\Omega$/cm. The handle layer is made of highly resistive polysilicon for electrical isolation of the fabricated devices. A sidewall metal plating technique was developed and integrated into the fabrication process to provide step coverage on the high aspect ratio of the in-plane sensors. Sidewall metalization is a critical feature to minimize dielectric charging once the sensor beam and side electrode come into contact upon pull-in. In the absence of metalization, pull-in events result in leakage current and accumulated charges on the native oxide layer covering both walls, which changes the sensors' bias voltage, thereby undermining their reliability and the repeatability of detection.

Figure 3.1 shows steps of the fabrication process flow for in-plane sensors on a SOI., $40\,\mu$m wide sensor beams were released by controlled HF etching. They can be summarized in four key steps: (a) Starting with an SOI substrate Piranha/RCA cleaned and
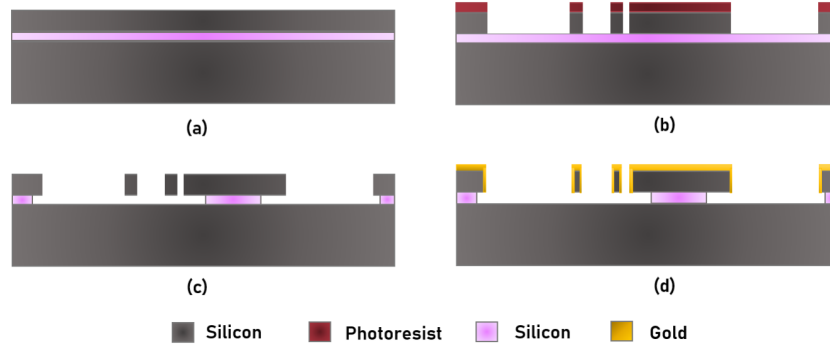
Figure 3.1: Fabrication process flow for in-plane sensors on an SOI substrate

dehydrated; (b) the device layer was first patterned and etched by Deep Reactive-Ion Etching (Si-RIE); (c) photoresist was stripped by O_2 ashing and the buried oxide was removed by controlled HF etching to release the device. Critical point drying in LCO_2 was used to dry the samples to minimize stiction. (d) Finally, a thin film of TiW was used as an adhesion layer followed by deposition of a gold (Au) layer on the top and vertical surfaces of the sensors. Since E-beam evaporation is not suitable for vertical wall coverage, a slow physical vapor deposition process was employed in this step.

3.1.3   Sensor Characterization

Initial characterization of fabricated sensors was carried out using a Scanning Electron Microscope (SEM) and a white light profilometer to ensure that there were no fabrication defects. Because the Au layer covered the surfaces of the chip, an electrical conductivity test was performed on the sensors to reject devices where a short circuit has developed between the sensor and actuation electrodes.

The sensor motions were measured optically using an LDV, MSV-400 from Polytec [45]. Out-of-plane and in-plane modal responses were obtained by placing the sensors in a vacuum chamber at 0.005 mbar. The quality factor is high enough to allow mechanical-thermal noise to act as white noise excitation at this pressure level. We followed the procedure described in Chapter 2 to measure the in-plane motions. The chip was tilted at a 60° angle with respect to the horizontal plane, and the LDV laser beam was focused at the tip of the sensor's sidewall.

The frequency-response curves of the sensors in air were obtained using two waveforms. The first is a white noise voltage signal. The second is a harmonic voltage signal (Eq. 2.6)

where the bias and amplitude of the waveform are held constant at $V_\circ = 10\,\text{V}$ while the excitation frequency Ω is swept with a slew rate of $20\,\text{kHz/s}$. Both waveforms were applied to one sidewall electrode only. For double-sided sensors, the second sidewall electrode and the sensor were held at the same voltage. The last step was undertaken to maintain the electrostatic field constant across all four sensor variants and allow for an equal comparison among them.

In both techniques, the time-domain data was collected using a real-time oscilloscope. RMS was calculated from the collected data using a dedicated mathematical code designed for this purpose. The frequency-response curves were generated at a resolution of $10\,\text{Hz}$. The half-power bandwidth method was used to estimate the quality factor of each mode from the frequency-response curves as:

$$Q = \frac{f_n}{\Delta f} \tag{3.1}$$

where f_n is the natural frequency and Δf is the half-power bandwidth. The resonant in-plane response of the sensors was also measured by applying five excitation levels of the harmonic voltage signal shown in Eq. 2.6, namely $V_\circ = 2, 4, 6, 8,$ and $10\,\text{V}$, with the excitation frequency set equal to their respective natural frequency $\Omega = \omega_{n,1} = 2\pi f_{n,1}$.

3.2 Results

Characterization showed the sensors were fully released with no visible downward deflection; hence the devices were free of stiction post-release. SEM images of a solid one-sided sensor and cavitary double-sided sensors are shown in Figures 3.2 (a) and (b). Using the SEM images, the thickness of the Au layer on the top surfaces was estimated as $370\,\text{nm}$. On the sidewalls, it was estimated to vary from a minimum of $116.3\,\text{nm}$ to a maximum of $164.1\,\text{nm}$.

Figure 3.3 shows the out-of-plane modal response for samples from each of the four sensor types; a FFT of the beam tips out-of-plane velocity under mechanical-thermal noise excitation in a vacuum. The natural frequency of the solid double-sided sensors was found to be $f_{s,d,o}{=}206\,\text{kHz}$, Introducing the cavity increased the natural frequency to $f_{c,d,o}{=}217.06\,\text{kHz}$, . The natural frequency of the solid one-sided sensors was found to be $f_{s,n,o}{=}208\,\text{kHz}$. Introducing the cavity increased the natural frequency to $f_{c,n,o}{=}219\,\text{kHz}$.

The in-plane frequency-response curves of the solid one-sided and double-sided sensors and the cavitary one-sided and double-sided sensors under white noise excitation are shown
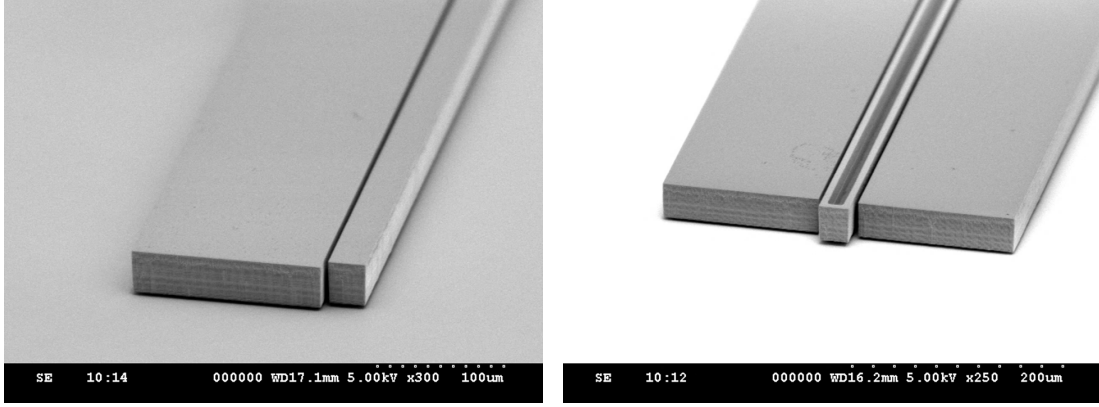
(a) solid one-sided　　　　　　　(b) cavitary double-sided

Figure 3.2: SEM images of SOI sensors showing the high aspect ratio of the capacitive gap between the sensor beam and side electrodes

in Figures 3.4 (a) and (b), respectively. The fundamental in-plane natural frequency of the cavitary one-sided sensor was found to be $f_{c,n,i}$=240.94 kHz while that of the cavitary double-sided sensor was $f_{c,d,i}$=239.56 kHz. The fundamental in-plane natural frequency of the solid one-sided sensor was $f_{s,n,i}$=217.88 kHz while that of the double-sided sensor was $f_{s,d,i}$=218.75 kHz.

We note that the response curves of the one-sided sensors are higher than those of the double-sided sensors throughout the frequency domain, indicating that the one-sided sensors have lower damping than the two-sided sensors. At the resonant peak, the cavitary sensors' response is higher by 13.56 μm/s under one-sided actuation compared to double-sided actuation. Similarly, the solid sensors' response is higher by 10.1 μm/s under one-sided actuation than double-sided actuation. The quality factors of the fundamental in-plane mode were calculated from the frequency-response curves using Eq. 3.1 as 104.3 and 72.3 for the cavitary one-sided and double-sided sensors, respectively, and 91.4 and 77.7 for the solid one-sided and double-sided sensors, respectively.

The in-plane frequency-response curves of the sensors, Figure 3.5 , were also evaluated under harmonic excitation with V_{o} = 10 V while the signal frequency was swept from 210 kHz to 230 kHz for the solid sensors and from 230 kHz to 250 kHz for the cavitary sensors. The peak (resonance) velocities were 48.64 μm/s and 19.08 μm/s for the one-sided and double-sided solid sensors, respectively, and 61.41 μm/s and 43.06 μm/s for the one-sided and double-sided cavitary sensors, respectively.

23
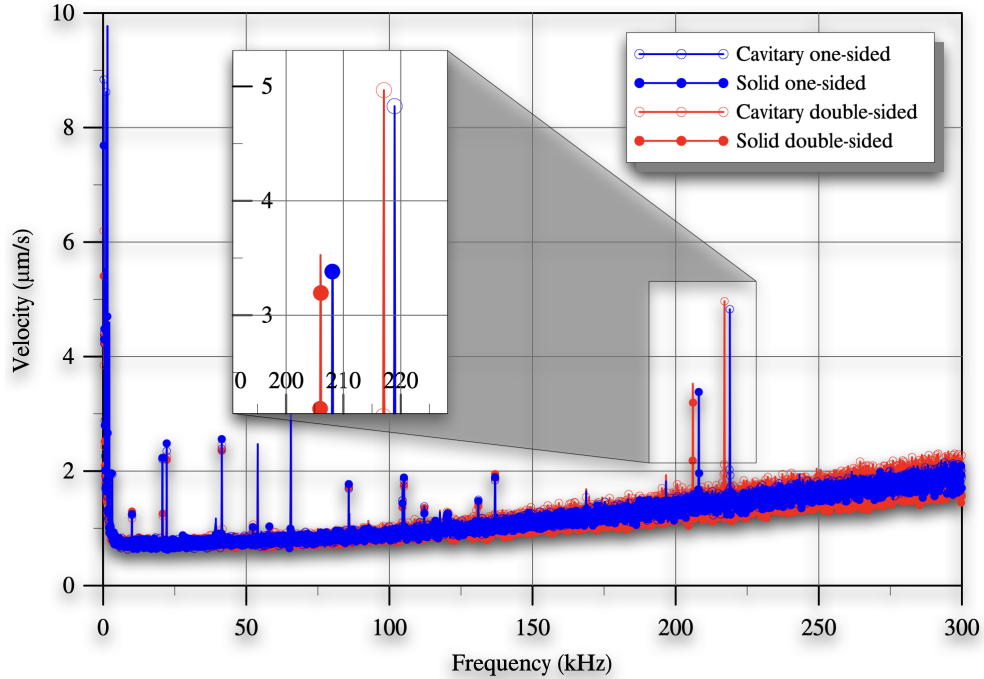
Figure 3.3: The out-of-plane modal response of the SOI sensors

The quality factors calculated from those frequency-response curves were 108.9 and 71.6 for the one-sided and double-sided solid sensors, respectively, and 105 and 79.9 for the one-sided and double-sided cavitary sensors, respectively. Those results show that in-plane sensors have higher quality factors than out-of-plane sensors, regardless of their configuration. For comparison, similar out-of-plane electrostatic MEMS gas sensors had a quality factor of 5.4 [17]. Further, we find that one-sided in-plane sensors have higher quality factors (lower damping) than double-sided sensors. Those results are in agreement with the findings of Alcheikh et al. [47]. The latter FEM found that double-sided MEMS resonators have lower quality factors than one-sided MEMS resonators.

Resonant inertial gas sensors typically measure the gas concentration as a shift in the resonant frequency due to added mass. The voltage required to operate those sensors should maintain a signal-to-noise ratio at the resonance of 3 or better to guarantee detectability. We measured the response of the four sensor variants to the harmonic waveform described in Eq. 2.6 in terms of the beam tip in-plane velocity as a function of the actuation voltage amplitude, Figure 3.6.
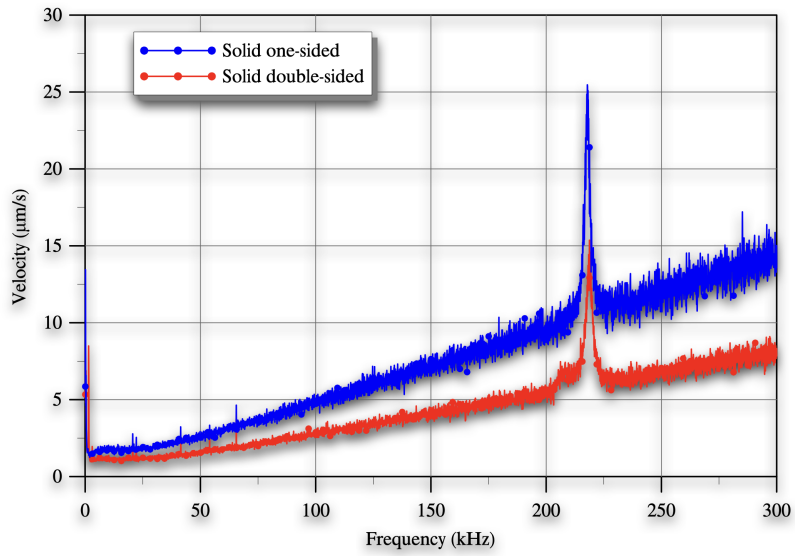
(a)   solid one-sided and double-sides sensors
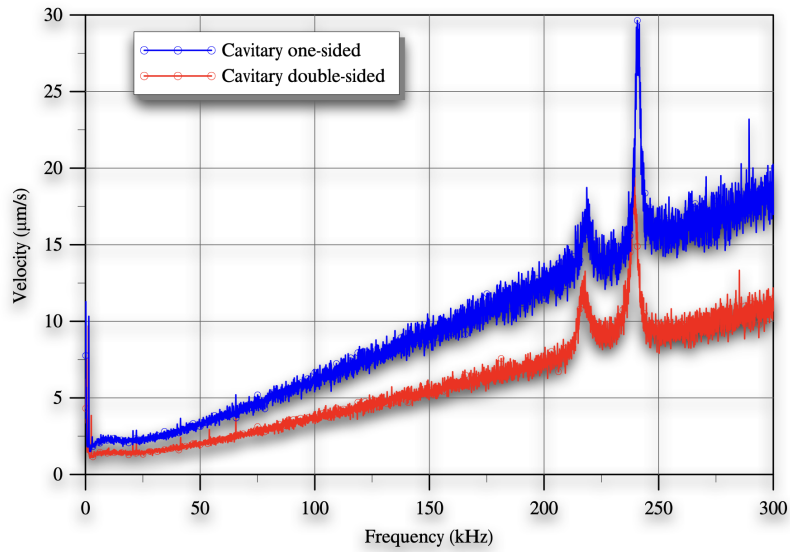
(b)   cavitary one-sided and double-sides sensors

Figure 3.4: The in-plane frequency-response curves of the sensors under white noise excitation
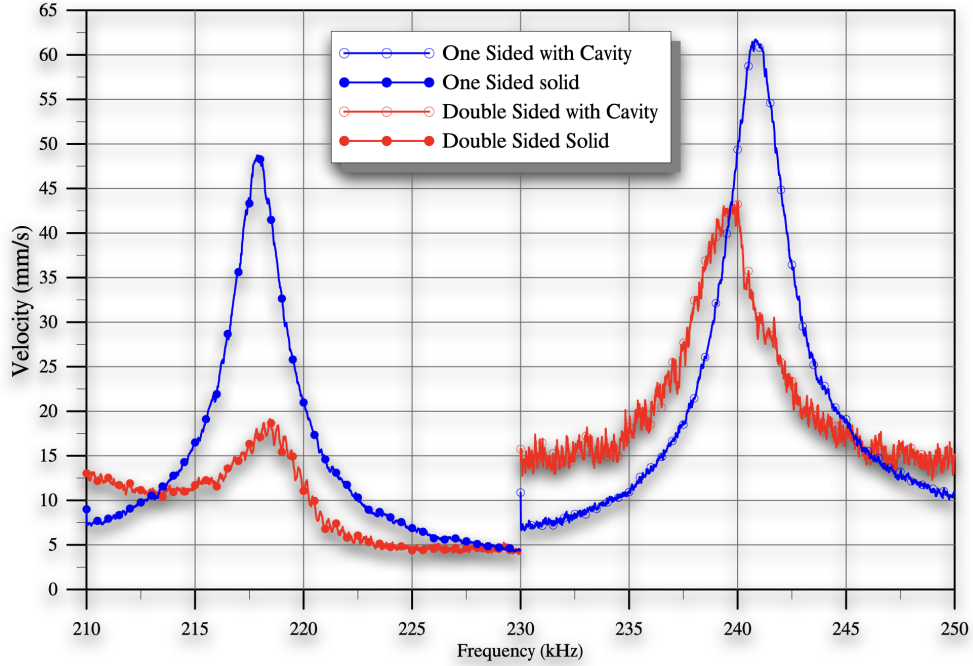
Figure 3.5: The in-plane frequency-response curves of the four sensor variants under harmonic excitation with $V_{\mathrm{o}} = 10\,\mathrm{V}$

Cavitary sensors significantly larger response under the same excitation waveform compared to solid sensors. The magnitude of in-plane velocity at $V_o = 10V$ was $77.64\,\mu\mathrm{m/s}$, $38.96\,\mu\mathrm{m/s}$ for the cavitary one-sided and double-sided sensors, respectively, compared to $3.33\,\mu\mathrm{m/s}$, $2.43\,\mu\mathrm{m/s}$ for the solid one-sided and double-sided sensors, respectively. The peak velocity of the cavitary one-sided sensor was 32 times larger than the velocity of the solid double-sided sensor.

Finally, we estimated each sensor's minimum detectable mass, assuming a minimum detectable frequency shift of $0.1\,\mathrm{Hz}$. The sensitivity of the sensors was also evaluated as the ratio that frequency shifts with respect to the underlying mass change. The results are listed in Table 2. The cavitary one-sided sensors had the smallest minimum detectable mass at 0.565 pg and the highest sensitivity at 177 Hz/ng.
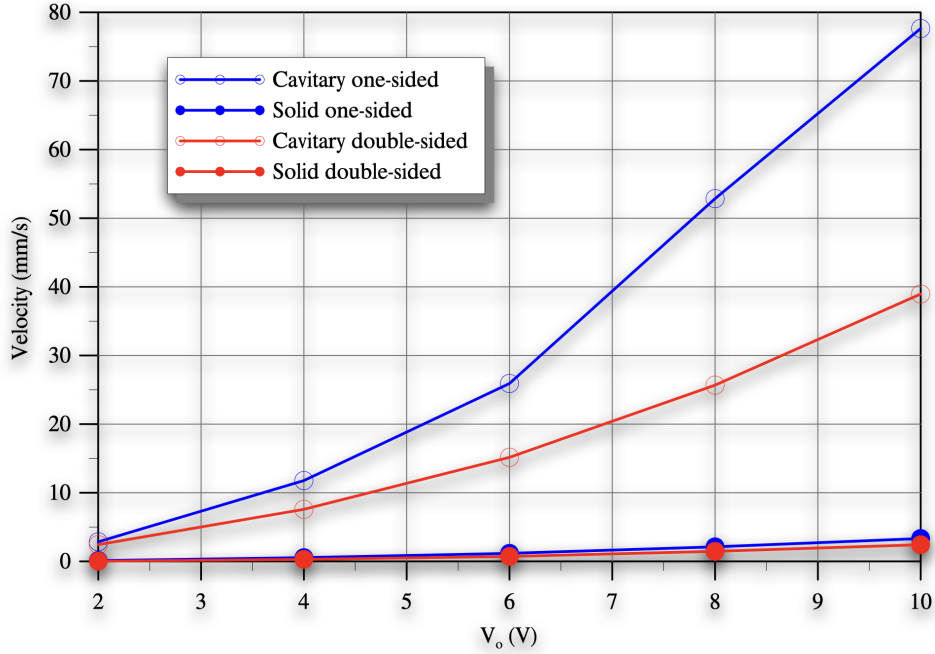
Figure 3.6: Peak velocity of the sensor variants exited by the harmonic waveform $V(t) = V_\circ + V_\circ \cos(\omega_{i,1} t)$ where $\omega_{i,1}$ is the fundamental natural frequency of each sensor

3.3 Conclusions

In-plane gas sensors were designed and fabricated using a custom SOI fabrication process to investigate the performance of four variant sensor designs. The sensors were successfully fabricated and coated with a metalization layer of gold to prevent dielectric charging. The performance of those sensors was evaluated and is summarized in Table 3.2. The results show that in-plane sensors have higher quality factors than comparable out-of-plane sensors. Further, one-side actuated sensors have higher quality factors than comparable double-side actuated sensors. In addition, cavitary sensors have lower voltage requirements, are more sensitive, and have smaller minimum measurable mass compared to solid sensors. We recommend that in-plane sensor designers forego any advantages that may arise from double-sided actuation in favor of the lower damping provided by one-sided actuation. Instead, they should secure lower actuation voltages by reducing the sensor mass and stiffness via cavitary sensor designs.

Table 3.2: Performance characteristics of the in-plane sensors

	Cavitary One-sided	Solid One-sided	Cavitary Double-sided	Solid Double-sided
Natural Freq (kHz)	240.84	217.85	239.70	218.44
Q White Noise	104	91	72	78
Q Freq. sweep	105	109	80	72
Velocity (mm/s)	77.64	3.33	38.96	2.43
Sensor Mass (ng)	681	839	681	839
Minimum Detectable mass (pg)	0.57	0.77	0.57	0.77
Sensitivity (Hz/ng)	177	129	176	130

Chapter 4

Electrostatic Bifurcation In-Plane Sensor Model

Creating a mathematical model for the MEMS sensors is very important to figure out possible linear and nonlinear behaviors. It also helps to predict how the sensor will work under different conditions and the accurate working range of the sensor. Electrostatic MEMS sensors are known for their nonlinear behavior and bifurcations, and those nonlinearities make the system more challenging to solve [48]. However, they can be used as a detection mechanism to achieve higher and more accurate sensitivity [17, 21, 48, 49, 50].

In the microscale range, pressure plays a non-negligible role in the performance of the system [51, 52, 53]. Actuation of the sensor impacts the fluid pressure in the gap between the beam and the fixed part and vice versa. This causes the major portion of the damping in the system damping, squeeze film damping [23, 24, 26]. Including this coupling between pressure and the beam in a mathematical model adds more complexities to the system.

The given rise to the squeeze-film damping force can be simulated using a two-dimensional compressible Reynolds equation that governs the pressure in the gap $\bar{P}$. This equation can be used easily in coupled to two-dimensional structural problems, such as that of a plate [53]. Since the beam equation is one dimension, the pressure equation should be reduced to one dimension. Hosseini et al. [54] eliminated Reynolds equation dependency on y by decomposing the total pressure into two functions of x and y, then integrating the pressure along the y direction to make the total pressure function of x only. A similar approach was taken by Nayfeh et al. [53] by assuming the pressure variation across the beam width to be small. Hasan et al. [48] integrated an approximate form of the pressure over the beam width to decouple the pressure and beam displacement. Alsaleem et al. [55] used

the Blech model to include the squeeze film effect in a lumped mass model they developed for an electrostatic resonator. They assumed a constant gap distance between two rigid plates.

Nayfeh et al. [53] used the perturbation method to solve the coupled system of a micro-plate and pressure equations. They used the finite element method to solve the perturbed system to get the mode shapes and natural frequencies. In previous work, [56], the coupled system of beam and pressure was discretized and solved using the Differential Quadrature Method (DQM) to get mode shapes, static and dynamic responses.

This chapter discusses the behavior of electrostatically actuated in-plane MEMS sensors under the effect of pressure. A coupled system of nonlinear Partial differential equations (PDEs) was solved to investigate the effect of squeeze film damping on the sensor's behavior. The Euler-Bernoulli beam equation coupled with a one-dimensional compressible Reynolds equation was used to represent the mechanical motion and pressure, and the system was solved using ROM.

4.1   Sensor Model

The electrostatically actuated in-plane sensor is a cantilever moving in a viscous medium (air or water) and actuated by a fixed side electrode, Figure 4.1. The dimensions of the cantilever are l length, b width, and h thickness. The sensor has a gap of d between the cantilever and the side electrode. The beam is actuated by a voltage difference V between it and a fixed electrode.

Following Euler-Bernoulli beam assumptions and accounting for linear viscous damping $\hat{c}\dot{w}$ and nonlinear damping of the fluid $\bar{P}(\hat{x}, \hat{t})h$, the equation of motion governing in-plane deflection $\hat{w}(\hat{x}, \hat{t})$ of the electrostatic sensor, is given by [57]

$$\rho b h \frac{\partial^2 \hat{w}(\hat{x}, \hat{t})}{\partial \hat{t}^2} + \hat{c}\frac{\partial \hat{w}(\hat{x}, \hat{t})}{\partial \hat{t}} + EI\frac{\partial^4 \hat{w}(\hat{x}, \hat{t})}{\partial \hat{x}^4} = F_e - \bar{P}(\hat{x}, \hat{t})h \tag{4.1}$$

subject to two boundary conditions at the fixed-end:

$$\hat{w}(0, \hat{t}) = 0 \qquad \text{and} \qquad \frac{\partial \hat{w}(0, \hat{t})}{\partial \hat{x}} = 0 \tag{4.2}$$

and two boundary conditions at the free-end:

$$\frac{\partial^2 \hat{w}(l, \hat{t})}{\partial \hat{x}^2} = 0 \qquad \text{and} \qquad \frac{\partial^3 \hat{w}(l, \hat{t})}{\partial \hat{x}^3} = 0 \tag{4.3}$$
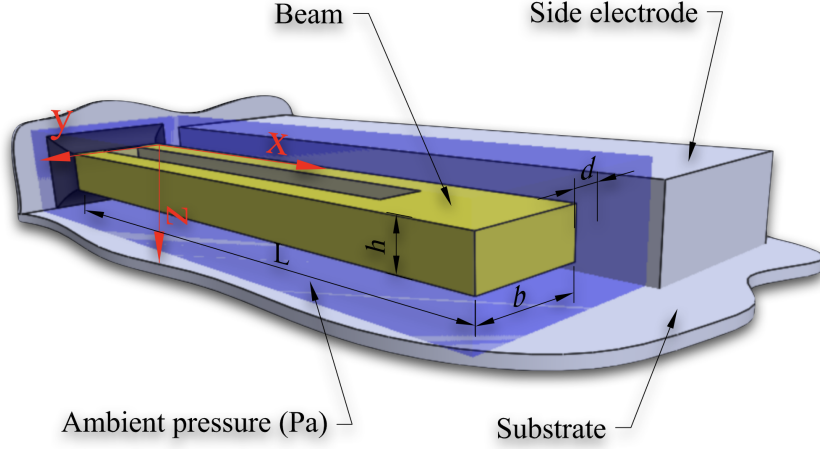
Figure 4.1: Schematic drawing of the in-plane sensor

where ρ is the microbeam density, E and I are Young's modulus and the second moment of area of the beam, and $\hat{c}$ is the linear viscous damping coefficient. The latter is used exclusively to account for energy losses due to non-fluidic sources, such as support losses and thermo-elastic damping. The electrostatic force term (F_e) in Eq. (4.1) can be calculated as:

$$F_e = \frac{\epsilon_r \epsilon_\circ h V^2}{2\big(d - \hat{w}(\hat{x}, \hat{t})\big)} \tag{4.4}$$

where $\epsilon_\circ$ and ϵ_r are the electrical permittivities of the vacuum and the viscous medium, respectively. V is the electrical potential difference between the beam and side electrode as defined in Eq. (2.6).

We assume that pressure variation across the beam width is negligible. This is reasonable considering the beam aspect ratio and the fact that deformations across the beam width are negligible. The two-dimensional Reynolds equation can be reduced to one-dimension as follows:

$$\frac{\partial}{\partial \hat{x}}\bigg(H^3(\hat{x}, \hat{t})\bar{P}(\hat{x}, \hat{t})\frac{\partial \bar{P}(\hat{x}, \hat{t})}{\partial \hat{x}}\bigg) = 12\,\eta_{eff}\bigg(H(\hat{x}, \hat{t})\frac{\partial \bar{P}(\hat{x}, \hat{t})}{\partial \hat{t}} + \bar{P}(\hat{x}, \hat{t})\frac{\partial H(\hat{x}, \hat{w})}{\partial \hat{t}}\bigg) \tag{4.5}$$

where $\bar{P}$ is the absolute pressure and H is the distance between the beam and the side electrode. η_{eff} is the effective viscosity of fluid. The pressure equation is subjected to zero flux at the fixed edge and trivial pressure boundary conditions at the free end:

$$\frac{\partial \bar{P}(0, \hat{t})}{\partial \hat{x}} = 0 \qquad \text{and} \qquad \bar{P}(l, \hat{t}) = P_a \tag{4.6}$$

31

where P_a is the ambient pressure. In the case of working in air, P_a is the atmospheric pressure. The gap distance and pressure H and $\bar{P}$ can be expressed as

$$H(\hat{x}, \hat{t}) = d - \hat{w}(\hat{x}, \hat{t})$$
$$\bar{P}(\hat{x}, \hat{t}) = P_a + \hat{P}(\hat{x}, \hat{w}) \tag{4.7}$$

Using equation (4.7) to substitute into Reynolds equation, Eqs. (4.5) and (4.6), we get

$$\frac{\partial}{\partial \hat{x}} \left(\left(d - \hat{w}(\hat{x}, \hat{t}) \right)^3 \left(P_a + \hat{P}(\hat{x}, \hat{t}) \right) \frac{\partial \hat{P}(\hat{x}, \hat{t})}{\partial \hat{x}} \right) =$$
$$12\, \eta_{eff} \left(\left(d - \hat{w}(\hat{x}, \hat{t}) \right) \frac{\partial \hat{P}(\hat{x}, \hat{t})}{\partial \hat{t}} + \left(P_a + \hat{P}(\hat{x}, \hat{t}) \right) \frac{\partial H(\hat{x}, \hat{w})}{\partial \hat{t}} \right) \tag{4.8}$$

$$\frac{\partial \hat{P}(0, \hat{t})}{\partial \hat{x}} = 0 \qquad \text{and} \qquad \hat{P}(l, \hat{t}) = 0 \tag{4.9}$$

The in-plane displacement of the sensor $\hat{w}(\hat{x}, \hat{t})$ can be decomposed into a static component $\hat{w}_s(\hat{x})$ and dynamic component $\hat{u}(\hat{x}, \hat{t})$, thus

$$\hat{w}(\hat{x}, \hat{t}) = \hat{w}_s(\hat{x}) + \hat{u}(\hat{x}, \hat{t}) \tag{4.10}$$

Reynolds equation can be linearized around the static equilibrium $\hat{w}_s(\hat{x})$ by substituting equation (4.10) into equation (4.8) and dropping the nonlinear terms. The linearized pressure equation can be written as

$$\frac{\partial}{\partial \hat{x}} \left(\left(d - \hat{w}_s(\hat{x}, \hat{t}) \right)^3 P_a \frac{\partial \hat{P}(\hat{x}, \hat{t})}{\partial \hat{x}} \right) = 12\, \eta_{eff} \left(\left(d - \hat{w}_s(\hat{x}, \hat{t}) \right) \frac{\partial \hat{P}(\hat{x}, \hat{t})}{\partial \hat{t}} + P_a \frac{\partial \left(d - \hat{w}_s(\hat{x}, \hat{t}) \right)}{\partial \hat{t}} \right) \tag{4.11}$$

We introduce the following parameters to nondimensionalize the governing equations.

$$x = \frac{\hat{x}}{l}, \qquad w = \frac{\hat{w}}{d}, \qquad t = \frac{\hat{t}}{\tau}, \qquad P = \frac{\hat{P}}{P_a}, \qquad \tau = \sqrt{\frac{\rho b h l^4}{EI}} \tag{4.12}$$

where τ is a characteristic time. The governing equations can be written in dimensionless form as:

$$\frac{\partial^2 w}{\partial t^2} + c \frac{\partial w}{\partial t} + \frac{\partial^4 w}{\partial x^4} = \alpha_1 V^2 \frac{1}{(1-w)^2} - \alpha_p P \tag{4.13}$$

$$\frac{\partial}{\partial x} \left((1 - w_s)^3 \frac{\partial P}{\partial x} \right) = \sigma \left((1 - w_s) \frac{\partial P}{\partial t} - \frac{\partial u}{\partial t} \right) \tag{4.14}$$

32

subject to the following boundary conditions:

$$w(0,t) = 0 \qquad , \qquad \frac{\partial w(0,t)}{\partial x} = 0$$

$$\frac{\partial^2 w(1,t)}{\partial x^2} = 0 \qquad , \qquad \frac{\partial^3 w(1,t)}{\partial x^3} = 0 \tag{4.15}$$

$$\frac{\partial P(0,t)}{\partial x} = 0 \qquad , \qquad P(1,t) = 0 \tag{4.16}$$

where:

$$c = \frac{\hat{c}l^4}{EI\tau}, \qquad \alpha_1 = \frac{6\epsilon_r\epsilon_\circ l^4}{Eb^3 d^3}, \qquad \alpha_p = \frac{P_a l^4 h}{EId}, \qquad \sigma = \frac{12\eta_{eff}l^2}{P_a\tau d^2} \tag{4.17}$$

4.2 Reduced Order Model (ROM)

This section develops reduced-order models to solve the static, forced eigenvalue, and nonlinear dynamic problems.

4.2.1 Static Problem

The static deflection of the microbeam was calculated by setting the time derivatives and the dynamic forcing terms in equation (4.13) equal to zero, to obtain:

$$\frac{d^4 w_s}{dx^4} = \alpha_1 V_{DC}^2 \frac{1}{(1 - w_s)^2} \tag{4.18}$$

subject to boundary conditions:

$$w_s(0) = 0 \qquad , \qquad \frac{dw_s(0)}{dx} = 0$$

$$\frac{d^2 w_s(1)}{dx^2} = 0 \qquad , \qquad \frac{d^3 w_s(1)}{dx^3} = 0 \tag{4.19}$$

4.2.2 Forced EVP

To derive the linear undamped EVP, we expand the electrostatic force term in a Taylor series around the static equilibrium w_s and drop damping, nonlinear, and forcing terms in

Eqs. (4.13) and obtain

$$\frac{\partial^4 u}{\partial x^4} - \frac{\partial^2 u}{\partial t^2} = \frac{\alpha_1 V^2}{(1 - w_s)^2} u \tag{4.20}$$

$$w_s(0) = 0 \quad , \quad \frac{dw_s(0)}{dx} = 0$$
$$\frac{d^2 w_s(1)}{dx^2} = 0 \quad , \quad \frac{d^3 w_s(1)}{dx^3} = 0 \tag{4.21}$$

The pressure equation and its corresponding boundary condition will not change. Assume the solution in the form:

$$w_s(x,t) = \phi(x)e^{i\omega_n t}$$
$$P(x,t) = \psi(x)e^{i\omega_n t} \tag{4.22}$$

where $\phi(x)$ and $\psi(x)$ are the nth mode shapes of the beam and the pressure, respectively, and ω_n is the corresponding non-dimensional natural frequency. Next, we substitute equations (4.22) into equations (4.14), (4.16), (4.20), and (4.21) to obtain

$$\phi_n^{(4)}(x) - \frac{\alpha_1 V_{DC}^2}{(1 - w_s)^2} = \omega_n^2 \phi_n(x) \tag{4.23}$$

$$\frac{d}{dx}\left((1 - w_s)^3 \psi_n'(x)\right) = i\omega_n \sigma\left((1 - w_s)\psi_n - \phi_n\right) \tag{4.24}$$

$$\phi_n(0) = 0 \quad , \quad \phi_n'(0) = 0$$
$$\phi_n''(1) = 0 \quad , \quad \phi_n^{(3)}(1) = 0 \tag{4.25}$$

$$\psi_n'(0) = 0 \quad , \quad \psi_n(1) = 0 \tag{4.26}$$

4.2.3 Dynamic Problem

To solve the dynamic problem we transform the PDEs (4.13) and (4.14) to a set of non-linear Ordinary differential equations (ODEs). We use a Galerkin expansion [58] within the framework of a weighted residual method to carry out the transformation. We use

34

the forced mode shapes of the cantilever beam and pressure as functions in the Galerkin expansion.

$$w(x,t) = \sum_{i=1}^{N} \phi_n(x)q_n(t)$$

$$P(x,t) = \sum_{i=1}^{N} \psi_n(x)r_n(t)$$

$$(4.27)$$

where N is the number of mode shapes used in the solution and $q_n(t)$ and $r_n(t)$ are the generalize coordinates of the displacement beam and gap pressure, respectively. Multiplying Eq. (4.13) by $(1-w)^2$ and substituting with Eq. (4.27) into Eqs. (4.13) and (4.14) yields:

$$(1 - \sum_{i=1}^{N} \phi_n q_n)^2 \frac{\partial^2 q_n}{\partial t^2} \phi_n =$$

$$-c(1 - \sum_{i=1}^{N} \phi_n q_n)^2 \frac{\partial q_n}{\partial t} \phi_n - (1 - \sum_{i=1}^{N} \phi_n q_n)^2 \frac{\partial^4 \phi_n}{\partial x^4} q_n \qquad (4.28)$$

$$+ \alpha_1 V(t)^2 - \alpha_p (1 - \sum_{i=1}^{N} \phi_n q_n)^2 \sum_{i=1}^{N} \psi_n r_n$$

$$\frac{\partial}{\partial x}\left((1-w_s)^3 \frac{\partial \psi_n}{\partial x} r_n\right) = \sigma\left((1-w_s)\frac{\partial r_n}{\partial t}\psi_n - \frac{\partial q_n}{\partial t}\phi_n\right) \qquad (4.29)$$

The orthogonality condition is be exploited by multiplying Eq. (4.28) by ϕ_n and Eq. (4.29) by ψ_n then integrating along the beam length from $x = 0$ to $x = 1$. The resulting ODEs are numerically integrated to find $q_n(t)$ and $r_n(t)$.

4.3   Results

4.3.1   Sensor Design

An in-plane sensor was used to validate the mathematical model. Figure 4.2 shows an SEM image of the sensor used for this purpose. The sensor was designed according to the conclusions of the chapter 3. It consists of a cantilever beam, side actuation, and landing

electrodes. The beam and landing electrode are electrically grounded while the electrical signal is connected to the side electrode. In order to decrease the beam mass, a through-hole was etched into it. A gold layer covers the whole sensor to eliminate dielectric charges. The sensor dimensions and material properties are listed in Table 4.1. All experiments were conducted in air under atmospheric pressure. The room pressure was measured as $P_a = 0.973\,\text{bar}$.
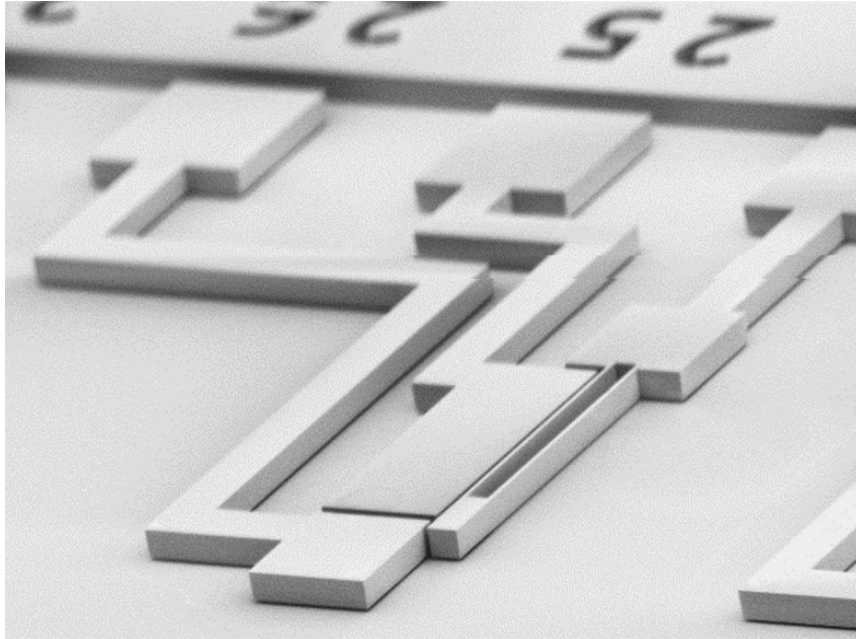
Figure 4.2: An SEM image of the electrostatic in-plane sensor

4.3.2 Static Response

The static displacement of the beam tip was obtained experimentally and predicted numerically from the model. The in-plane displacement of the sensor at the tip ($x = 450\,\mu\text{m}$) was measured experimentally under quasi-static excitation. A sawtooth voltage signal varying from $0\,\text{V}$ to $110\,\text{V}$ at a frequency of $3\,\text{Hz}$ was applied to the side electrode to obtain the displacement-voltage curve and pull-in voltage. It is shown as a line of red diamonds in Figure 4.3. The pull-in voltage was measured as $105.7\,\text{V}$ where a sudden jump in displacement is observed.

Wolfram Mathematica [59] "NDSolve" command was used to solve the static problem

36

Table 4.1: Dimensions and material properties of the in-plane sensor used to verify the mathematical model

Parameter	Value	Description
l	$450\,\mu$m	beam length
b	$40\,\mu$m	beam width
h	$30\,\mu$m	beam height
d	$3.5\,\mu$m	gap between beam and side electrode
l_e	$370\,\mu$m	length of beam cavity
b_e	$26\,\mu$m	width of beam cavity
ρ	$2330\,\text{N/m}^3$	density of beam
E	$160\,$GPa	Youngs modulus
ϵ	$8.854 \times 10^{-12}\,\text{F/m}$	permittivity of air
p_a	$0.973 \times 10^5\,Pa$	pressure of the ambient
ρ_g	$19300\,\text{N/m}^3$	density of gold
η	$1.81 \times 10^{-5}\,\text{kg/(m} \cdot s)$	viscosity of air
h_g	$0.2\,\mu$m	thickness of gold layer

Eq. (4.18) numerically for a given DC voltage via a shooting method. The predicted displacement was obtained at the tip ($x = 1$). The static displacement-voltage curve was obtained by increasing the DC voltage from $0\,\text{V}_{\text{DC}}$, with steps of $1\,\text{V}_{\text{DC}}$, until the residual error in the solver exceeds a predefined tolerance.

The static displacement curve is plotted in Figure 4.3 as a line of blue circles. Pull-in voltage was predicted at $106\,$V. The results show a good match between experimental measurements and model predictions. The static in-plane response is similar to that of traditional out-of-plane sensors.

The DUT was fabricated using the custom SOI microfabrication process mentioned in section 3.1.2. The beam support is held fixed employing a buried oxide layer. Releasing the MEMS structure includes etching away some oxide layer regions, which may weaken the support. To match the model to experimental measurements, the beam stiffness was reduced from an as-designed value to an as-fabricated value representing the non-ideal support.
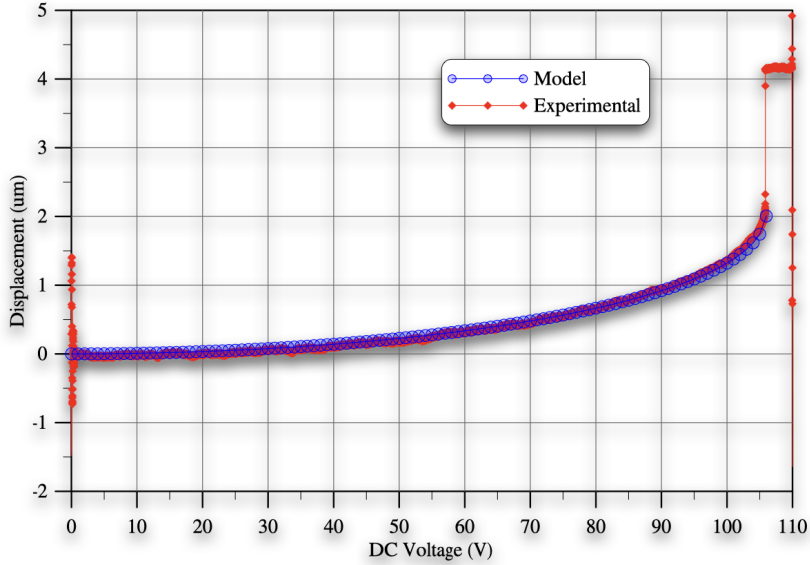
Figure 4.3: Comparison between the experimentally measured and calculated static in-plane displacement as a function of DC bias

4.3.3 Modal Response

The natural frequencies of the beam were calculated under three bias levels of 5V, 10V, and 15V. They were found to be 25.594 kHz, 25.571 kHz, and 25.531 kHz, respectively. The softening effect of bias voltage, which reduces the natural frequency as voltage increases, is a common characteristic of electrostatic MEMS.

The first three mode shapes of the beam are shown in Figure 4.4. The mode shapes were invariant for all three values of DC voltage 5V, 10V, and 15V. They were also incidental, to the well-known mode shapes of unloaded cantilever beams.

The first and second pressure mode shapes are shown in Figure 4.5. The pressure mode shapes were sensitive to variations in ambient pressure. Figure 4.5 shows the pressure mode shapes at three levels of ambient pressure, $P_a = 0.5$ bar, 1.0 bar, and 1.5 bar. They were most sensitive to variations in ambient pressure at the peak closest to beam tip. The squeeze number σ increases as the ambient pressure P_a drops, per Eq. (4.17), allowing the pressure under the beam to experience larger variations as it approaches ambient pressure at the beam tip. On the other hand, the interior peak of the second pressure mode was insensitive to variation in ambient pressure. This is expected since the no-penetration condition at the wall does not vary with ambient pressure.

38
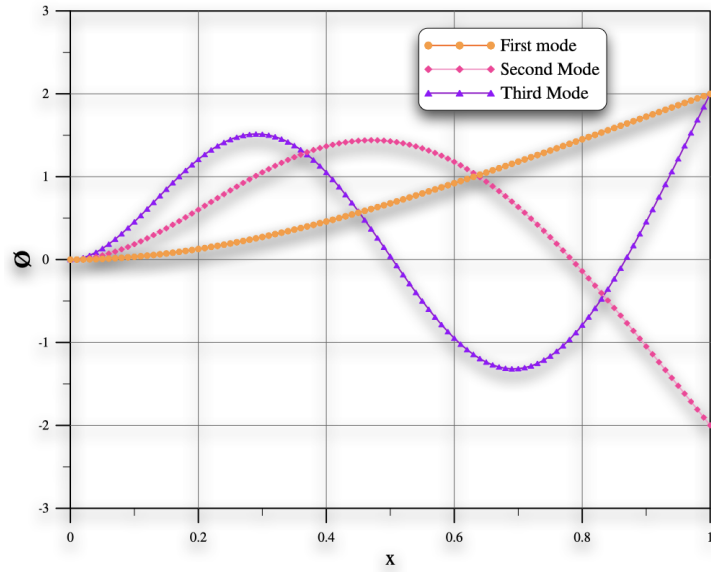
Figure 4.4: The first three mode shapes of the beam
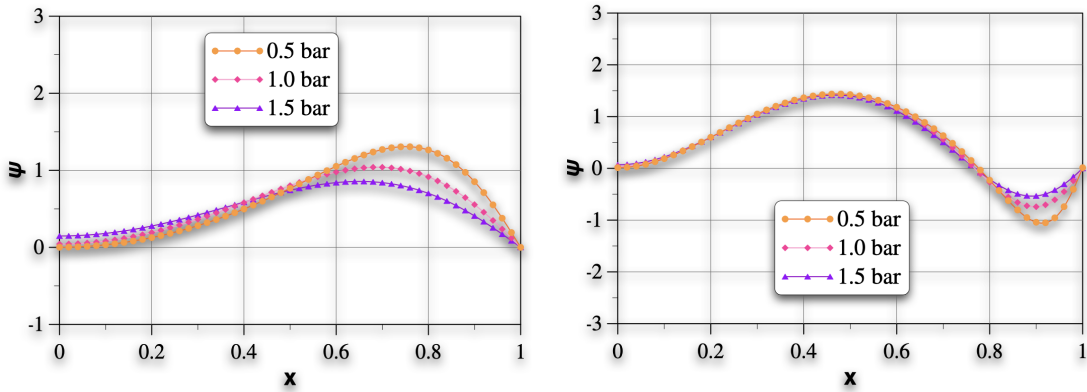
(a) First pressure mode shape

(b) Second pressure mode shape

Figure 4.5: The (a) first and (b) second mode shapes of pressure at three levels of ambient pressure

As ambient pressure P_a drops, a narrow region in the vicinity of the beam tip experience sharper change in pressure and result in a boundary layer where the standard solution techniques are not suitable. Perturbation analysis can be used to solve boundary layer

problems [52, 60]. In future work, we will follow this approach as outlined in Appendix A to solve the eigenvalue problem.

4.3.4 Dynamic Response

The coupled system of equations describing the interactions of the beam and medium was solved for the sensor motions and gap pressure. The initial-value problem of the ROM, Eqs. (4.28) and (4.29), was numerically integrated using Mathematica NDSolve command subject to the initial conditions $q_1 = 0,01$, $\dot{q}_1 = 0.01$, and $r_1 = 0.01$. The first beam and pressure mode shapes only were used in solving the system.

To estimate viscous damping due to non-fluidic sources, the sensor was placed in a vacuum chamber at a pressure of 5 μbar. A Lock-in Amplifier (Zurich Instruments HF2LI) was used to obtain the frequency-response curve of the sensor. The quality factor was measured as the slope of the phase-frequency curve at resonance:

$$Q = \frac{f_n}{2} \frac{d\theta}{df}\bigg|_{f_n} \tag{4.30}$$

It was found to be $Q = 214.6$.

The non-dimensional displacement and velocity of the beam tip were calculated under excitation by the voltage waveform of Eq. (2.6) for three excitation levels $V_\circ = 5$, 10, and 15 V. In all three cases; the excitation frequency was set equal to the unactuated natural frequency $\Omega = \omega_n$. The steady-state response was obtained by long-time integration for $100T$, where $T = 2\pi/\Omega$ is the excitation period.

The phase portraits of the beam tip in the vicinity of primary resonance ($\Omega = \omega$) and the superharmonic resonance of order-two ($\Omega = \omega/2$) are shown in Figure 4.6(a). The orbits were obtained as the response over the last excitation period $t = [99T, 100T]$. They were symmetric around the origin. The time-history of the excitation signal, displacement, and velocity are also shown in Figures 4.6(b) and (c) for primary and superharmonic resonances, respectively.

We also show in Figure 4.7(a) the phase portraits of the beam tip over the last excitation period $t = [99T, 100T]$ under excitation by waveforms with amplitudes of $V_\circ = 5$, 10, and 15 V and a frequency of $\Omega = 20$ kHz. This excitation frequency is between the primary and superharmonic resonances described above. The orbits grow nonlinearly with the increase in the excitation signal. Rather than being symmetric around the origin, they are shifted towards the electrode because of the bias introduced by electrostatic forcing. These are typical features of electrostatic MEMS.
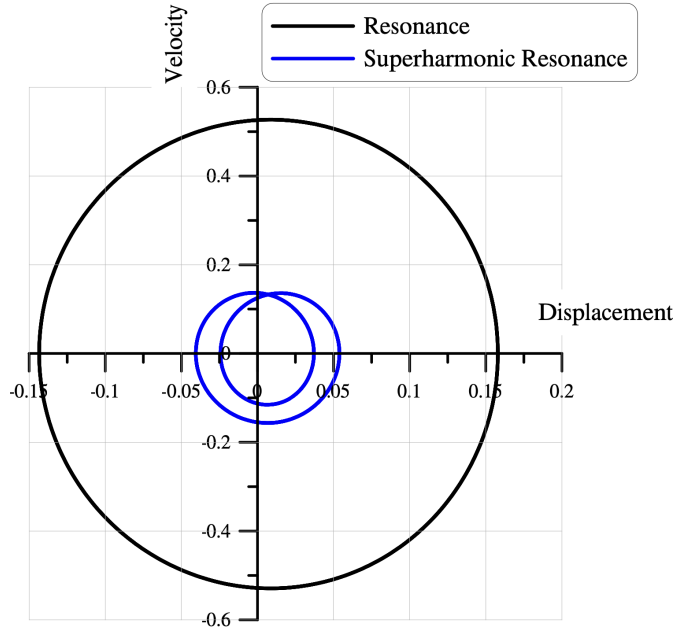
(a) Phase portraits of the beam tip
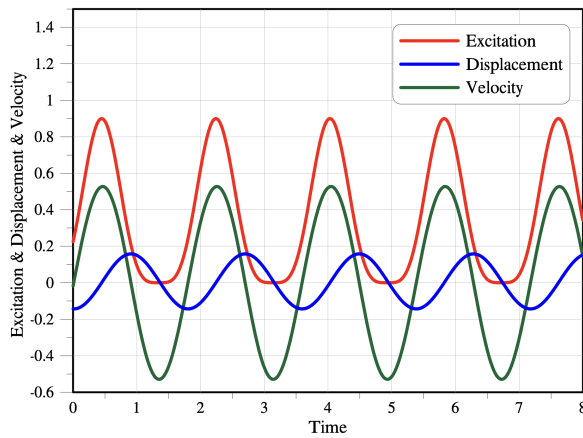
(b) Primary resonance
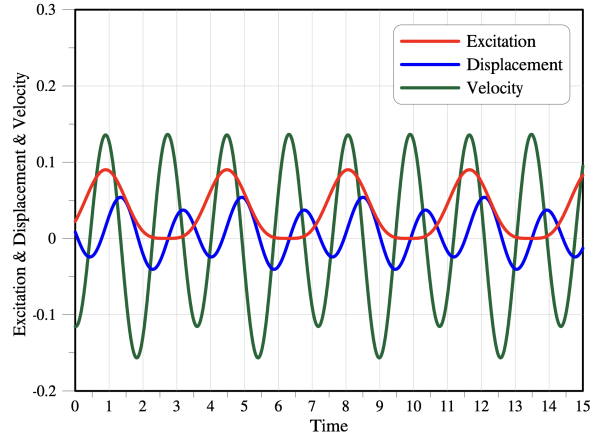
(c) Superharmonic resonance

Figure 4.6: The simulated (a) phase portraits and the nondimensional time-histories of the displacement and velocity of the beam tip in the vicinity of (b) primary and (c) super-harmonic resonances under excitation by a biased harmonic voltage with an amplitude of $V_\circ = 15$ V

41
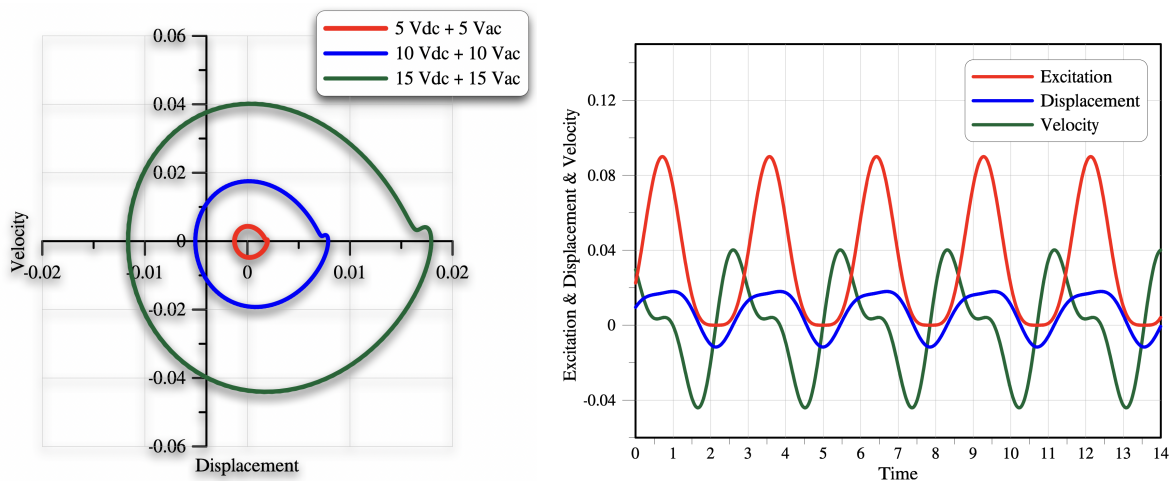
(a) Phase portraits under $V_\circ = 5$, 10, and 15 V   (b) Time data under $V_\circ = 15$ V

Figure 4.7: The simulated nondimensional time domain data of the beam tip at $20\,\text{kHz}$ harmonic excitation

The corresponding nondimensional time-histories of the excitation signal, displacement, and velocity are shown in Figure 4.7(b). They demonstrate a feature missing from the typical response of electrostatic MEMS in the literature. As the beam approaches maximum displacement (minimum gap), displacement and velocity stall before reversing direction and continuing to drop towards a zero-crossing, respectively. This is a result of the electrostatic force reaching a trough synchronously with squeeze-film damping force approaching its maximum value.

We compare in Figure 4.8 the measured frequency-response curve of the beam tip in-plane velocity (red diamond line) to that predicted by the ROM (blue line). The sensor was excited by a biased harmonic signal with $V_\circ = 15$ V. The signal frequency was swept from $\Omega = 10\,\text{kHz}$ to $55\,\text{kHz}$. The simulated frequency up-sweep was carried out at a step of $20\,\text{Hz}$. Long-time integration following the procedure described above was used to predict the steady-state response. The RMS of the beam velocity was evaluated over the last $4T$ of the time-history at each excitation frequency.

The experimental frequency up-sweep was carried out at a slew rate of $5\,\text{kHz/s}$. A specialized code was used to calculate the RMS of the velocity response over 10 periods centered around the excitation frequency of interest. A frequency step of $40\,\text{Hz}$ was used to construct the curve. To match and simulated frequency responses to its experimental

42

counterpart, parameter identification was performed. We matched the peaks at the primary resonance of the two curves by identifying the effective viscosity of air.
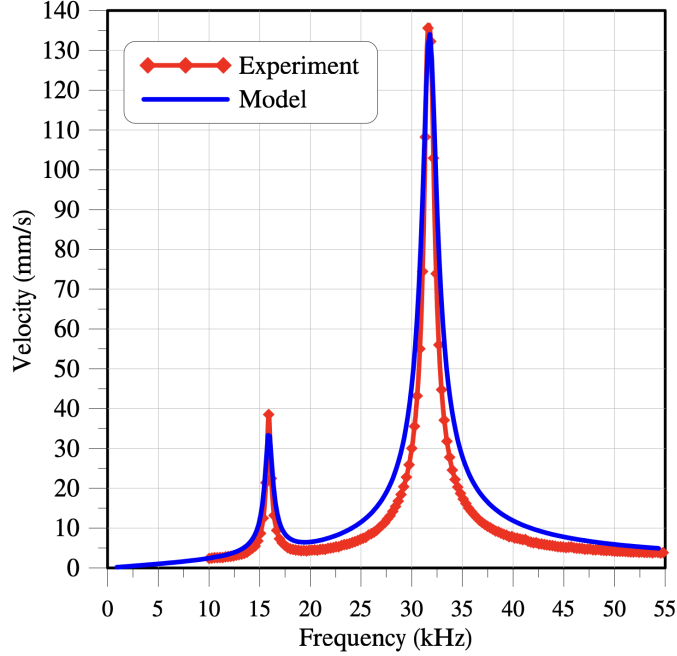
Figure 4.8: Comparison between the experimentally measured and simulate frequency-response curves of the sensor under the harmonic excitation $15\text{V}_{DC} + 15\text{V}_{AC}\sin(\Omega t)$

The results show good agreement between the model and experiment . Primary resonance frequency and amplitude were found to be $\Omega = 31.66\,\text{kHz}$ and $136.1\,\text{mm/s}$. The superharmonic resonance of order-two was also observed at $\Omega = 15.88\,\text{kHz}$ where the measured and predicted velocities were $38.57\,\text{mm/s}$ $34.6\,\text{mm/s}$, respectively.

Using the half-power bandwidth method, we found the quality factors at primary and superharmonic resonances from the experimental frequency-response as $Q = 33.9$ and 31.8. Similarly, the quality factors at primary and superharmonic resonances obtained from the simulated frequency-response were $Q = 25.6$ and 22.5. These results show that the fluidic forces contribute to linear energy loss mechanisms (viscous damping) in the sensor bringing down the quality factor at primary resonance from 214.6 to 33.9. On the other hand, the drop in the quality factor from primary to superharmonic resonance is incommensurate with the ratio between the two resonant frequencies (2:1) as would be predicted under

purely viscous damping conditions as per the relationship

$$Q = \frac{\omega_n m}{c}$$

This indicates the presence of nonlinear energy loss mechanisms that reduce the effective viscous damping coefficient c with the amplitude of oscillations resulting in a lower c value at superharmonic resonance. While the model underestimates the quality factor at primary and superharmonic resonances by 24% and 29%, respectively, it effectively captures the linear and nonlinear damping mechanisms described above. Further tuning of the model may ameliorate those numerical differences.

Changing ambient pressure from room pressure $P_a = 0.973$ bar to low pressure conditions ($P_a = 0.2$ bar) had a negligible impact on the frequency-response of the sensors. Figure 4.9 shows the simulated frequency-response curves of the sensor tip velocity for a voltage waveform with $V_\circ = 15$ V at those pressure levels. The two curves are almost on top of each other.
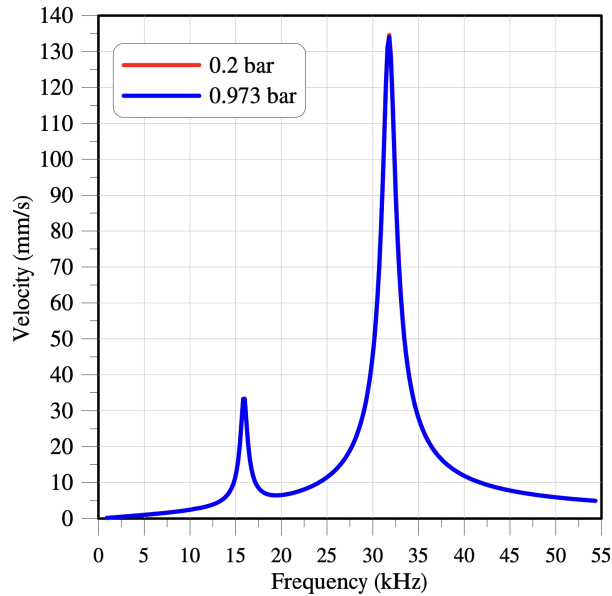
Figure 4.9: The simulated frequency-response curves of the sensor tip under room pressure $P_a = 0.973$ bar and low pressure $P_a = 0.2$ bar

The ROM was used to investigate the sensor response for higher excitation levels. Figure 4.10(a) shows the frequency-response curves of the sensor tip velocity under biased harmonic waveforms with amplitudes of $V_\circ = 20, 25, 30$, and 35 V. Similarly, Figure 4.10(b)

shows the frequency-response curves for voltage amplitudes of $V_\circ = 40, 45$, and $50\,\text{V}$. We found that the beam exhibits a softening effect common electrostatic MEMS due to the softening electrostatic nonlinearity. The frequency-response curves skew progressively to the left with as voltage amplitude, and the electrostatic force increase with the peaks moving from $\Omega = 31.62\,\text{kHz}$ to $31.34\,\text{kHz}$ as the amplitude increased from $V_o = 20$ to $25\,\text{V}$.

For voltage amplitudes of $V_o = 30\,\text{V}$ and higher, the frequency-response curves are composed of three branches: left, upper, and right. This is a result of a cyclic-fold bifurcation developing to the left of (a frequency below) the natural frequency ($\Omega < \omega_n$). At the bifurcation, the response jumps from a left branch of small stable orbits to an upper branch of large unrealizable orbits. Those orbits involve motions beyond the capacitor gap delineated by the dashed brown line in Figures 4.10. In practice, those orbits correspond to tapping mode oscillations. Since the model does not encompass contact with the substrate, it can not reproduce those motions.

For $V_\circ = 30\,\text{V}$, the cyclic-fold bifurcation point is located at a frequency of $\Omega = 29.98\,\text{kHz}$ where the velocity jumps from $527\,\text{mm/s}$ to $898.29\,\text{mm/s}$. Increasing the excitation amplitude to $V_o = 35$ and $40\,\text{V}$, shifts the cyclic-fold bifurcation progressively to the lift at $\Omega = 28.33\,\text{kHz}$ and $26.77\,\text{kHz}$, respectively. A second cyclic-fold bifurcation appears for voltage amplitudes of $40\,\text{V}$ and higher in the vicinity of the superharmonic resonance or order-tow at $\Omega = 13.44\,\text{kHz}$, in addition to the original cyclic-fold bifurcation at $\Omega = 25.542\,\text{kHz}$. The number of cyclic-fold bifurcations increased at an amplitude of $V_o = 50\,\text{V}$ as they appear in the vicinities of the superharmonic resonances of orders-two, -three, -four, and -five with the latter appearing at $\Omega = 6.532\,\text{kHz}$.

4.3.5   Underwater Sensor

We used the model to predict the sensor behavior underwater. The main differences between air and water as working media are their viscosities and relative permittivities. The relative permittivity was changed in the model from $\epsilon_r = 1$ for air to $\epsilon_r = 80$ for water properties. The effective viscosity was also increased from $\eta_{eff} = 0.35 \times 10^{-5}$ for air to $\eta_{eff} = 1.7 \times 10^{-4}$ for water.

Ghommem et al. [56] showed that the higher density and viscosity of water results in a drop in the in-plane natural frequency due to added mass and added damping. Have this drop is less severe than the case for out-of-plane motion. On the other hand, the elevated permittivity of water increases, the electrostatic force generated from the same input signal by a factor of eighty.
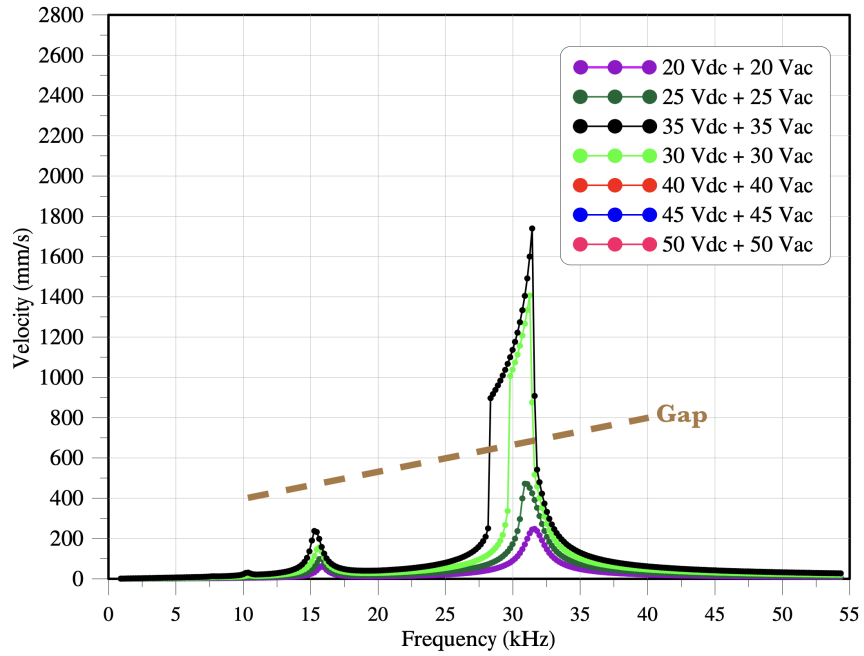
(a) Frequency-response curves for $V_o = 20, 25, 30,$ and $35\,\text{V}$
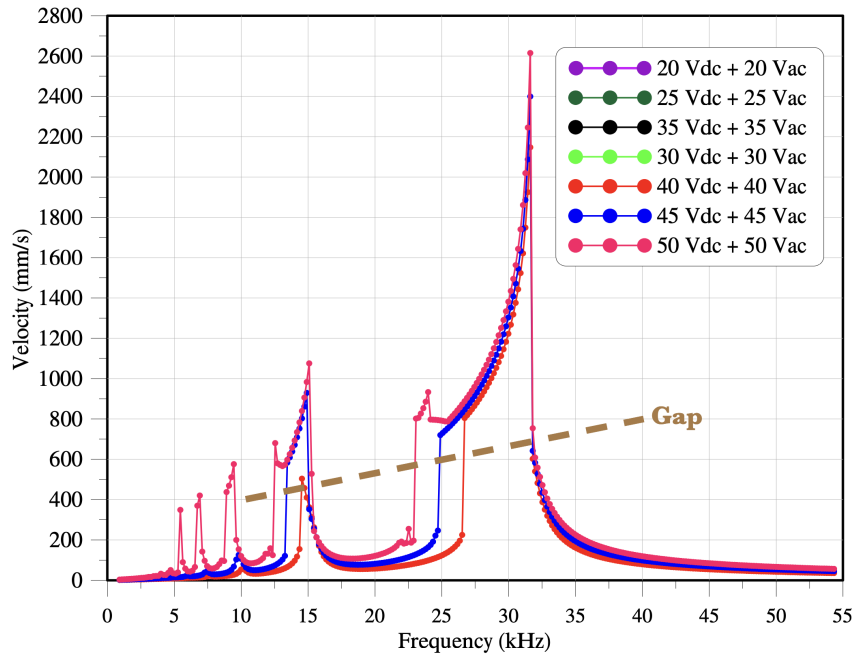
(b) Frequency-response curves for $V_o = 40, 45,$ and $50\,\text{V}$

Figure 4.10: The simulated frequency-response curves for the sensor tip velocity

The phase portraits of the sensor in water medium are shown in Figure 4.11 (a) for a biased harmonic excitation signal with a frequency of $\Omega = 31.6\,\text{kHz}$ and five amplitudes $V_o = 2, 4, 6, 8$, and $10\,\text{V}$. The long-time integration procedure described above was used to obtain the steady-state response. The simulated displacement and velocity increase with the signal amplitude. The orbits shift towards the side electrode as the static equilibrium position increases approaching static pull-in. The corresponding nondimensional time-histories of the signal, nondimensional displacement, and nondimensional velocity for $V_o = 10\,\text{V}$ are shown Figure 4.11 (b).
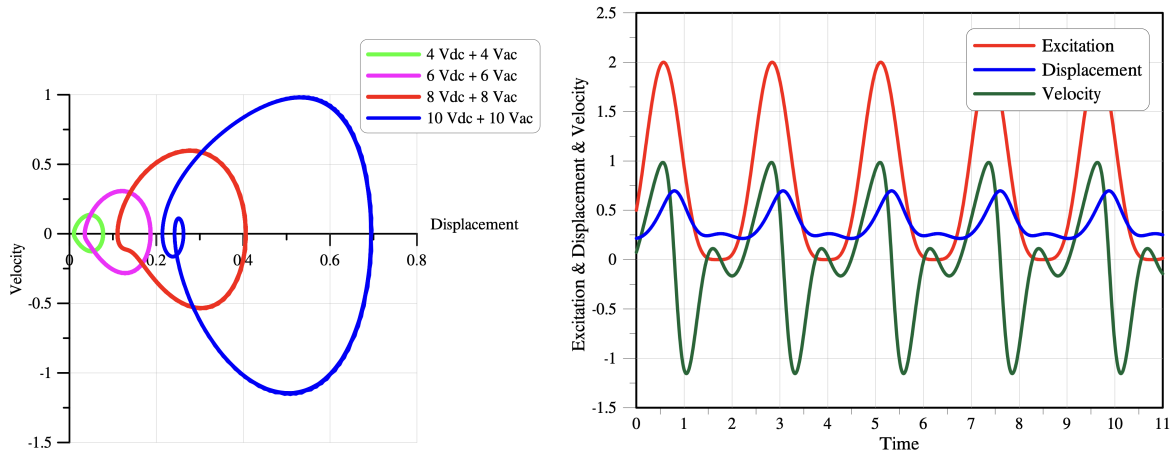
(a) The nondimensional phase portraits of the sensor under water

(b) The time-histories of the signal, displacement, and velocity

Figure 4.11: The simulated nondimensional (a) phase portraits of the sensor underwater for excitation signals with a frequency of $\Omega = 31.6\,\text{kHz}$ and amplitudes of $V_o = 2, 4, 6, 8$, and $10\,\text{V}$ and (b) the corresponding time-histories of the signal, displacement, and velocity for $V_o = 10\,\text{V}$

Using the procedure described above, the frequency-response curves of the sensor tip velocity were obtained for biased voltage waveforms with amplitudes of $V_o = 2, 4, 6, 8$, and $10\,\text{V}$ for a frequency up-sweep from 0 to $55\,\text{kHz}$, Figure 4.12. No sign of a resonant response can be detected over this frequency range, indicating that the first mode is overdamped. This is expected since the quality factor in air is $Q = 33.9$ will not survive a fifty-fold increase in effective viscosity.

We observe that the tip velocity increases linearly for an initial frequency range across all five excitation levels. This range increases with the excitation amplitude. Eventually,
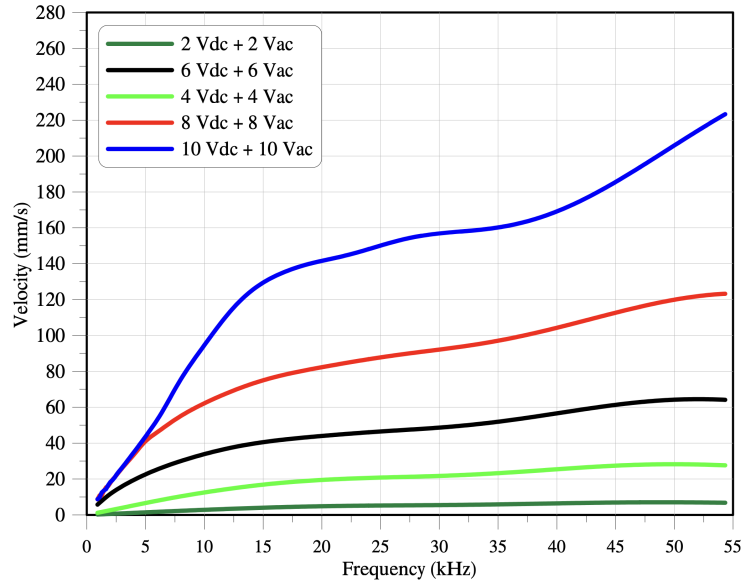
Figure 4.12: The simulated frequency-response curves for the sensor underwater for biased harmonic signals with amplitudes of $V_o = 2, 4, 6, 8,$ and $10\,\text{V}$

the rate of velocity increases with frequency undergoes a significant drop. This indicates that the damping mechanism has two ranges: a smaller linear level at low frequencies and a larger nonlinear level at higher frequencies.

It should be noted that the solver fails to converge for electrostatic forcing levels higher than an amplitude of $V_\circ = 10\,\text{V}$. It remains to be investigated whether that is due to numerical stiffness as the boundary layer close to the tip becomes narrower and pressure changes within it steeper or due to dynamic pull-in under complex damping mechanism.

4.4   Conclusions

A coupled system of nonlinear partial differential equations was solved to investigate the effect of squeeze film damping on the sensor's behavior. An experiment was conducted to check the validity of the mathematical model. Results of the model's static displacement show a good match with the experimental data. EVP was solved for the beam and the pressure. The natural frequencies drop as the electrostatic force increases. The softening behavior was noticed with increasing the bias voltage.

48

At pressure levels closer to the ambient pressure, the pressure mode shapes show a smooth change in the pressure. At lower pressure, the pressure tends to change quickly, creating a boundary layer at the tip. In this case, a different solution method may be considered. The dynamic response of the beam is similar to the response of the traditional electrostatic MEMS. We noticed a cyclic-fold bifurcation around the primary resonance when the $V_o = 30\,\text{V}$. Another cyclic-fold bifurcation was noticed around the superharmonic resonance when V_o was increased to $40\,\text{V}$. The number of the cyclic-fold bifurcation points was increased further when the harmonic excitation increased. The calculated frequency-response curves of the underwater sensor show almost flat responses because of the very high damping.

Chapter 5

Electrostatic Bifurcation Pressure Sensor

Most MEMS pressure sensors use at least two elements to achieve the pressure measurement process. First, the sensing element, which deforms when the pressure is applied to it. This sensing element should be as significant and thin as possible to achieve noticeable deformation when pressure is applied. The sensing element can be in the shape of a membrane, diaphragm, or plate. The second element is the transducer responsible for transforming the deformation (strain) of the sensing element into a readable output signal. The most popular transduction mechanisms in MEMS pressure sensors are piezoresistive, capacitive, optical, or resonance transduction [61, 62, 63, 64, 65].

In 1962, the first MEMS device ever was introduced as a piezoresistive pressure sensor [4, 5, 30]. Piezoresistive pressure sensors have high gauge factors; however, the operating range of the sensors is limited because of the high-temperature coefficient of the piezoresistive material used [62]. All the diaphragm-based pressure sensors have a limited operating range of temperature since the diaphragm can be permanently plastically deformed with the increase of pressure and temperature [62, 63].

Traditional MEMS capacitive sensors use a diaphragm to seal a chamber. This chamber may be vacuumed to measure the absolute pressure or filled with atmospheric pressure air to measure the differential pressure[61]. The absolute pressure sensor is considered more sensitive than the differential one; however, it is less robust. The most common fabrication processes of MEMS pressure sensors include wafer bonding processes to fabricate the required chamber[61, 66]. Capacitive pressure sensors were first introduced by Sander et al. of the Stanford Integrated Circuits Lab to improve the sensitivity and stability that is

possible with piezoresistive pressure sensors [5, 31]. The high output impedance and the nonlinear characteristics of the sensor response are disadvantages [66].

Nonlinear characteristics of the electrostatically actuated MEMS sensors could be advantageous if they are used as a detection mechanism [48, 67]. The nonlinear behavior of the electrostatic MEMS sensors includes static and dynamic pull-in [67, 68, 69]. Sub-harmonic or super-harmonic secondary resonance is also expected where a new resonance takes place at twice the natural frequency or half the natural frequency, respectively[70]. Electrostatic loading can lead to softening or hardening behaviors where the resonance frequency decreases or increases [69]. Cyclic fold bifurcation [33], Hopf bifurcation[71], and chaos [17] are also expected.

Hasan et al. [48] used the bifurcation as a detection mechanism for a binary capacitive pressure sensor. They used two designs of the sensors, First a large cantilever with proof mass. The sensor's natural frequency was $192.5\,\mathrm{kHz}$. The sensor's quality factor and bandwidth were small because of the small natural frequency. The sensor should be working at low pressures since working at pressure levels closer to the ambient temperatures may kill most of the bifurcations required for sensing. They also solved one degree of freedom lumped mass model for simulating the sensor's response.

Yu and et al. [64] fabricated A MEMS capacitive pressure sensor as an array of 16 membrane-based vacuumed sensors. The sensors were fabricated using a custom fabrication process. They investigated the effect of the membrane's size on the sensitivity of the sensor. It was noticed that the membrane pull-in into the substate at pressure levels lower than the atmospheric pressure.

karpati et al. [66] designed a capacitive pressure sensor to work in a range of $0-1000$ mbar. They found that their captive sensor's structure is unreliable at pressures higher than 800 mbar.

In this chapter, we try to overcome some limitations of the MEMS pressure sensors by introducing a new novel electrostatic bifurcation pressure sensor. The electrostatic bifurcation pressure sensor presented in this chapter uses an analog sensing mechanism to detect the change in the ambient pressure changes. The electrostatic bifurcation pressure sensor is a simple microstructure that can easily be fabricated using a standard multiuser or a custom fabrication process. It doesn't need wafer bonding, sealing, or any complex microfabrication process. It overcomes the limitations of temperature in the other pressure sensors. Unlike the other MEMS pressure sensors, the electrostatic bifurcation pressure sensor doesn't need a large area or vacuum cavity to operate. The functional parameters of the bifurcation pressure sensor are independent of the design dimensions of the sensor. It also collects the advantages of low power cost, a wide range of operations.

5.1 Methods

5.1.1 Sensor Design

An electrostatic bifurcation pressure sensor was designed based on the main conclusions of the chapter 3 and fabricated using custom SOI fabrication process. An SEM image of the sensor is shown in 4.2. The dimensions and characteristics of the sensor are described in Table 4.1.

Modal analysis of the in-plane pressure sensor was carried out using FEM to ensure the mode shapes and natural frequencies match the required design. COMSOL software was used for this purpose. The results of the modal analysis are shown in Figure 5.1. The first

(a) 1st in-plane bending

(c) 1st out-of-plane bending

(d) Beams 1st in-plane bending

(e) 2nd out-of-plane bending
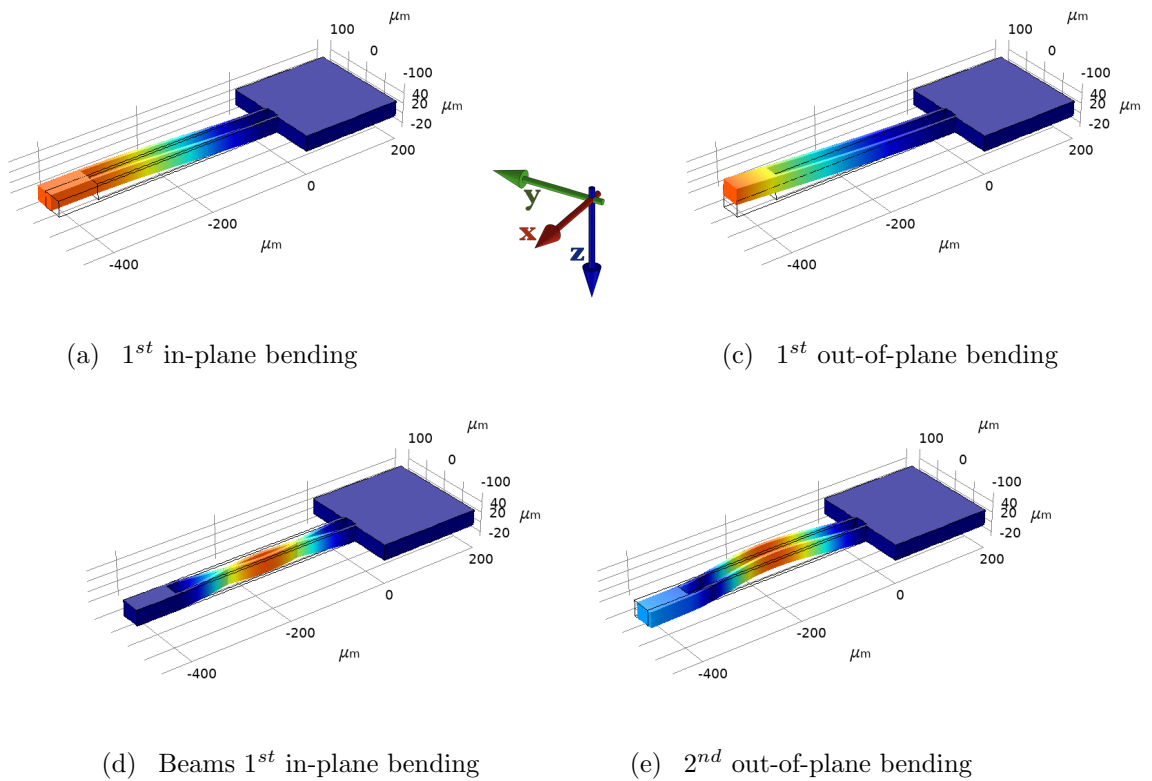
Figure 5.1: The first four mode shapes of the electrostatic bifurcation in-plane pressure sensor

mode shape was the first in-plane bending mode shape where the sensor moves along the y−axis. The calculated natural frequency of the sensor was 54.1 kHz. The second mode shape was found at 125 kHz where the beam moves out-of-plane along the z−axis. The third mode was the first in-plane bending mode of the beams. At this mode, the beams act like fixed-fixed beams supported by two fixed supports, the anchor from one end and the proof mass from the other end. This mode took place at 366 kHz. The fourth mode shape was the second in-plane mode shape. It was found at 384 kHz. The sensor's model analysis shows that the sensor's primary resonance was in-plane, which was one of the design requirements. The four modes are neither closer from each other nor closer to the harmonics of the first mode. This substantial property of the design ensures eliminating the chances of modal interactions.

5.1.2 Experimental Setup

Figure 5.2 shows the experimental setup of pressure testing. The sensor (DUT) die was wire bonded to the chip carrier and placed inside the pressure test chamber. The device is placed horizontal or tilted with an angle to measure out-of-plane or in-plane responses, respectively. The pressure test chamber was made of aluminum and equipped with a transparent acrylic cover to provide optical access of the LDV to the DUT. The chamber has a gas inlet and a gas outlet.

Controlling the pressure level inside the chamber includes two directions controlling, above and below the atmospheric pressure. Above the atmospheric pressure, the gas inlet is connected to a nitrogen gas tank via a stainless-steel piping system. The pressure inside the test chamber was measured using a pressure gauge that sends feedback of pressure measurements to the mass flow controller to control the amount of nitrogen entering the pressure chamber. For pressures below the atmospheric pressure, the gas outlet was connected to a vacuum pump. The mass flow controller balances the vacuuming rate with the gas flow rate at the required pressure.

The characterization of the sensor mainly includes generating frequency-response curves under different excitation conditions. The frequency-response curves were obtained in two ways. First, a harmonic voltage signal (Eq. 2.6) is held constant at $V_\circ$ while the excitation frequency Ω is swept with a slew rate of 20 kHz/s. The signal was applied to the sidewall electrode only. Then, the velocity response of the sensor was measured using MSV-400, and UHF-120 LDVs from Polytec [45] and collected using a real-time oscilloscope. RMS was calculated from the collected data using a dedicated mathematical code designed for this purpose. The frequency-response curves were generated at a resolution of 10 Hz.
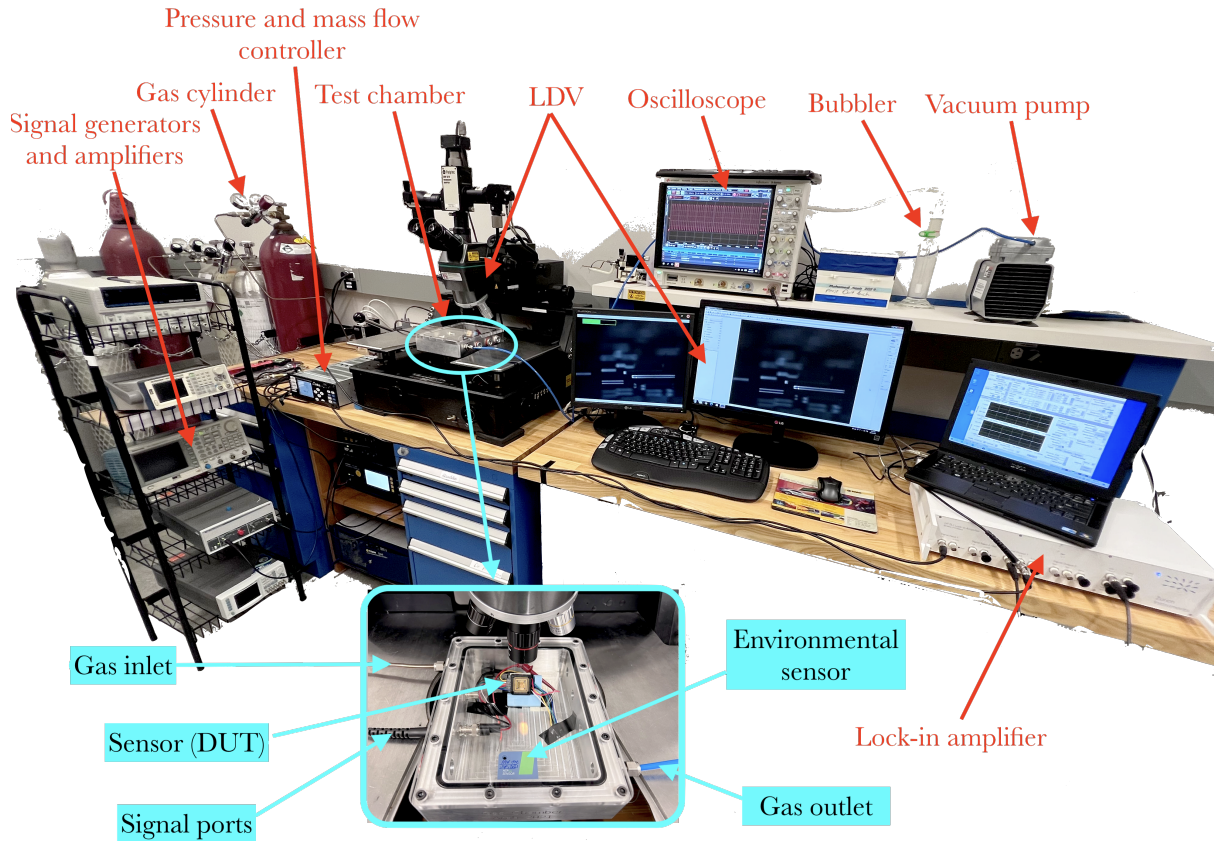
Figure 5.2: Experimental setup of pressure testing

Second, An HF2LI 50 MHz Lock-in Amplifier from Zurich Instruments has been used to obtain frequency-response curves. The lock-in amplifier applies the signal at a specific frequency and measures the response at this frequency or its harmonics. The maximum output signal of the lock-in amplifier is $10\,\text{V}$. Therefore we used a high voltage amplifier to amplify the lock-in's signal. The signal was supplied to the electrostatic bifurcation pressure sensor through co-axial electric ports built in the pressure test chamber.

As explained in Chapter 2, the sensor was tilted by $\phi = 60°$ to allow measuring in-plane motions. The apparent velocity response of the electrostatic pressure sensor was measured optically using the LDV. The lock-in amplifier collected the measured velocity response at the excitation frequency only or its harmonic. The amplitude of the apparent

measured velocity response is then calculated. The velocity amplitude at this frequency can be calculated from Eq 2.5. The response shift can be plotted by comparing the input velocity response with the output excitation signal.

5.2   Results and discussion

5.2.1   Basic Characterization

The initial characterization of the fabricated sensor starts with selecting a healthy sensor. For this purpose, an electrical connectivity test was conducted on different sensors on the die. The different parts of the sensor were electrically probed to make sure that the gold was covering this part, not touching any other part of the structure, and close the electrical circuit. The natural undamped unforced response of the sensor was examined by actuating the sensor using white thermal noise. The sensor was placed inside a vacuum chamber, and the pressure inside the chamber was reduced to 4 mbar. The in-plane and out-of-plane frequency-response curves over a wide bandwidth were obtained, and the frequencies of the noticeable response were recorded. A higher resolution in-plane and out-of-plane frequency-response curves were measured around the recorded frequencies from the white thermal noise experiment for both in-plane and out-of-plane responses.

In-plane and out-of-plane frequency-response curves of the electrostatic bifurcation pressure sensor were obtained by actuating the sensor by $15V_{dc} + 15V_{ac}\sin(\Omega t)$. Where Ω was swept from 10 kHz to 90 kHz. The results are plotted in Figure 5.3. The forced natural frequency was observed at 31.66 kHz where the sensor moves in-plane. The measured natural frequency was lower than the calculated natural frequency from the FEM. This difference can be explained as the effect of defects in the SOI fabrication process, as well as the sacrificial layer is not as rigid as the silicon anchor. A super-harmonic resonance of the sensor was noticed at 15.88 kHz. The out-of-plane response curves show that the first out-of-plane took place at 82.226 kHz.

The quality factors were calculated using the half-power bandwidth method, Eq. 3.1. It was found that the quality factor at the first in-plane and out-of-plane mode shapes, $Q_{i,1} = 148$ and $Q_{o,1} = 122$, respectively.

To investigate the nonlinearities and bifurcations of the electrostatic pressure sensor, frequency-response curves were obtained by applying harmonic signals with different amplitudes. We used 15 V excitation signal V_o then increased it in steps of 0.5 V until we hit the cyclic-fold bifurcation. The frequency Ω was swept in the two directions upward
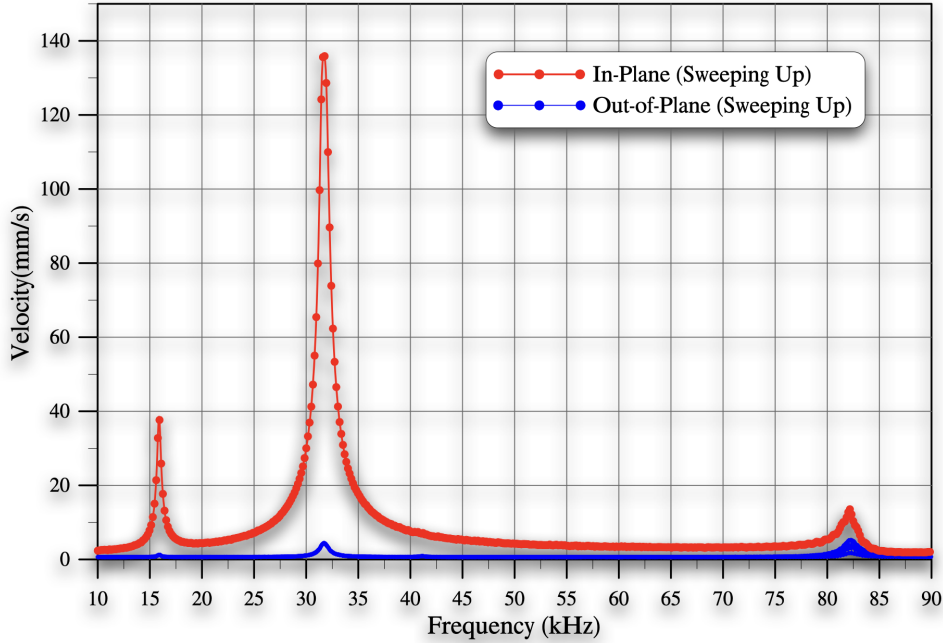
Figure 5.3: In-plane and out-of-plane Frequency response curve for the sensor in air

and downward around the primary resonance of the sensor. Figure 5.4 shows the up and down-sweep frequency-response curves of the sensor. The figure shows softening behavior of the sensor in both the up and down-sweep curves. As example, at $V_o = 15$ V the primary resonance was observed at 31.66 kHz while it was 31.59 kHz and 31.387 kHz for $V_o = 16.5$ V and $V_o = 18$ V, respectively.

At $V_o = 19.5$ V, the pressure sensor exhibits a cyclic-fold bifurcation in the velocity response. The velocity jumps suddenly at 30.967 kHz from 180.5 mm/s to 250 mm/s. Because the pressure sensor design includes a limit stopper (the landing electrode), the tip of the beam can't exceed this displacement and velocity limit. The sensor starts to tap in the landing electrode. This tapping mode starts at 30.913 kHz and ends at 31.566 kHz for $V_o = 20$ V excitation.

The electrostatic pressure sensor's down-sweep frequency-response curves 5.4 show almost the same behaviors as the up-sweep curves before entering the tapping mode oscillation.

There were two jumps in the up-sweep frequency-response curves from the lower stable branch to the tapping mode oscillation (jump-up) and another at the tapping mode's end to
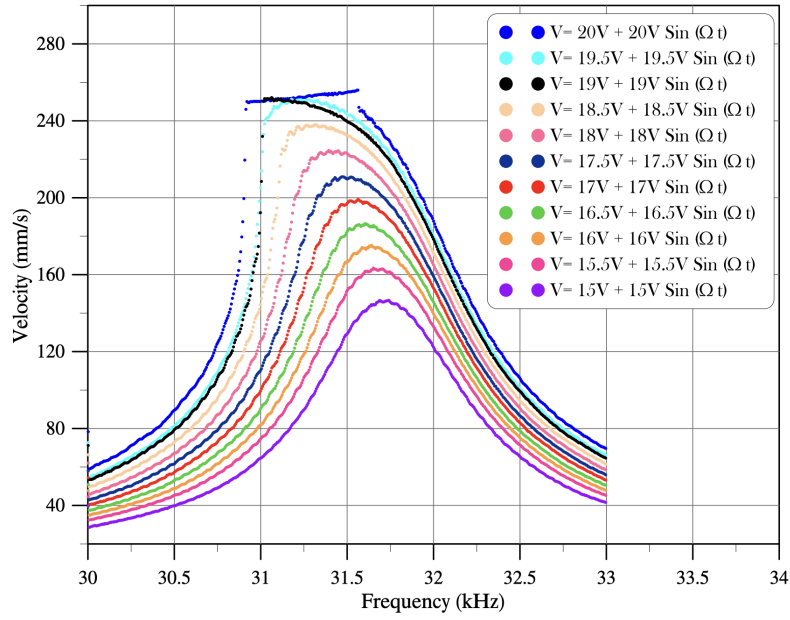
(a)   up-sweep
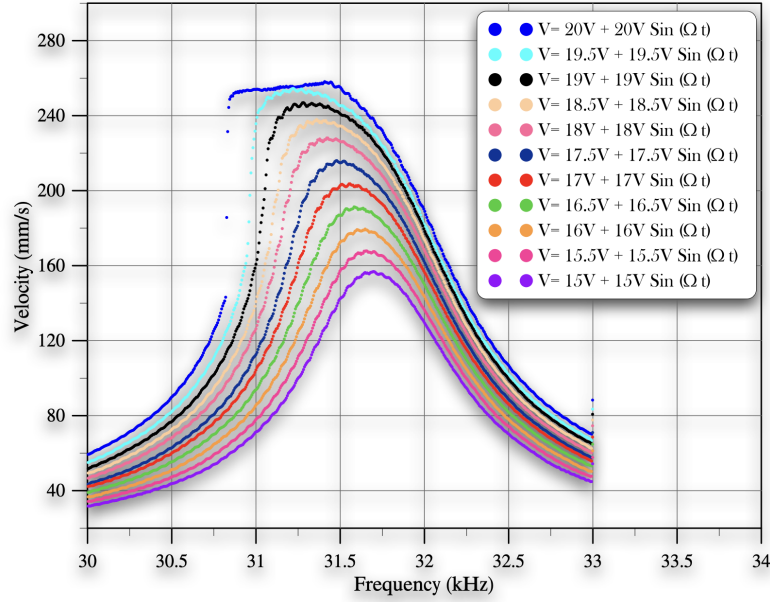
(b)   down-sweep

Figure 5.4: Up and down-sweep frequency-response curves show the softening behavior of the electrostatic pressure sensor and the start of the tapping mode

57

return to the lower stable branch (jump-back). The down-sweep frequency-response curves show that the sensor enters the tapping mode oscillation smoothly without a noticeable significant jump. However, when the sensor tries to exit the tapping mode, its response jumps from the tapping mode to the lower stable branch (jump down). The difference between the frequency of the jump-up and down is called hysteresis region[17]. Figure 5.5 shows the jump down at 30.837 kHz therefore the hysteresis region of the sensor under $V_o = 20\,V$ excitation is 76 Hz. The curve also shows a perfect match between the up and down-sweep frequency-response curves.
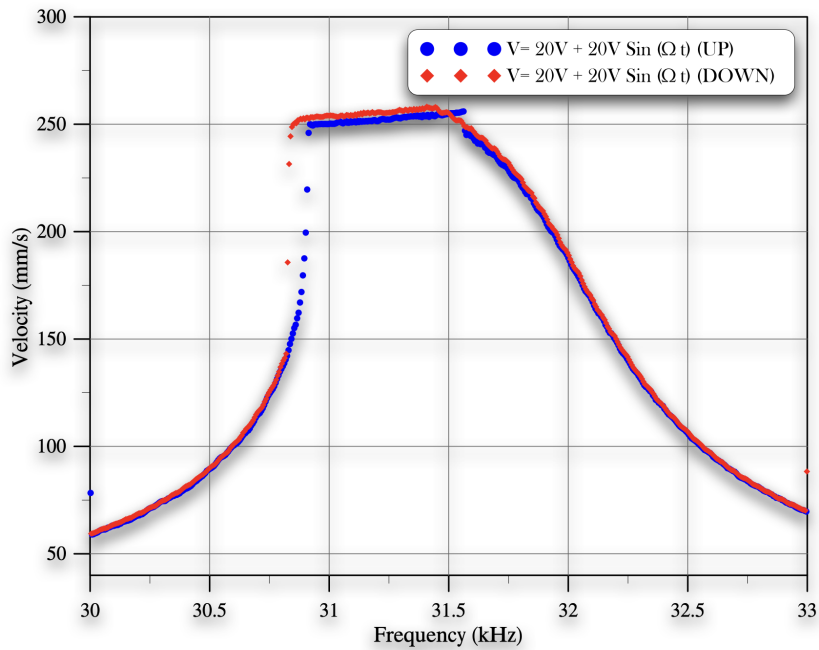
Figure 5.5: Frequency-response curves of the electrostatic pressure sensor show hysteric region between the jumps in the up and down-sweep

The characteristics of the electrostatic bifurcation pressure sensor were investigated at the tapping mode oscillation by increasing the harmonic excitation signal V_o. Figure 5.6 shows the tapping mode oscillation of the pressure sensor under $V_o = 20, 22.5$, and 25 V. The results show that tapping mode oscillation is still obtained until 25 V. As the excitation signal increases, the bandwidth of the tapping mode increases. For example, at $V_o = 20\,V$, the bandwidth of the tapping mode was 769 Hz while it was 2.016 kHz and 2.702 kHz under $V_o = 22.5\,V$ and $V_o = 25\,V$, respectively. The hysteresis region was 76 Hz for the sensor

under $V_o = 20$ V. This region was increased to 400 kHz and 682 kHz when excitation signal was increased to $V_o = 22.5$ V and $V_o = 25$ V, respectively.
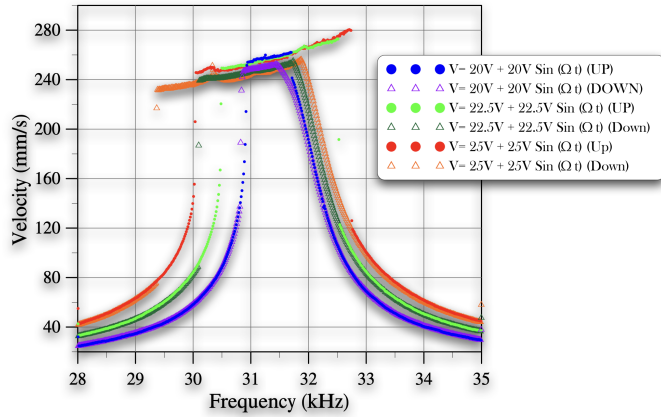
(a) $V_o = 20, 22.5,$ and 25 V
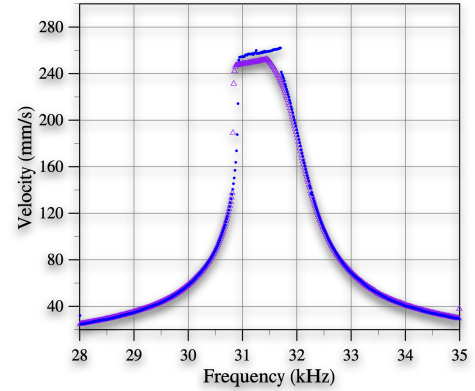
(b) $V_o = 20$ V
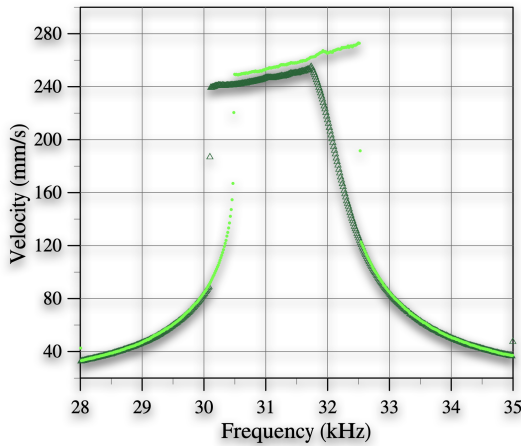
(c) $V_o = 22.5$ V
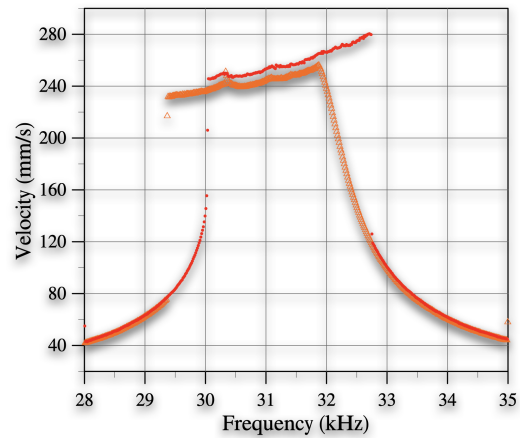
(d) $V_o = 25$ V

Figure 5.6: Up and down-sweep frequency-response curves show the tapping mode variations under $V_o = 20, 22.5,$ and 25 V

5.2.2 Pressure Sensor Characterization

We used the lock-in amplifier to obtain the frequency-response curves and the phase diagrams of the responses for another sensor. To establish a reference line for the experiments, we repeated the frequency-response curves of the electrostatic pressure sensor at excitation signals lower and higher than $V_o = 20\,\mathrm{V}$ (the excitation signal required to put the sensor in the tapping mode oscillation). The purpose of these two reference measurements is to compare the sensitivity of the proposed sensor to the pressure in both cases and select the best sensitivity detection mechanism (with or without bifurcation).

The results of the reference experiment are shown in 5.7. The results show a good match between the up and down-sweep curves before entering the tapping mode for both the velocity amplitude and phase. At the tapping mode, the results are different in both the velocity amplitudes and phases because of the hysteresis effect. Using the electrostatic signal for $V_o = 15\,\mathrm{V}$, the phase diagram of the velocity response shows a phase shift of $180°$ of the up and down-sweep curves. The same phase shift was obtained for up and down-sweep curves at the tapping mode; however, there were very significant jumps in the phase diagram at the start and end of the tapping modes. These jumps accurately identify the tapping's start, end, and bandwidth. Another difference between the phase diagram and the velocity amplitude of the frequency-response curves is that even small jumps in the velocity amplitudes will show up as significant jumps in the phase diagram. For example, the sensor's down-sweep frequency-response curve shows a very smooth curve before and after entering the tapping mode, which makes identifying the accurate start of the tapping mode oscillation challenging. However, the phase diagram can clearly show the start of the moment the sensor enters the tapping mode by a vertical jump on the phase shift at $24.163\,\mathrm{kHz}$. The bandwidth of the tapping mode is different in cases of the up and down-sweep frequency-response curves.

The frequency-response curves (without tapping) of the electrostatic pressure sensor under different ambient pressures ($200, 400, 600, 800,$ and $1000\,\mathrm{mbar}$) are shown in Figure 5.8. For pressure levels closer to the atmospheric pressure ($400, 600, 800,$ and $1000\,\mathrm{mbar}$), there were no noticeable differences in the velocity response curves. The significant difference was noticed when the pressure was lowered to $200\,\mathrm{mbar}$ where the velocity amplitude increased to $70.98\,\mathrm{mm/s}$ and $86.7\,\mathrm{mm/s}$ for the atmospheric pressure $200\,\mathrm{mbar}$, respectively. The phase diagrams 5.8 (b) for the sensor under the different ambient pressures are almost identical. The fact that no noticeable change was observed at pressures higher than $200\,\mathrm{mbar}$ in the frequency-response curves and/or the phase diagrams makes it harder to use them to identify the ambient pressure around the sensor. The results of the down-sweep frequency-response curve, 5.9 do not show any change from the up-sweep results.
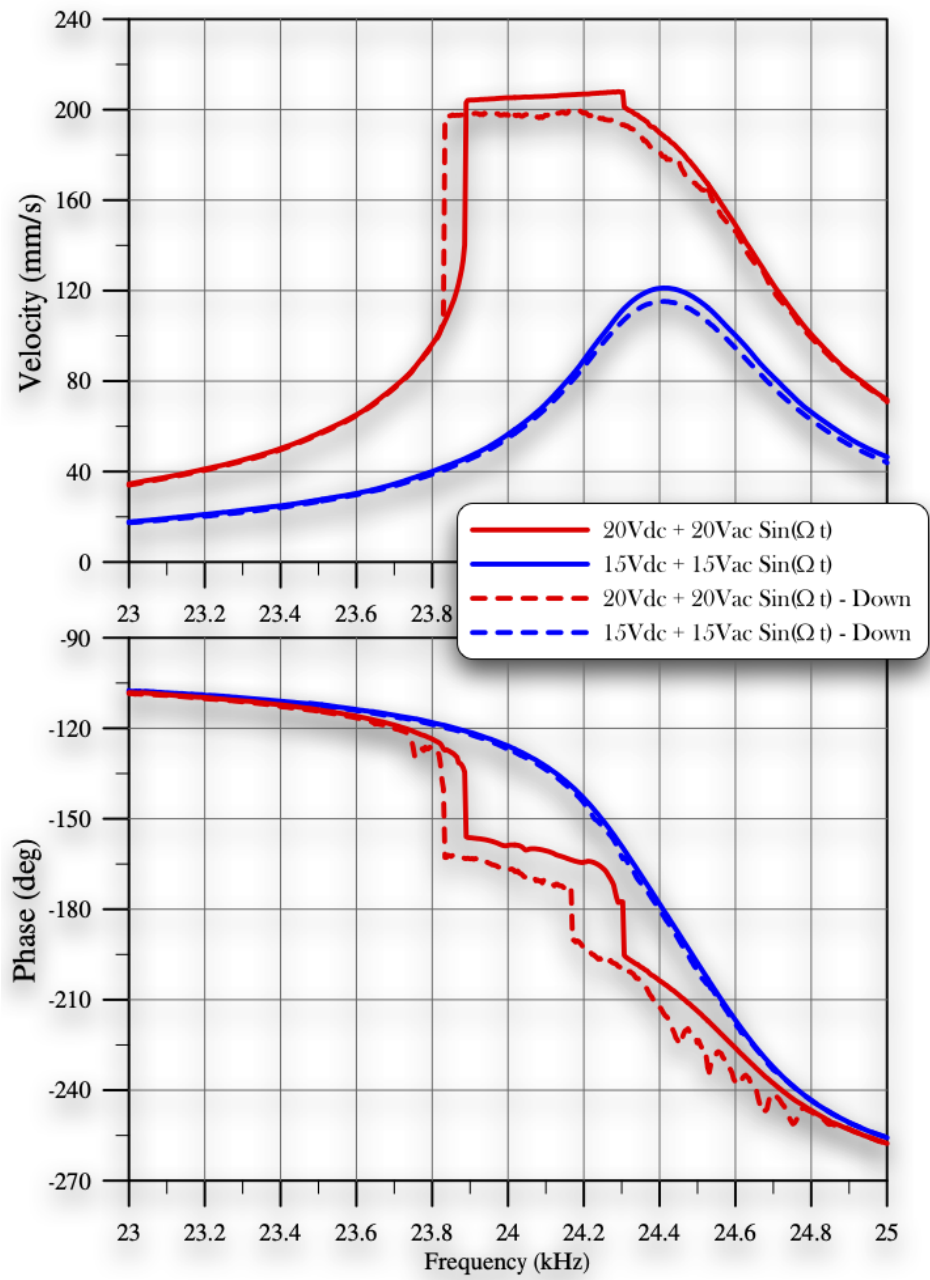
Figure 5.7: Frequency response curve and phase diagram of the electrostatic sensor in air
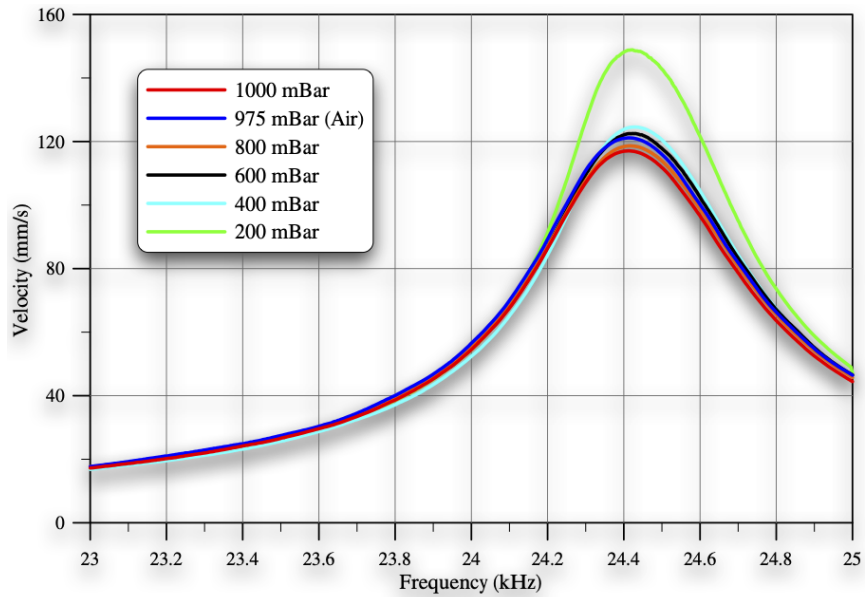
(a) up-sweep
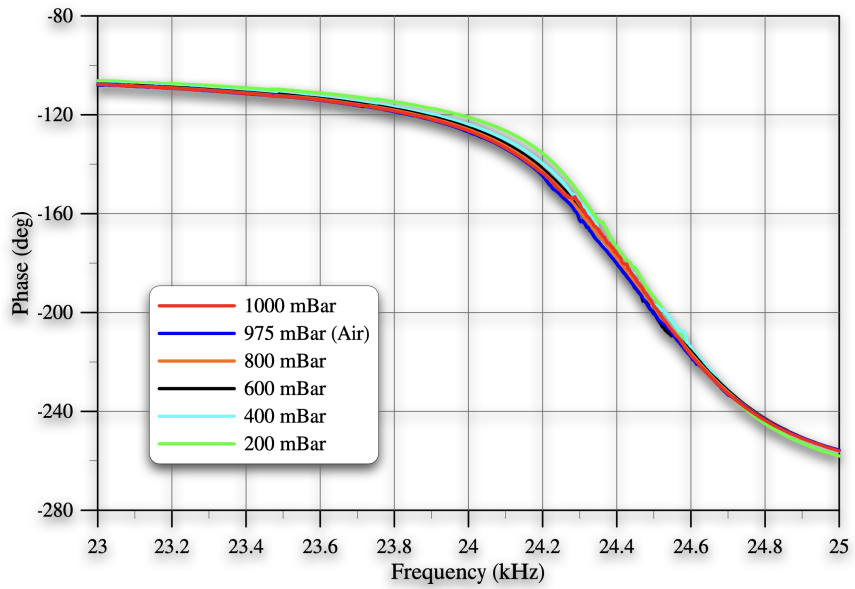
(b) Phase diagram

Figure 5.8: Effect of the pressure on the frequency-response curve and corresponding phase of the sensor in air using $V_o = 15\,\mathrm{V}$
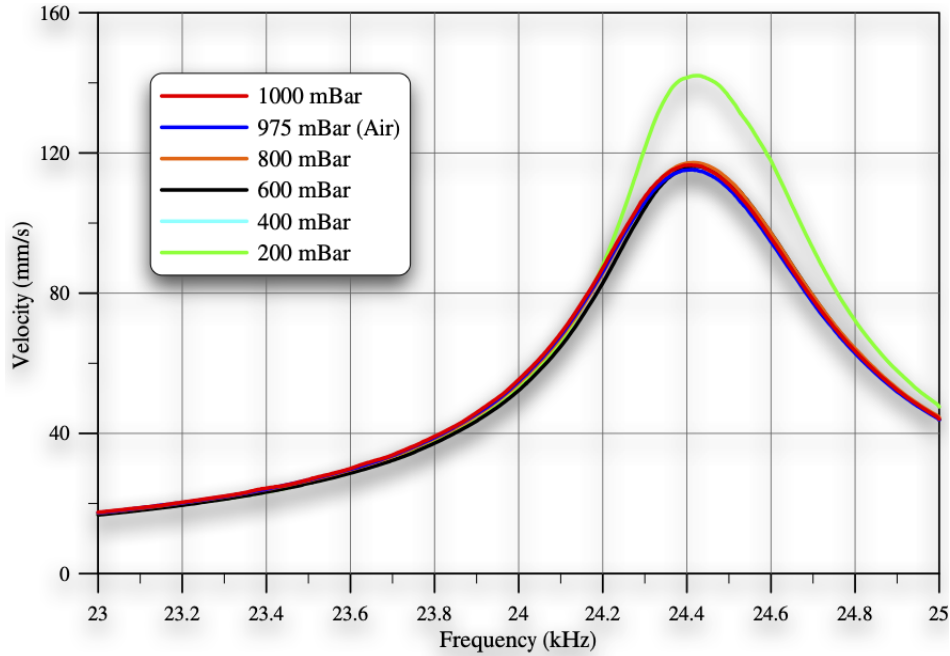
Figure 5.9: Frequency-response curve and phase diagram of the electrostatic sensor in the air

The frequency-response curves of the electrostatic pressure sensor at the tapping mode were recorded under different ambient pressures $(200, 400, 600, 800,$ and $1000\,\text{mbar})$. The up-sweep frequency-response curves and phase diagrams are shown in Figure 5.10. Under the same harmonic excitation $(V_o = 20\,\text{V})$, the velocity responses at the different pressure levels jump from the lower stable branch to the tapping mode oscillation at $23.89\,\text{kHz}$ excitation frequency. However, the sensor jumps back to the lower stable branch at different excitation frequencies. Table 5.1 summarizes the tapping's start, end for the frequency-response curves at tapping mode oscillation. The lower the ambient pressure, the wider bandwidth of the tapping mode oscillation.

There were jumps in the phase diagram at the start and end of the tapping mode oscillation. It seems that the phase diagram also has a stable phase branch and tapping mode phase branch. Once the sensor enters the tapping mode oscillation, the phase jumps from the stable phase branch to the tapping mode phase branch. No matter the tapping mode's bandwidth, the phase always jumps back to the stable phase branch. The lower the ambient pressure, the wider the tapping mode oscillation bandwidth, and the bigger jumps-back to the stable phase branch.

Table 5.1: Characterization of the tapping mode oscillation

Pressure (mbar)	up-sweep or down	Tapping's Start (kHz)	Tapping's end (kHz)	Tapping's Bandwidth (Hz)
200	Up	23.89	24.726	836
400	Up	23.89	24.529	639
600	Up	23.89	24.356	466
800	Up	23.89	24.264	374
1000	Up	23.89	24.249	359
200	Down	23.631	24.468	837
400	Down	23.712	24.338	626
600	Down	23.764	24.268	504
800	Down	23.802	24.221	419
1000	Down	23.831	24.166	335

The down-sweep frequency-response curves of the electrostatic pressure sensor under the tapping mode at the same pressure levels were plotted in Figure 5.11. The characteristics of the tapping mode oscillation are summarized in Table 5.1. The down-sweep curves shows different start and end of the tapping mode oscillation under different ambient pressures. In some cases of pressure loading, The tapping mode bandwidth is the same for the up and down-sweep curves.

From the previous results, we can conclude that the tapping mode gives quantitative and qualitative sharp changes (jumps-up, back, and down) in the velocity amplitudes and phases when the ambient pressure changes. Before the tapping mode, the change in the ambient pressure results in a slight change in the velocity response, which is less significant than the changes that happen in the tapping mode.

By comparing the frequency-response curves of the up and down-sweep, we found that the results of the up-sweep only show the jumps in the velocity amplitude and the phase diagram at the start of the tapping mode. However, the results of the down-sweep exhibit the jumps at the start and end of the tapping mode in both the velocity amplitude and phase. It is worth noting that we can relate the pressure to the tapping's start, end, or

bandwidth.

For the aforementioned reasons, we selected to use the phase diagrams of the down-sweep frequency-response curves at the tapping mode to generate the calibration curve of the proposed sensor. This phase diagram can accurately identify the tapping's start, end, and bandwidth. Figure 5.12 shows two examples of a pressure calibration curve generated from the frequency-response curves of Figure 5.11. A second-degree polynomial was selected for the curve fittings as follows.

$$P = a_1 f^2 + a_2 f + a_3 \tag{5.1}$$

where p is the pressure, f is the calibration parameter used, a_1, a_2, and a_3 are coefficients obtained from the curve fittings, Table 5.2. Using any of the calibration parameters, ambient pressure can be accurately identified.

Table 5.2: Fitting parameters of the pressure calibration curves

Calibration Parameter(f)	a_1	a_2	a_3
Tapping's start	0.0137	-647.817	7640294
Tapping's end	0.00629	-308.766	3787334
Tapping's bandwidth	0.00225	-4.239	2171

5.3   Conclusion

A novel electrostatic bifurcation pressure sensor was developed and tested. The sensor consists of a simple microstructure that can easily be fabricated using a multiuser or a custom fabrication process. It doesn't need wafer bonding, sealing, or any complex micro-fabrication process. Electrostatic bifurcation pressure sensor overcomes these limitations of temperature in the other pressure sensors. Unlike the other MEMS pressure sensors, the Electrostatic bifurcation pressure sensor doesn't need a large area or vacuum cavity to operate. The functional parameters of the bifurcation pressure sensor are independent of the design dimensions of the sensor. It also collects the advantages of low power cost, a wide range of operations.

The results of the frequency-response curves showed that the electrostatic bifurcation in-plane pressure sensor would be more sensitive to the pressure if the cyclic-fold bifurcation

mechanism was used as the detection mechanism. There were significant jumps in the phase diagrams at the start and end of the tapping mode oscillation. We concluded that the phase diagram of the down-sweep is the most sensitive measurement for pressure change. The electrostatic bifurcation in-plane pressure sensor is able to measure the ambient pressure by measuring the start, end, or bandwidth of the tapping mode oscillation.
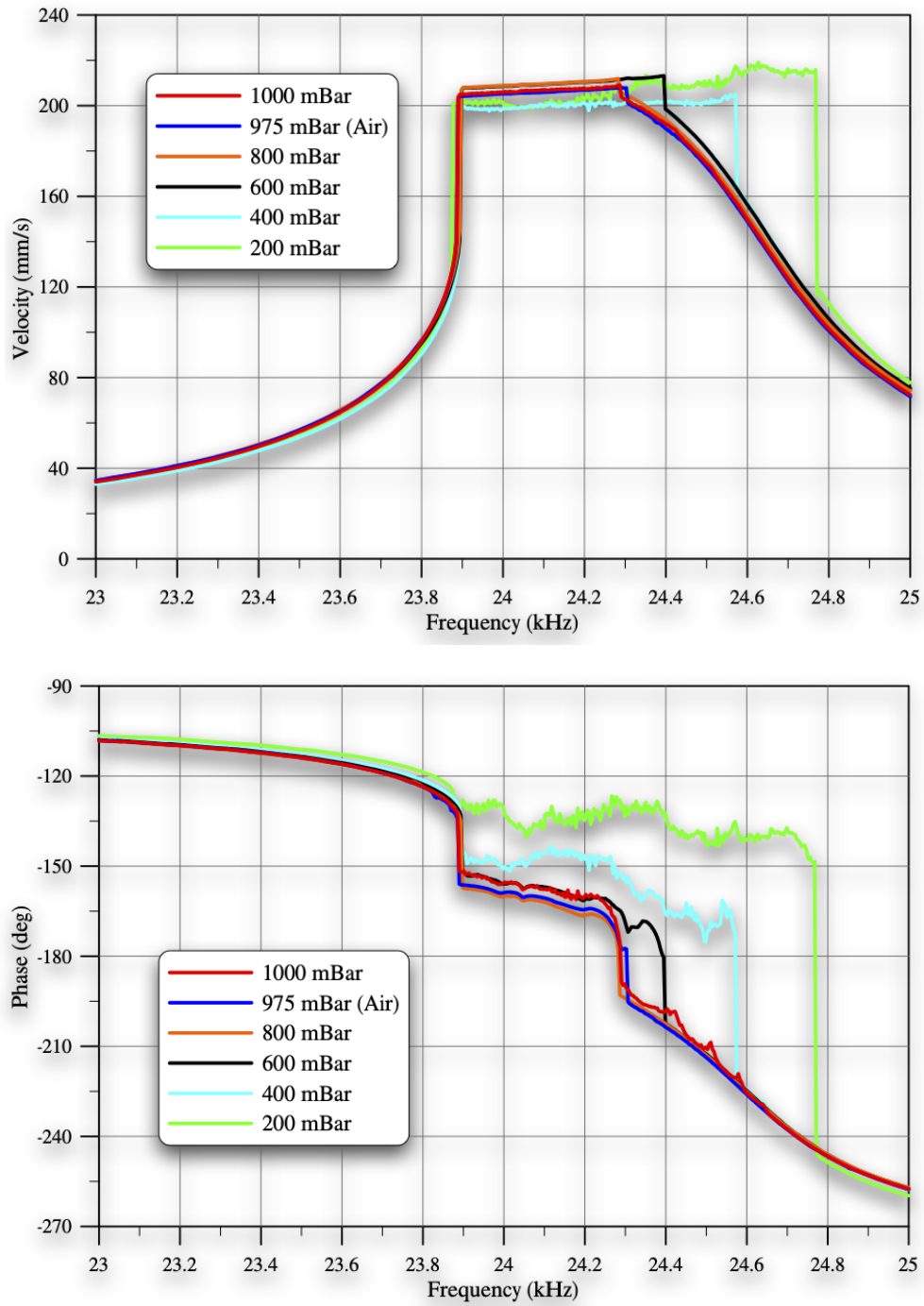
Figure 5.10: Effect of the pressure on the frequency-response curve and corresponding phase of the sensor in air using $V_o = 20\,\mathrm{V}$ when sweeping the frequency up.

67
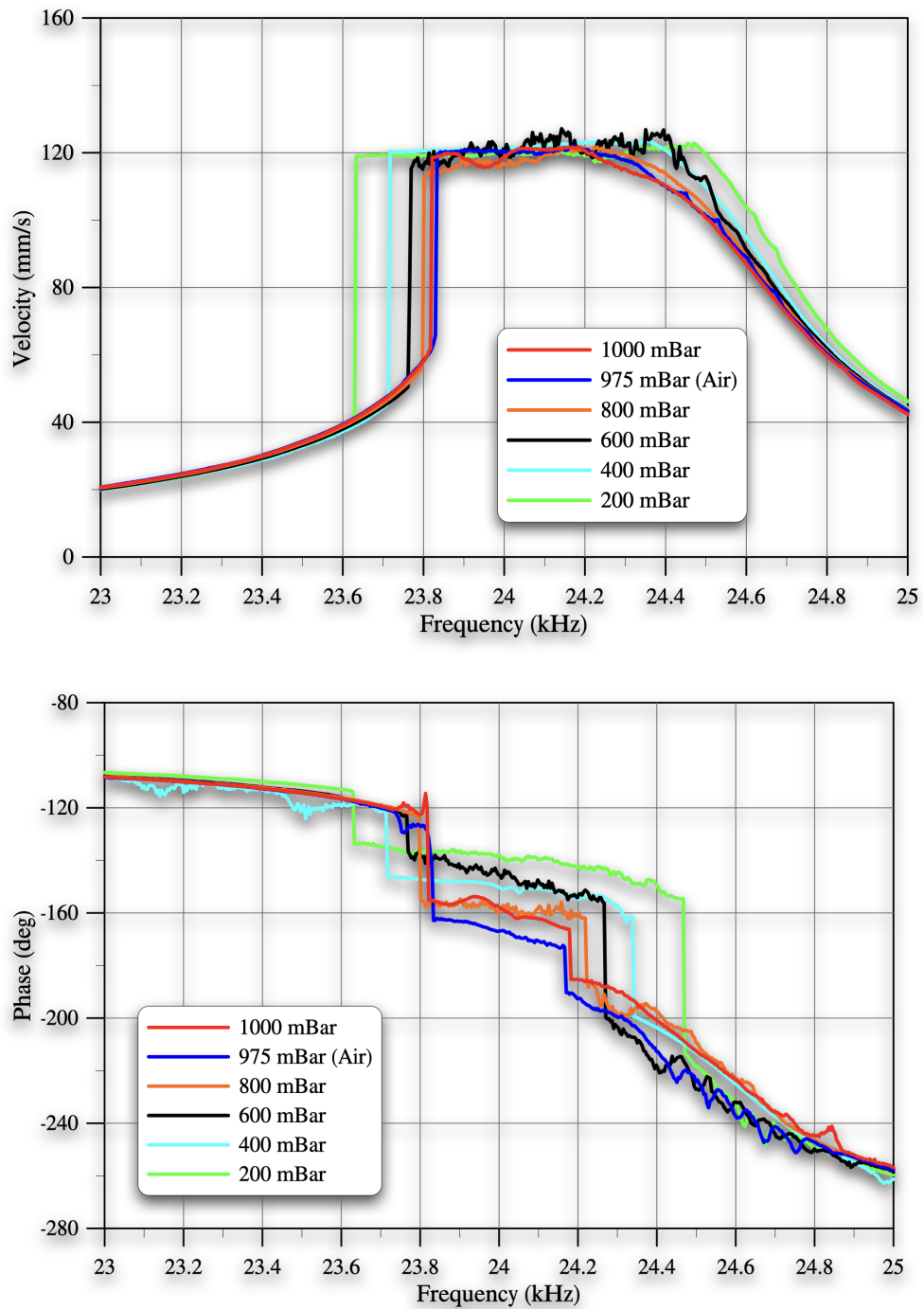
Figure 5.11: Effect of the pressure on the frequency-response curve and corresponding phase of the sensor in air using $V_o = 20\,\mathrm{V}$ when sweeping the frequency down.
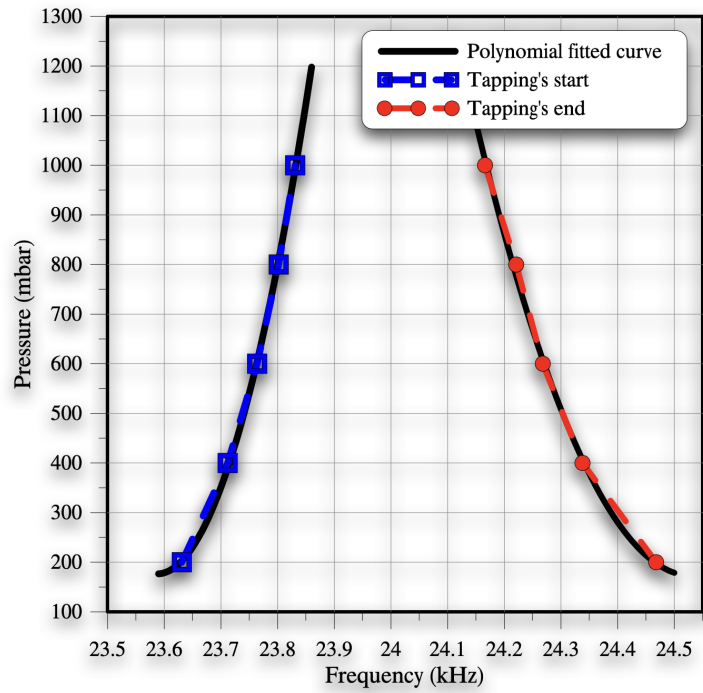
(a) using the tapping's start and end frequencies
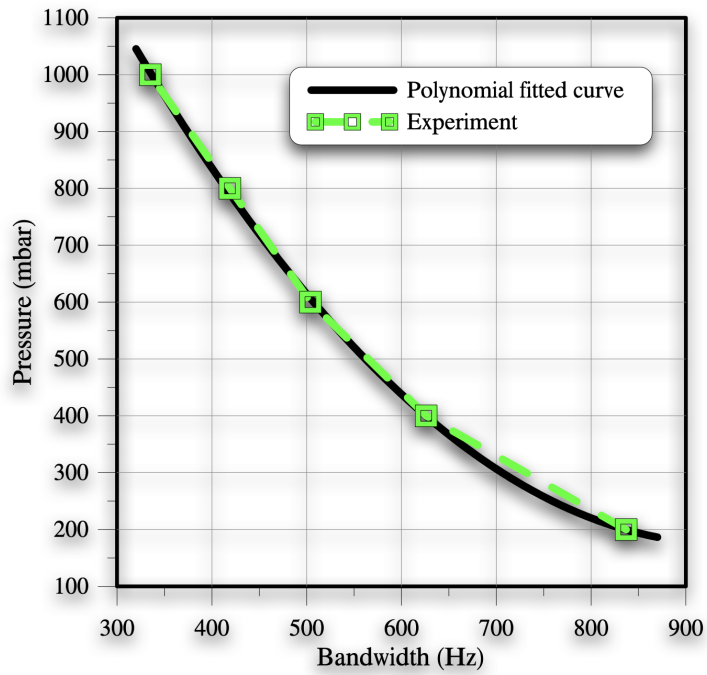
(b) using the tapping's bandwidth

Figure 5.12: Pressure calibration curves

Chapter 6

Electrostatic Bifurcation Gas Sensor

VOCs, such as hydrogen sulfide (H_2S), formaldehyde (HCHO), and benzene (C_6H_6) are widely released into ambient air as a result of industrial processes. The different forms of hydrogen sulfide produced by naturally occurring sulfate-reducing bacteria pose serious industrial process challenges to oil pipeline operators [72]. Furniture and paint are major sources of formaldehyde vapor indoors [73].

Frequent exposure to hydrogen sulfide can be lethal and infrequent exposure can lead to severe ocular, respiratory, neurological, cardiovascular, metabolic, and reproductive effects [74, 75]. Formaldehyde vapor in the indoor environment is a known health hazard [73].

Gas sensors can monitor the presence and concentration of VOCs in ambient air and provide a tool to protect against these dangers. The most common technologies used for gas sensing are solid-state sensors, electrochemical sensors, catalytic sensors, ionization sensors, and MEMS sensors [76]. Small size, high sensitivity [21], and compatibility with smart electronics technology [77] are important advantages for MEMS sensors. Inertial MEMS sensors are functionalized with detector material to absorb a target gas. They detect gas concentration via the resulting change in mass. The most widely used detector materials are polymers [21] and metal oxides [78].

Conducting polymers, such as polyaniline (PANI) and poly(2,5-dimethyl aniline) (P25DMA), are used as sensing materials due to their affinity to VOCs, the reversibility of their electrical and optical properties, low cost, and fabrication flexibility.

Mousavi et al. [79] demonstrated a resistive-type H_2S sensor based on thin-film PANI. The morphology of PANI can be enhanced to improve its sensitivity to H_2S by controlling synthesis conditions, such as the oxidant agent, monomer concentration, the ratio of the monomer to oxidant, and the reaction time and temperature [80].

Traditionally, inertial MEMS gas sensors [81, 82, 83] have employed static and dynamic detection modes. In the static mode, gas sorption is related to a structural displacement under the sorbed mass[83]. For example, Schlicke et al. [83] used the displacement of electrostatically actuated membranes to detect toluene at concentrations higher than 1000 ppm. In the dynamic mode, gas sorption is related to a frequency shift in a resonant peak [81, 82, 83, 84]. Dam et al. [84] used the shift in the resonance frequency of a clamped-clamped microbeam functionalized with polyacrylic acid (PAA) to detect sub-ppm concentrations of ammonia in air. Park et al. [85] detected 526 ppm of a VOC (toluene) in dry nitrogen using a frequency shift in the peak response of a Capacitive Micromachined Ultrasonic Transducer (CMUT) functionalized with poly(styrene-co-allyl alcohol) (PSAA). The use of sensor arrays equipped with multiple detector materials has been proposed as a method to improve the sensitivity and selectivity of gas detection. Possas-Abreu et al. [86] demonstrated an array of seven sensors equipped with various detector polymers for the detection of thirteen VOCs. Their best sensitivity was detecting 103 ppm of phenylacetate in dry nitrogen using a sensor functionalized with polyacetylene.

Bifurcation sensors were introduced recently [17, 21] as alternative inertial MEMS gas sensors. They exploit static and dynamic bifurcations in order to enhance the SNR. An equilibrium position or a periodic orbit experiences a sudden (qualitative) change in size at those bifurcations due to sorbed gas molecules. They have been shown to increase the size of the response signal to stimulus from a small incremental change, in the case of traditional sensors, to a larger qualitative change. Khater et al. [21] demonstrated a static bifurcation MEMS sensor made of a cantilever beam functionalized with P25DMA. They successfully detected 5 ppm of ethanol vapor in dry nitrogen. Kumar et al. [87] and Al-Ghamdi et al. [17] demonstrated a dynamic bifurcation sensor made of microcantilever beams. Functionalized with poly 4-vinyl pyridine, Kumar et al.'s [87] sensor was able to detect methanol vapor in dry nitrogen. In contrast, Al-Ghamdi et al.'s [17] sensor, functionalized with P25DMA, was able and detected 100 ppb of ethanol vapor in dry nitrogen.

In this chapter, we report on the further development of static bifurcation sensors to detect hydrogen sulfide as well as to detect formaldehyde and differentiate it from an interferent gas (benzene). The sensors use binary sensing mechanisms to detect the presence of the targeted gases at low concentrations. We also developed and deployed a novel method to functionalize those gas sensors.

6.1 Sensor Design and Characterization

The gas sensor was fabricated using a surface micromachining process, PolyMUMPs [88]. The main features of the PolyMUMPS are summarized in Appendix B. It was made of a $60\,\mu m \times 30\,\mu m$ sense-plate supported by two $125\,\mu m \times 5\,\mu m$ microbeams, Figure 6.1, fabricated in the Poly2 structural layer with a thickness of $1.5\,\mu m$. The plate design balances the need for a large surface area to facilitate sensor polymer deposition against the need to eliminate release holes that may lead to leakage of the carrying medium during functionalization. The bottom electrode is patterned underneath the sense-plate in the Poly0 layer.
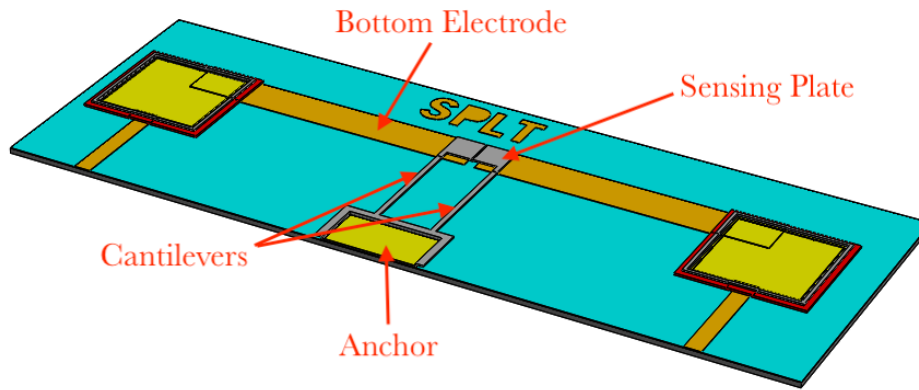
Figure 6.1: Layout of the gas sensor

A FEM modal analysis of the sensor was carried out using the COMSOL Multiphysics [89]. The 3D model of the sensor was built by defining the layout in the package MEMSPro and simulating PolyMUMPS fabrication steps in it. The resulting 3D model was imported into COMSOL. The mesh was made of 22,309 tetrahedral elements, 13,746 triangular elements, 1,724 edge elements, and 100 vertex elements with a total of 125,187 Degrees-of-Freedom (DOF). The minimum element size was $1.5\,\mu m$. The density, Young's modulus, and Poisson's ratio of the structural polysilicon were defined as per the fabrication process handbook [88, 90]. The boundary conditions imposed represent the fixed support of the beams at the anchor.

The first four mode shapes of the sensor are shown in Figure 6.2. The fundamental mode was the first out-of-plane bending mode with a natural frequency of $f_{o,1}{=}36$ kHz. The second mode shape was the first torsional mode (twists around x-axis) with $f_{t,1}{=}209$ kHz.

72

(a) 1st out-of-plane bending $f_{o,1}$=36 kHz

(b) 1st torsional mode $f_{t,1}$=209 kHz

(c) 1st in-plane bending $f_{i,1}$=260 kHz

(d) 2nd out-of-plane bending $f_{o,2}$=385 kHz
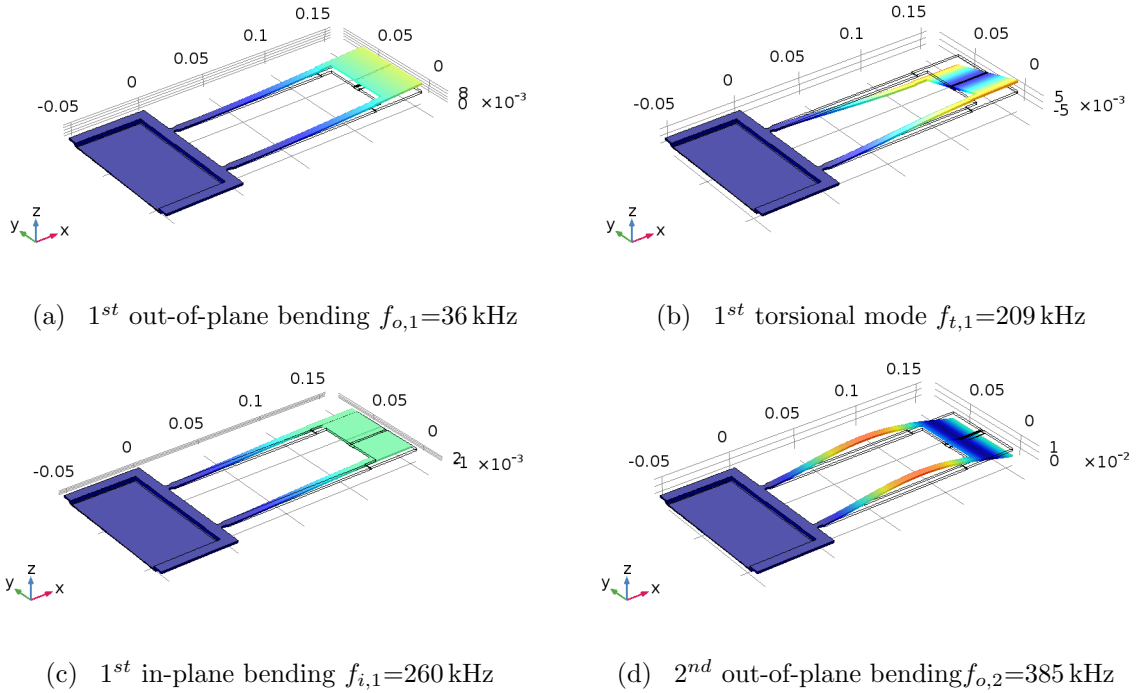
Figure 6.2: The first four modes of the gas sensor

The third mode was the first in-plane bending mode with $f_{i,1}$=260 kHz. The fourth mode shape was the second out-of-plane bending mode with a corresponding natural frequency of $f_{o,2}$=385 kHz. This distribution of the modes over the frequency domain indicates that, with their concomitant complications to sensor operation, modal interactions are unlikely.

The response of the fabricated sensor was investigated experimentally under thermal noise excitation by placing it in a vacuum chamber under a pressure of 0.005 mbar. A multi-point scan of the top surface of the sensor, Figure 6.3, shows that the dominant mode of response was the first out-of-plane bending mode.

An FFT of the first natural frequency of the sensor was found to be 34 kHz. The differences between the measured and calculated natural frequencies arise from micro-fabrication artifacts. Figure 6.4 shows one of those artifacts where the beam is over etched at the fixed end, thereby reducing the stiffness of the fabricated sensor.

The experimental setup of gas testing is the same as the experimental setup of the pressure testing described in section 5.1.2 and Figure 5.2.
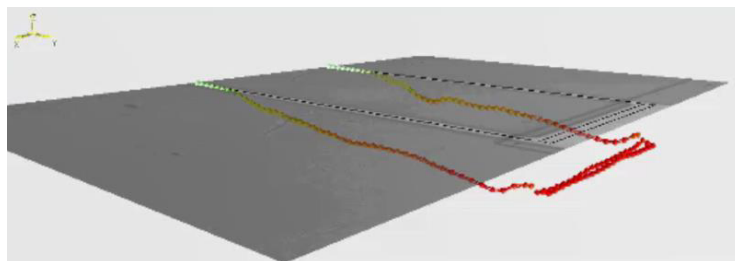
Figure 6.3: Experimental modal analysis of the sensor under the LDV.
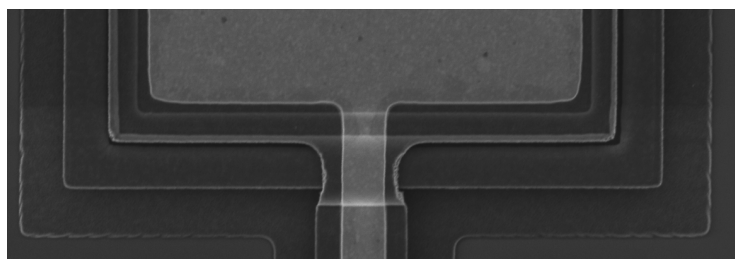
Figure 6.4: Defects of micro-fabrication processes

6.1.1 H$_2$S Sample Collection and Enrichment

A water sample containing Sulfate-Reducing Bacteria (SRB) was obtained from the General Petroleum Company, Egypt (GPC), with a salinity of 1.6% NaCl. This sample was used as a source of sulfidogenic microorganisms. The water sample was onsite inoculated on Postgate's-B medium and further incubated at 37°C for 14 days [91, 92]. The black precipitate (ferrous sulfide) was used as an indicator for growth and activity. In order to evaluate the hydrogen-sulfide H$_2$S production, the SRB sample was further enriched by inoculation with the enriched inocula and cultivation at 37°C for different incubation periods on Postgate's-C medium [92]. SRB count was estimated during the cultivation time using the Most Probable Number (MPN) [93].

In the other experiment, The target analyte gases contained 10 ppm of formaldehyde (F) and benzene (B) were utilized for evaluations. Pure nitrogen (Praxair grade 5.0) was used to purge samples (and/or parts of the experimental set-up) before actual testing.

6.2 Sensor Functionalization

6.2.1 Detector Polymer Evaluation

Four polymeric materials were selected and analyzed: PANI, P25DMA, poly(4-vinyl pyridine) (P4VP), and poly(acrylic acid) (PAAc). PANI and P25DMA show the best sorption ability of formaldehyde and benzene.

The test setup for sorption studies has been described previously in Stewart et al. work [94]. Each polymeric sensing material is exposed to a gas, and the amount of analyte that sorbs onto the sensing material is measured. If the sensing material being evaluated is sensitive to the target analyte, higher quantities of the analyte are sorbed. All sorption measurements are taken at room temperature (22 °C) and approximately 15 psi.

The setup exploits a difference in gas concentration (before and after exposure to the sensing material) to establish how much of the target analyte has been sorbed. Before exposure, a "blank" run can be analyzed by a highly accurate Varian 450 Gas Chromatograph (GC) (with a specialized Photon Discharge Helium Ionization Detector (PDHID) to determine the gas concentration for the case of no sorption. After exposure to the sensing material, the gas stream flows into the GC, distinguishing between similar analytes and recording concentrations down to the ppb level.

6.2.2 Deposition Method

A semi-automatic deposition method was developed to functionalize gas sensors. One gram of the detector polymer was mixed with 50 grams of a carrying medium. Ethylene glycol $(CH_2OH)_2$ was chosen as a carrying medium due to its low wettability of polysilicon surfaces and fast evaporation rate. The mixture was stirred for 15 minutes at a speed of 300 RPM to ensure equal dispersion of the detector polymer in the carrying medium.

A microfluidic pump drove the mixture at a $0.1\,\mu$L/minute flow rate through a pipe-pipette assembly supported by a microprobe to deposit a droplet of the mixture on the sense plate. Figure 6.5 shows the experimental setup. Ethylene glycol was allowed to evaporate naturally, leaving the detector polymer on top of the sense plate. The process was continued for at least 10 minutes until the detector polymer covered most of the sense plate. Figure 6.6 shows sensor samples during and after functionalization.

Nitrogen flow was introduced for 15 minutes. The frequency-response curve of the sensor was obtained by applying a pulse train of 5 V amplitude, 1 kHz frequency, and 10 μs

Figure 6.5: The experimental setup for sensor functionalization.

pulse width. The velocity of the plate's center point was measured using the LDV. FFT of the measured velocity before and after functionalization were calculated. The added mass of the polymer onto the sensor shifted the frequency of the maximum velocity down from 23 kHz to 22 kHz, corresponding to a polymer mass of 0.522 ng, and reduced the peak velocity from 380 mm/s to 295 mm/s.

A sawtooth signal varying from 0 V to 6.8 V at a frequency of 5 Hz was applied to the bottom electrode in a dry nitrogen environment to measure the static pull-in voltage. Pull-in voltage was detected as a sudden change in the plate displacement where the slope of the displacement-voltage curve approaches infinity. After five trials, the mean and standard deviation of the measured pull-in voltage was calculated, Table 6.1. The results show that the mean of the pull-in voltage drops from 6.543 V to 6.264 V before and after the polymer deposition, respectively. This difference is due to the added mass of the detector polymer. The standard deviation, representing the influence of circuit and other environmental noise sources, was calculated to be 1.8 mV for the sensor blank and functionalized sensors, respectively.

Figure 6.6: (a) The sensor and pipette during the deposition process and (b), (c), and (d) functionalized sensors.

6.3 Experiments

6.3.1 Hydrogen Sulfide Sensor

The resulting H₂S gas at different cultivation periods (1, 3, and 5 days) was collected, and its concentration was measured by Dräger Tubes (2-60 ppm) approved by NIOSH (Method/TCA/A-012), and the American Industrial Hygiene Association (AIHA). Furthermore, the measurements were confirmed by GC following the (ASTM) Method D5623. The H₂S gas concentrations were found to be 20, 40, and 60 ppm, respectively.

The target gas was released into the gas chamber by passing a stream of dry nitrogen into the head air of a vial containing an SRB sample cultivated for one day. After five

Table 6.1: Pull-in for the sensor with and without polymer under sawtooth loading

Pull-in (V)	1	2	3	4	5	Avg.	St. Dv
Blank	6.541	6.541	6.545	6.541	6.545	6.542	0.002
Functionalized	6.262	6.266	6.263	6.260	6.264	6.262	0.002

minutes of releasing H_2S into the gas chamber, a sawtooth voltage signal varying from $0\,V$ to $6.4\,V$ at a frequency of $3\,Hz$ was applied to the substrate electrode to detect the pull-in voltage of the sensor. The pull-in voltage in the presence of H_2S was found to be $6.264\,V$, which is the same value for the pull-in voltage in dry nitrogen. Thus, indicating failure to detect the gas. The H_2S release period was then increased to fifteen minutes. The pull-in voltage detected under this condition was $6.257\,V$. The detection voltage, defined as the difference between pull-in voltage in the presence and absence of H_2S, was $7\,mV$ well above standard deviation, proving that the gas can be detected at a 20 ppm concentration under well-mixed conditions.
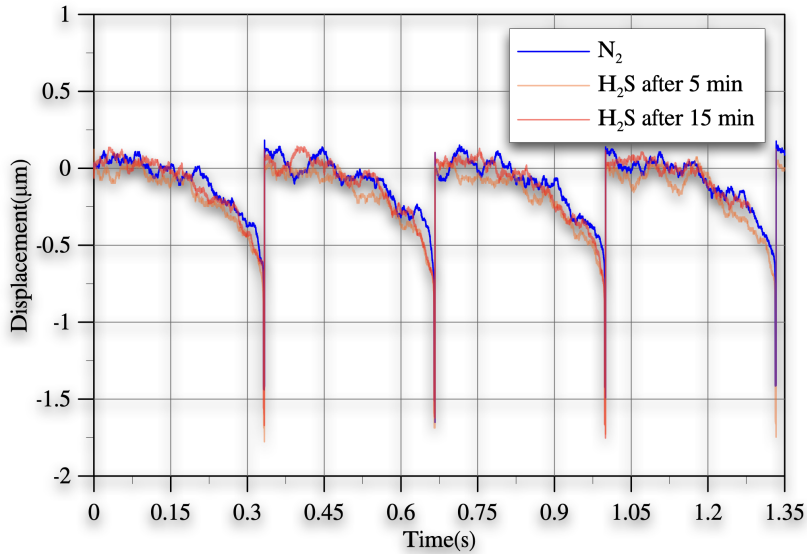
Figure 6.7: Displacement of the gas sensor before and after releasing the gas using a sawtooth signal excitation of 3Hz frequency

6.3.2 Formaldehyde Sensor

Testing the formaldehyde and benzene (F and B) was conducted in two steps. First, we measured each gas individually as a target gas to determine the detection voltage and minimum concentration that can be detected for this gas. Second, two gases are mixed up and released in the gas chamber. The formaldehyde was selected as the target gas and the benzene as the interferent gas.

Dry nitrogen gas was introduced into the chamber for fifteen minutes. The dielectric charge on the sensor was measured and recorded. A DC load was then applied to the sensor and increased at a rate of $1 \, \text{mV} / 30 \, \text{seconds}$ until the sensor pulled in. After this, the nitrogen supply was shut down. The pull-in voltage for the nitrogen was calculated and recorded.

The target gas F or B was introduced to the gas chamber at the desired concentration ($10 \, \text{ppm}$, $5 \, \text{ppm}$, $2 \, \text{ppm}$, and $1 \, \text{ppm}$). The dielectric charge on the sensor and the pull-in voltages were measured in the same manner. The experiment was repeated at least three times, and the results were tabulated. The mean and standard deviation of the detection voltages for both of the detector polymers (PANI and P25DMA) at different levels of target gases concentrations are listed in Table 6.2.

The results indicate the sensor's ability to detect both formaldehyde and benzene at low concentrations. PANI was found to be more sensitive to both formaldehyde and benzene than P25DMA. The minimum detectable concentration of formaldehyde using PANI was found to be $1 \, \text{ppm}$, while the minimum detectable concentration of benzene was found to be $2 \, \text{ppm}$ for PANI. Therefore, setting the sensor equipped with PANI to a detection voltage of $3 \, \text{mV}$ allows for detecting formaldehyde while rejecting benzene. At this level, the detection voltage is well above the circuit noise level at $1.8 \, \text{mV}$ and the overall sensor repeatability (standard deviation) threshold of $1.8 \, \text{mV}$. The minimum detectable concentration of formaldehyde using P25DMA was found to be closer to $5 \, \text{ppm}$, while the minimum detectable concentration of benzene using P25DMA was found to be about $10 \, \text{ppm}$.

6.4 Conclusions

An electrostatic bifurcation gas sensor was designed and fabricated using the PolyMUMPS surface micromachining process. The sensor was functionalized with the detector polymer polyaniline (PANI) using a new deposition method. We demonstrated the detection of hydrogen sulfide H_2S resulting from SRB using the static bifurcation MEMS gas sensor. The limit of detection was found to be less than 20 ppm.

Table 6.2: The mean and standard deviation of the detection voltage, in mV, for combinations of detector polymers and test gases

| | HCHO | | | |
	10 PPM	5 PPM	2 PPM	1 PPM
P25DMA	3.6 ± 0.57	1 ± 2		
PANI	8 ± 4.73	7.83 ± 8.56	9 ± 8.22	3 ± 1.41

| | C_6H_6 | | | |
	10 PPM	5 PPM	2 PPM	1 PPM
P25DMA	2.66 ± 0.58	-2.33 ± 3.21		
PANI	7.5 ± 3.53	7.4 ± 3.64	7 ± 8.2	

The electrostatic bifurcation gas sensor was used to differentiate formaldehyde from benzene. First, the minimum detectable concentration of the two VOCs was measured for the two detector polymers: PANI and P25DMA. We found that PANI could detect the formaldehyde down to 1 ppm in dry nitrogen, and it can detect the benzene down to 2 ppm. On the other hand, P25DMA could detect formaldehyde and benzene down to 5 ppm. The functionalized sensor with PANI could selectively detect formaldehyde in the presence of benzene as an interferent gas.

Chapter 7

Electrostatic Bifurcation Underwater Sensor

The oceans and seas are typically regarded as pristine environments. But in reality, it is contaminated by pollutants: heavy metals such as mercury and lead [95]. The mercury can enter the food chain. The emitted mercury circulates the globe and eventually accumulates in water-laid sediments where it is converted into toxic methylmercury[96]. It may accumulate in organisms like fishes, so it has a direct effect on organisms and an indirect effect on humans. Methylmercury can easily enter the gastrointestinal tract, blood, and brain[97]. As a consequence, it impairs hearing and vision, causes reproductive failure and tremors. When consumed in high doses, it may cause death for either fish or humans.

The two main sources of mercury's emission in air can be classified as primary natural sources, and primary anthropogenic sources [98]. Volcanoes, forest fires, and geothermal activity are considered natural sources of mercury emissions in air. Additionally, mercury can be reemitted from the evaporation of ocean water. Industries include burning fossil fuels, mining for various metals, cement production, and medical-related industries, are the primary anthropogenic sources of mercury in air. Globally, burning fossil fuels is the major anthropogenic source of mercury in air; it accounts for about 40% of all manufactured mercury emissions.

According to the U.S. Environmental Protection Agency's 2014 National Emissions Inventory report [99], electricity generation units that burn coals are the major contributor to mercury emission by about 22.9% in 2014. The second emission source was Electric Arc Furnaces by 5% while the third contributor was industrial applications like the Portland cement, institutional boilers, and process heaters.

In Canada, mercury emissions amounted to $5300\,\mathrm{kg}$ in air and $240\,\mathrm{kg}$ in the water in 2010 [100]. The major emission comes from electrical power generation and wastewater treatment. The Province of Ontario was the biggest source of the emitted mercury in air in the last three decades[100].

Observation of mercury in the water surface becomes an essential requirement for keeping the environment safe. In this chapter, we are proposing an electrostatic bifurcation underwater sensor to detect mercury in water. We present the basic concepts of the sensor design and characterization.

7.1   Sensor Design

7.1.1   Design Criteria

To design an electrostatic bifurcation underwater sensor, stiffness, damping, and electrostatic force should be carefully considered. As far as we know, squeeze film damping is the dominant source of damping in MEMS[26]. Fluids like air and liquids can resist the compression or tension stresses; however, it doesn't show a noteworthy resistance to shear stress. Therefore, sensors that are designed to move in-plane are expected to exhibit higher quality factors (Q) and lower damping than the traditional out-of-plane sensors[25, 28].

Additionally, operating the MEMS in a liquid environment reduces the quality factors significantly because of the liquid's viscosity and added masses onto the sensor. Degradation of Q in the case of actuating in-plane is smaller than the case of actuating it out-of-plane [56, 101]. Again, this feature gives the in-plane actuation a substantial advantage over the out-of-plane actuation.

To avoid the effect of the external disturbances (vibrations), the underwater sensor was designed to have a fundamental natural frequency greater than $10\,\mathrm{kHz}$. Modal interactions should be avoided in the sensor's design. As a result, the sensor was designed to have none of the lower modes at multiple integers of the fundamental frequency. Modal analysis of the underwater sensor was carried out to identify the natural frequencies and ensure that they are well separated from each other, as described in Section 7.1.2.

Considering the functionalization process of the detector polymer onto the microbeam, the sensor should have a wide microbeam area to deposit a suitable amount of the detector polymer. This area should also reduce the chance of overflow of the detector polymer underneath the microbeam to prevent the stiction of the microbeam to the substrate. To do this, the sensor was designed as a microcantilever with a large top surface area to

Table 7.1: Dimensions of the underwater sensors

Length(μm)	width(μm)	Side Gap (μm)
200	16	2
200	16	3
200	20	3
200	24	3
250	24	3

improve the sensor's capacitance to carry the detector polymer. The sensor was designed according to PolyMUMPs fabrication process[88], Appendix B. Variable dimensions of the sensor were also considered in the design to give a wider range of applications. The dimensions variation of the underwater sensor is described in Table 7.1.

7.1.2 Modal Analysis

A FEM modal analysis of the sensor was carried out using COMSOL Multiphysics commercial software [89] to analyze the natural frequencies and mode shapes of the underwater sensor. The 3D model of the sensor was built using MEMSPro [102] software by drawing the 2D layout then defining the PolyMUMPS fabrication steps.

The generated 3D model, Figure 7.1 (a), is then transferred to COMSOL so that the parameters of the FEM problem can be defined. The physics was defined as Solid Mechanics, and an eigenfrequency solver was used. The material density, Young's modulus, and Poisson's ratio were defined for the polysilicon [88]. The boundary conditions were defined as fixed at the anchor and free everywhere else. Then the mesh was created, Figure. 7.1 (b). The statistics of the mesh were 27918 tetrahedral elements, 13535 triangular elements, 2507 edge elements, and 96 vertex elements. The minimum element size was 1.5μm. The FEM solver solved for 138627 DOF, and the first 25 eigenfrequency were calculated.

The first six out-of-plane mode shapes are plotted in Figures 7.2 (a) to (f). All the out-of-plane mode shapes are the traditional known out-of-plane bending modes for the cantilever. The fundamental mode was the first out-of-plane bending mode, and it appeared at a natural frequency of $f_{o,1}$=123.6 kHz. The other out-of-plane mode shapes took places at $f_{o,2}$=772 kHz, $f_{o,3}$=2.146 MHz, $f_{o,4}$=4.165 MHz, $f_{o,5}$=6.8 MHz, and $f_{o,6}$=10 MHz, in order.

The in-plane mode shapes, Figure 7.2 (g -k), show that the first in-plane mode shape

(a) 3D Model   (b) Mesh
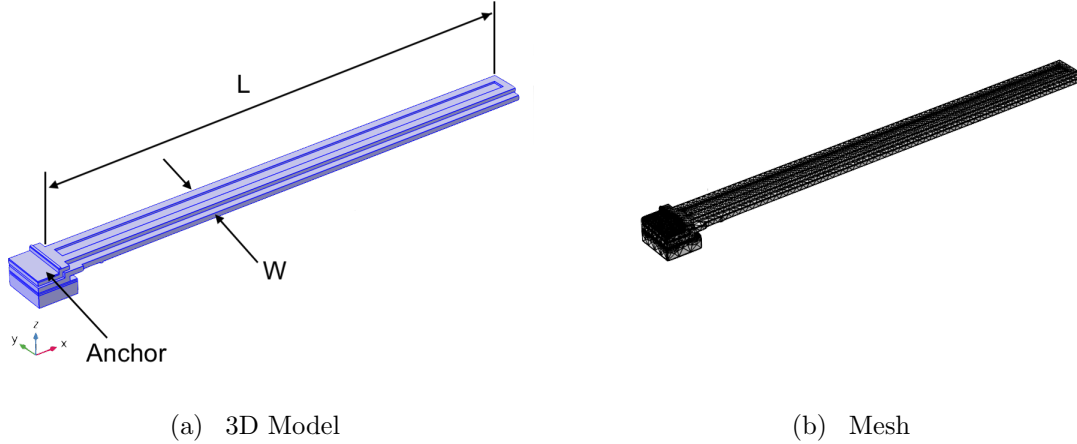
Figure 7.1: FEM of the electrostatic bifurcation in-plane underwater sensor

occurs at $f_{i,1}$=428 kHz, where the microbeam is bent in-plane, and the cantilever's free end has maximum displacement. The second in-plane bending mode takes place at $f_{i,2}$=2.63 MHz. The third, fourth, and fifth in-plane mode shapes can be noticed at $f_{i,3}$=7.14 MHz, $f_{i,3}$=13.4 MHz, and $f_{i,4}$=21.1 MHz, respectively. Because of the nature of the surface micromachining process (PolyMUMPS), it is expected that the in-plane natural frequencies will have higher values than the out-of-plane natural frequencies. The results of the in-plane bending mode shapes achieve the design consideration (high in-plane natural frequencies and the wide frequency bands separating between them). For tests and the experimental characterization, The first and second mode shapes will be considered. Twisting mode shapes have also appeared in the FEM results. The first six twisting mode shapes took place at 2.2 MHz , 6.67 MHz , 11.1 MHz , 15.7 MHz , 20.2 MHz , and 24.9 MHz, respectively.

7.2   Basic Characterization

Visual inspection was first performed on the sensor to ensure that the structure is well released and that neither cracks nor other undesired features exist in the sensor. A SEM image of the underwater sensor is shown in Figure 7.3. The geometry of the fabricated sensor was investigated under Contour Elite I 3D Optical Microscope from BRUKER [103]. Topography of the underwater sensor, Figure 7.4, show that the fabricated dimensions

(a) 1st out-of-plane mode shape at 123.6 kHz

(b) 2nd out-of-plane mode shape at 772 kHz

(c) 3rd out-of-plane mode shape at 2.146 MHz

(d) 4th out-of-plane mode shape at 4.165 MHz

(e) 5th out-of-plane mode shape at 6.8 MHz

(f) 6th out-of-plane mode shape at 10 MHz

(g) 1st in-plane mode shape at 428 kHz

(h) 2nd in-plane mode shape at 2.63 MHz

(i) 3rd in-plane mode shape at 7.14 MHz

(j) 4th in-plane mode shape at 13.4 MHz

(k) 5th in-plane mode shape at 21.1 MHz

Figure 7.2: Modal analysis of the electrostatic bifurcation in-plane underwater sensor

match the designed dimensions.

Mechanical response of the underwater sensor was investigated optically using MSV-400 and UHF-120 LDVs from Polytec [45] and electrically using HF2LI Lock-in Amplifier from Zurich instruments [104]. The out-of-plane and in-plane motions were investigated. The in-plane experimental setup under the LDV was explained previously in Chapter 2. The cantilever's tip was considered for the optical measurements, but the whole structure movement was considered in the current measurement.

First, the modal response of the sensor was tested by placing the underwater sensor in a vacuum chamber at 0.005 mbar. The microbeam was grounded, and a white noise signal of 0 V mean and 25 V standard deviation was applied on the side electrode of the sensor
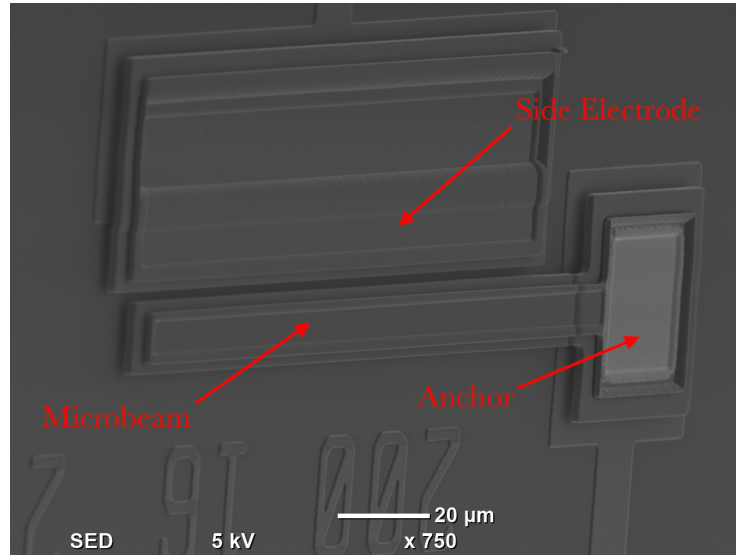
Figure 7.3: SEM of the underwater sensor

to cover a broad band of actuation frequencies.

The experimental setup was switched to the in-plane experimental setup, and the same actuation signal was applied. The modal response of the sensor under the random noise excitation for the out-of-plane and in-plane are plotted in Figure 7.5. The first peak in the frequency-response was observed in the out-of-plane measurements at 117.3 kHz, representing the first out-of-plane natural frequency. Its corresponding mode shape is shown in the FEM results, Figure 7.2(a). The second out-of-plane natural frequency was observed at 650 kHz. Comparing the natural frequencies of the sensor with the FEM simulation results, Figure 7.2 (a) and (b), we find that the experimental results of the natural frequencies are close to the FEM results, which means that the fabrication process didn't change the mechanical properties of the MEMS structure. Those results also indicate that the fabricated sensor is well released and functionally working per design.

The first and second in-plane mode shapes were observed at 435 kHz and 2.7 MHz, Figure 7.5. Their corresponding mode shapes are shown in Figure 7.2 (g) and (h). The experimental results match the calculated results of the FEM. It should be noted that the first and the second in-plane natural frequencies will be used for underwater sensing purposes.

The frequency-response curve of the underwater sensor was obtained by sweeping the excitation frequency while holding the voltage waveform constant. An AC signal of 50 V
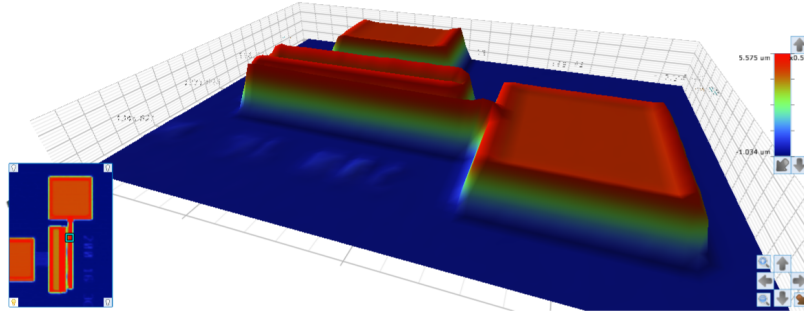
(a)   Topography
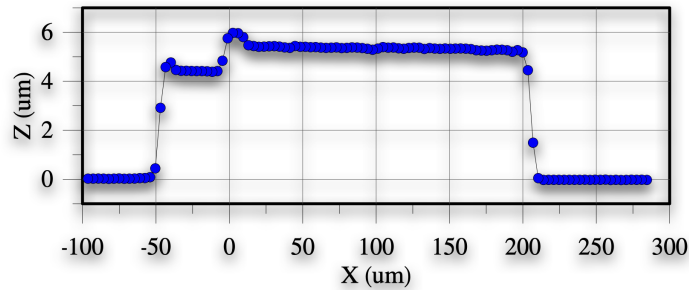
(b)   Cross-section

Figure 7.4: Topography of the underwater sensor

amplitude was used in this experiment. AC signal was preferred to eliminate electrolysis.

Electrolysis happens when ample electrical power is applied on the H_2O molecule, which is enough to break down the bond between the H and O_2, transforming them into gases. Electrolysis can be produced by applying low DC voltage as low as $1.23\,V$ across two submerged electrodes in the deionized water[105, 106]. Electrolysis is one of the major challenges in testing underwater because it changes the damping and electrical permittivity of the system. This was the main reason for using an AC signal in most experiments.

For a given frequency Ω, the RMS of 60 periods was calculated to obtain the Frequency-response curves of the underwater sensor. The frequency-response curves of the first and second out-of-plane bending modes, Figure 7.6, were found by sweeping the excitation frequency from $90\,kHz$ to $120\,kHz$ and $600\,kHz$ to $700\,kHz$, respectively, in one second period. The frequency-response curves of the first and second in-plane bending modes,
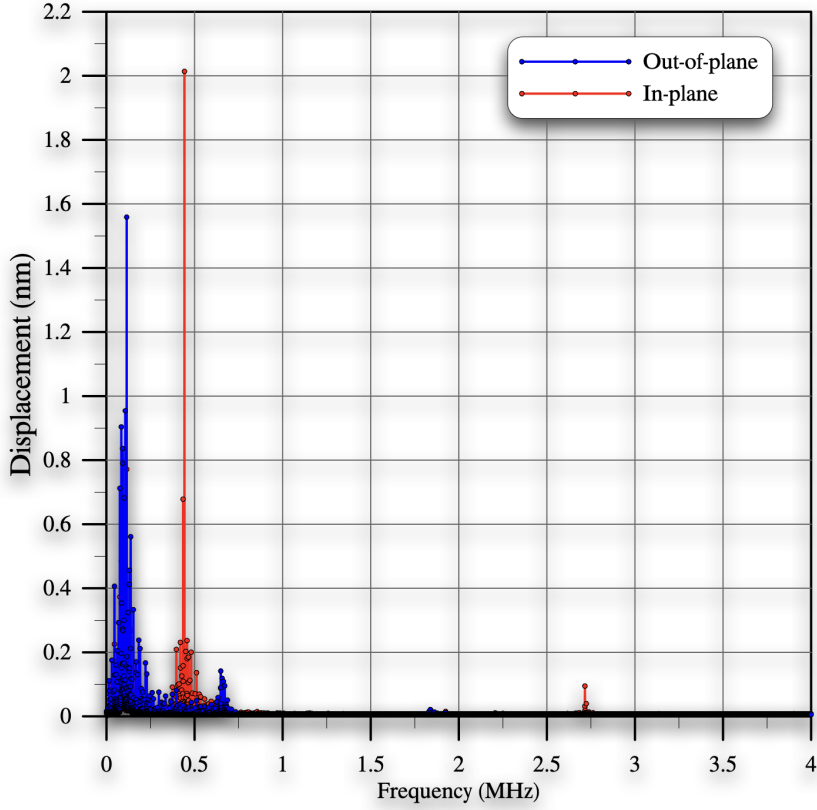
Figure 7.5: Frequency-response of the underwater sensor under a white noise signal of $0\,\mathrm{V}$ mean and $25\,\mathrm{V}$ standard deviation

Figure 7.7, were found by sweeping the frequency from $425\,\mathrm{kHz}$ to $445\,\mathrm{kHz}$ and $2.6\,\mathrm{kHz}$ to $2.8\,\mathrm{MHz}$, respectively, in one second period.

The natural frequencies of the first two out-of-plane modes were observed at $f_{o,1}=103\,\mathrm{kHz}$ and $f_{o,2}=658.5\,\mathrm{kHz}$, respectively. Quality factors were estimated using the half-power band-width method, Eq. 3.1. For the out-of-plane modes, the quality factors were found to be $Q_{o,1}=2.2$ and $Q_{o,1}=25$.

Applying an AC signal of $50\,\mathrm{V}$ amplitude onto the sensor to plot the frequency-response curve at the expected first in-plane natural frequency showed an unknown motion closer to the natural frequency. These strange motions may be explained as out-of-plane motions that were generated at this point. Exciting the sensor in-plane with an excitation that exceeds a specific threshold of the structure could pump the power of the microcantilever into the fundamental mode shape of the structure, which, in this case, is out-of-plane.
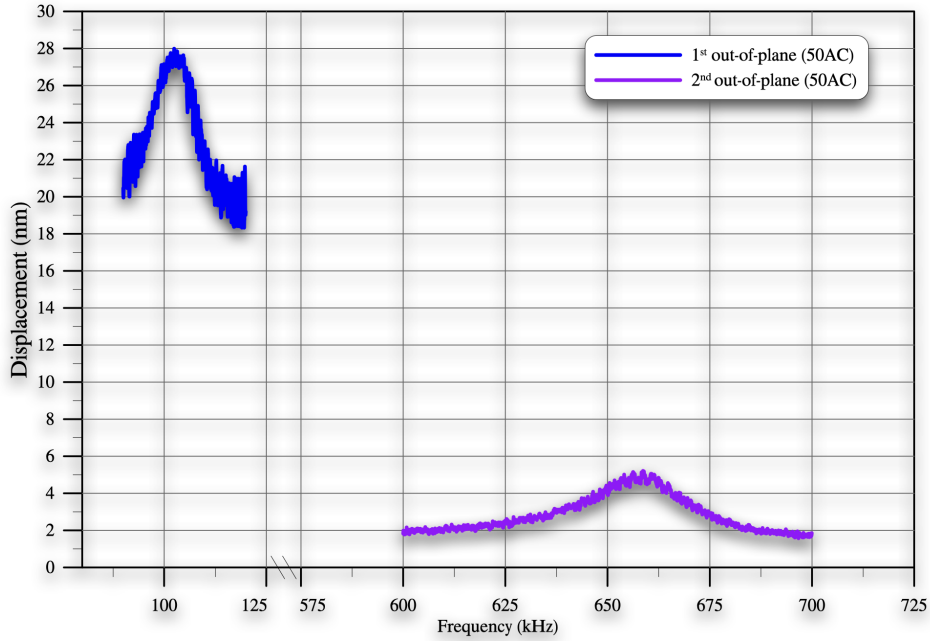
Figure 7.6: Frequency-response curves of the first and second out-of-plane bending modes.

This explanation is close to the definition of the parametric excitation of a microstructure. To avoid this issue, the sensor has been excited with 12.5 V AC and 12.5 V DC. The frequency-response curve is plotted in Figure 7.7.

The first in-plane natural frequency was found at $f_{i,1}$=438 kHz. The quality factor of the first in-plane natural frequency was $Q_{i,1} = 97.5$. The second in-plane natural frequency was found at $f_{i,2}$=2.72 MHz and its quality factor was $Q_{i,2} = 680$. It is noticed that the quality factors for the in-plane natural frequencies are much higher than the quality factors of the out-of-plane natural frequencies.

The underwater sensor top surface's area wasn't large enough to carry an appropriate amount of the detecting polymer. The beam tends to stick to the substrate, and small mechanical responses of the sensor were the main limitations of the first generation of the underwater sensor. To improve the under sensor design, a second generation of the underwater sensor was developed and fabricated, Appendix C.
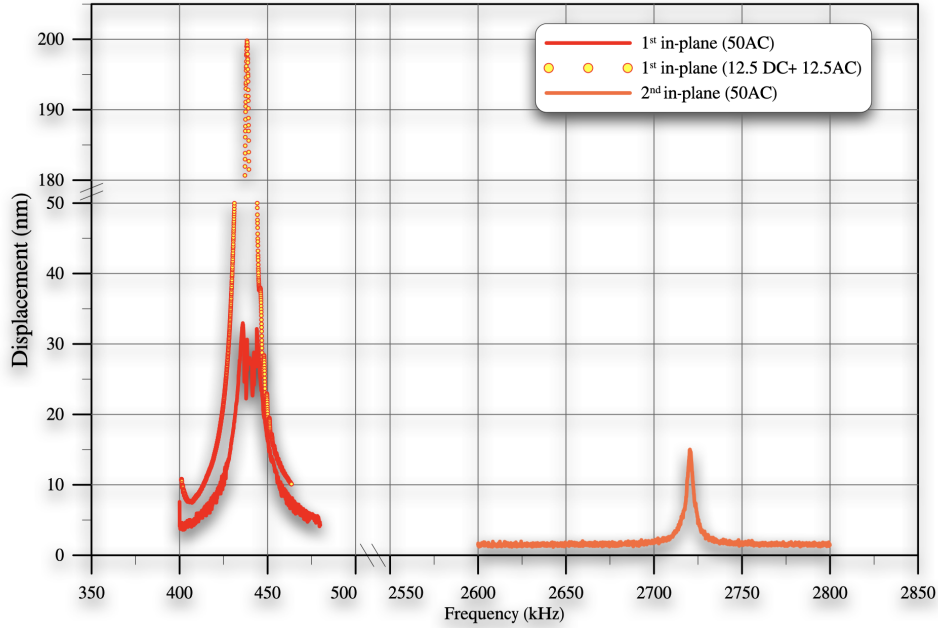
Figure 7.7: Frequency-response curves of the first and second in-plane bending modes..

7.3 Experimental Setup

The electrostatic force for the parallel plate, Eq. 4.4, is proportional to the electrical permittivity. Deionized water (H_2O) has an electrical permittivity (dielectric constant) of 78.5 [107], while air has a permittivity of 1 (vacuum permittivity= 8.854×10^{-12} F/m). This difference in the electrical permittivity amplifies the electrostatic force in testing underwater to $60 - 80$ times of testing in air.

The viscosity of water is higher than air, thus damping increases significantly when submerging the sensor underwater. Accordingly, the sensor's response will be reduced considerably [25]. Furthermore, the added mass of water onto the sensor reduces the response and shifts the system's natural frequencies [25].

Surface tension in case of testing underwater is considerable, which can diminish the MEMS motions [106]. Sometimes the surface tension force can lead to stiction of the micro-structure to the bottom or side electrode.

Some impurities and dust particles flowing in the water can also reduce the gap between the two electrodes or even connect them, increasing the risk of electrical sparks. Thermal

and electrical conductivity were also considered when testing underwater because they are higher in water than in air.

Figure 7.8 shows the experimental setup of testing the underwater sensor underwater. Electrical measurements of the induced current between the two electrodes were used to characterize the behavior of the underwater sensor. Electrical measurements represent an 'integral-type estimate of the overall structure motion rather than a 'point-wise measurement of motion. At the same time, the LDV was used to validate the experimental setup and ensure the validity of each step of the experimental procedure.
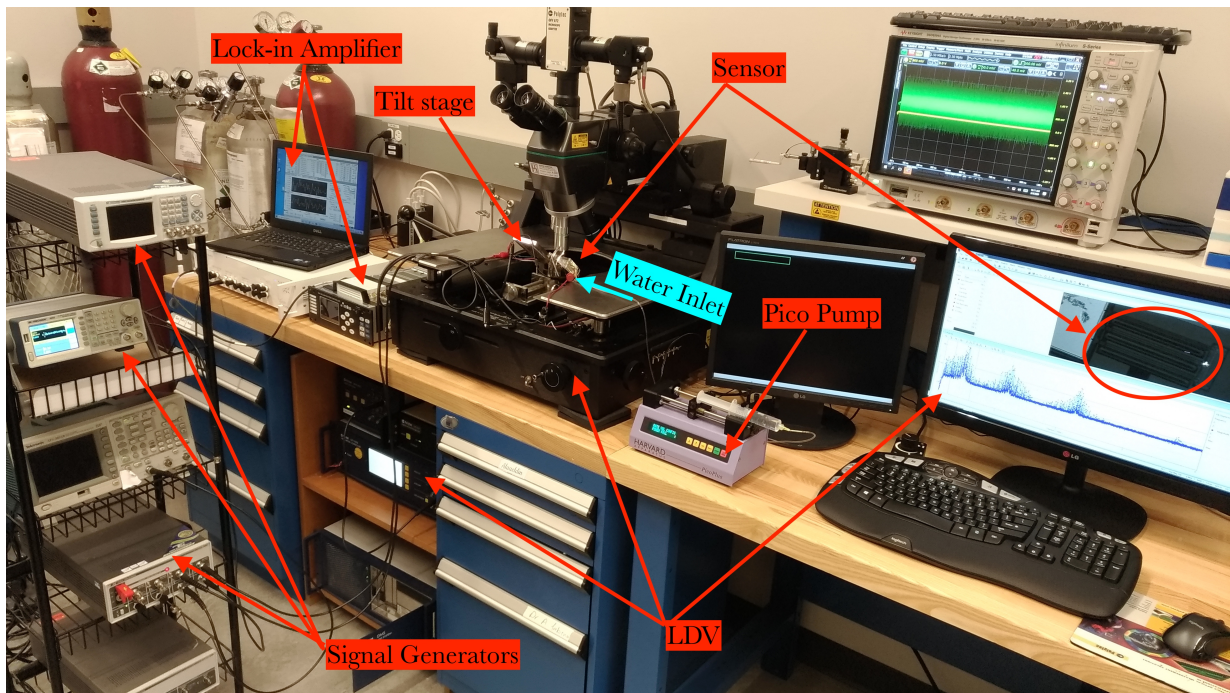
Figure 7.8: Experimental setup of testing the underwater sensor underwater

The sensor is placed in a test chamber made from transparent acrylic to provide optical access to the underwater sensor. The test chamber has a cavity of 6 mL. A microfluidic pump (Pico plus) from Harvard Apparatus [108] was used to pump the water slowly and carefully into the test chamber. A flow rate of 500 μ L/min was used to fill the chamber in 12 minutes. Higher rates of flow can cause stiction of the microbeam to the bottom or side electrodes. The test chamber has an outlet that allows the overflow of water and indicates the fullness of the chamber.

The sensor is connected electrically to the lock-in amplifier, and the induced current

onto the sensor current was amplified using a trans-impedance amplifier, Figure 7.9. A frequency sweep test was conducted on the sensor before and after introducing the water.
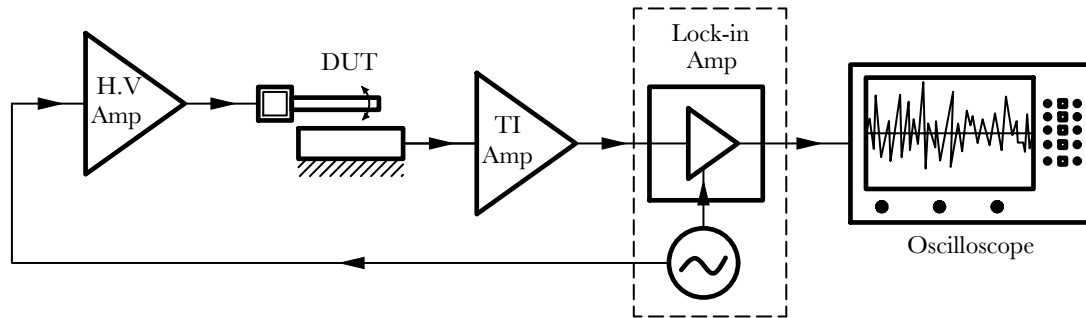
Figure 7.9: Experimental setup for measuring the current of the underwater sensor

The actuation frequency was swept from 1 kHz to 2 MHz. Pure AC loading was used: 25 V amplitude in air and 0.5 V underwater. RMS of the current was recorded and the average of 16 readings was calculated and plotted in Figure 7.10.

In air, the frequency-response curve of the induced current shows a peak in current amplitude at 44 kHz, 110 kHz, and 226 kHz. Those peaks accompanied a noticeable change in the phase diagram. The phase shifts were 73° for the 44 kHz, 144° for the 110 kHz, and 105° for the 226 kHz. Another significant current peak was observed at 3.46 MHz, its value around 1000 times the former peaks values, although no change in the phase diagram was observed. This peak may be an artificial response from the electrical equipment used. Comparing those results with the FEM results of the sensor in Table C.1, we find that those frequencies are almost equal to half of the first, second out-of-plane, and first in-plane natural frequencies.

We suspect that the experimental results of the measured current show the first, second out-of-plane, and first in-plane natural frequencies of the sensor. Although, their phase shifts are not typical at natural frequencies (180°). This may be related to how close they are to each other, in addition to the bandwidth of each natural frequency being wide and intersecting with the other bandwidths.

Testing the sensor underwater resulted in two noticeable peaks in the current amplitudes. The first current peak occurred at 280 kHz, and its corresponding phase shift was
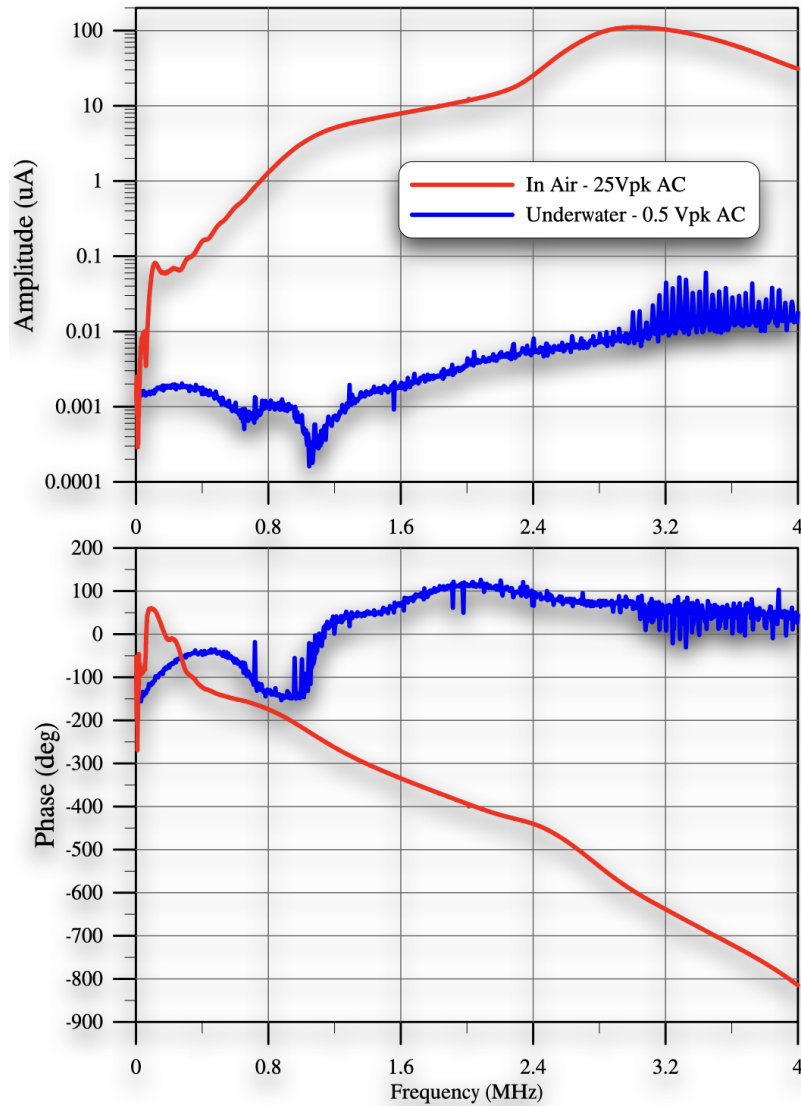
Figure 7.10: Frequency-response curves of the underwater sensor in air and underwater

180°. The second current peak was observed at 916 kHz and the phase shift at this frequency was also 180°. The closest natural frequencies from Table C.1 to those results are the first and second in-plane natural frequencies of the sensor underwater.

By comparing these results with the results of the mathematical model, Section 4.3.5,

we find that the water is damping the sensor's response flattens all sharp peaks in the frequency-response curves of the velocity and displacement.

Chapter 8

Conclusions and Future Work

8.1 Conclusions

8.1.1 Measurement of In-Plane Motions

We demonstrated a technique to measure in-plane motions of MEMS actuators using a typical out-of-plane LDV. It employs a tilt stage to align the sidewalls of MEMS actuators with the incident laser beam. Specifically, we demonstrated the deployment of our technique to measure modal response and frequency-response in-plane successfully.

Further, we compared the validity of using in-plane and out-of-plane measurement techniques to detect predominantly planar response modes. We found that measuring the response of a mode in a plane where it is not active leads to inferior and misleading results. The motions associated with a planar mode that appear outside its dominant plan are spurious, related to fabrication or actuation misalignments. As a result, they are small compared to those occurring in the primary plane of motion and approach a minimum as the frequency of excitation approaches the natural frequency of the mode, thereby concentrating the actuator response in its dominant plane of motion. Therefore, predominantly planar modes should only be observed in their dominant plane. The measurement technique proposed here allows us to achieve that regardless of the plane of motion.

8.1.2 In-Plane Sensor Design

In-plane sensors were designed and fabricated using a custom SOI fabrication process to investigate the performance of four variant sensor designs. The sensors were successfully

fabricated and coated with a metalization layer of gold to prevent dielectric charging. The performance of those sensors was evaluated and is summarized in Table 3.2. The results show that in-plane sensors have higher quality factors than comparable out-of-plane sensors. Further, one-side actuated sensors have higher quality factors than comparable double-side actuated sensors. In addition, cavitary sensors have lower voltage requirements, are more sensitive, and have smaller minimum measurable mass compared to solid sensors. We recommend that in-plane sensor designers forego any advantages that may arise from double-sided actuation in favor of the lower damping provided by one-sided actuation. Instead, they should secure lower actuation voltages by reducing the sensor mass and stiffness via cavitary sensor designs.

8.1.3   Electrostatic Bifurcation In-Plane Sensor Model

A coupled system of nonlinear partial differential equations was solved to investigate the effect of squeeze film damping on the sensor's behavior. An experiment was conducted to check the validity of the mathematical model. Results of the model's static displacement show a good match with the experimental data. EVP was solved for the beam and the pressure. The natural frequencies drop as the electrostatic force increases. The softening behavior was noticed with increasing the bias voltage.

At pressure levels closer to the ambient pressure, the pressure mode shapes show a smooth change in the pressure. At lower pressure, the pressure tends to change quickly, creating a boundary layer at the tip. In this case, a different solution method may be considered. The dynamic response of the beam is similar to the response of the traditional electrostatic MEMS. We noticed a cyclic-fold bifurcation around the primary resonance when the $V_o = 30\,\text{V}$. Another cyclic-fold bifurcation was noticed around the superharmonic resonance when V_o was increased to $40\,\text{V}$. The number of the cyclic-fold bifurcation points was increased further when the harmonic excitation increased. The calculated frequency-response curves of the underwater sensor show almost flat responses because of the very high damping.

8.1.4   Electrostatic Bifurcation Pressure Sensor

A novel electrostatic bifurcation pressure sensor was developed and tested. The sensor consists of a simple microstructure that can easily be fabricated using a multiuser or a custom fabrication process. It does not need wafer bonding, sealing, or any complex microfabrication process. Electrostatic bifurcation pressure sensor overcomes these limitations of

temperature in the other pressure sensors. Unlike the other MEMS pressure sensors, the Electrostatic bifurcation pressure sensor does not need a large area or vacuum cavity to operate. The functional parameters of the bifurcation pressure sensor are independent of the design dimensions of the sensor. It also collects the advantages of low power cost, a wide range of operations.

The results of the frequency-response curves showed that the electrostatic bifurcation in-plane pressure sensor would be more sensitive to the pressure if the cyclic-fold bifurcation mechanism was used as the detection mechanism. There were significant jumps in the phase diagrams at the start and end of the tapping mode oscillation, and we concluded that the phase diagram of the down-sweep is the most sensitive measurement for pressure change. The electrostatic bifurcation in-plane pressure sensor can measure the ambient pressure by measuring the start, end, or bandwidth of the tapping mode oscillation.

8.1.5 Electrostatic Bifurcation Gas Sensor

A static bifurcation MEMS-based gas sensor for detecting low concentrations of three VOCs (formaldehyde, benzene, and hydrogen sulfide) were successfully designed and fabricated using the PolyMUMPs surface micromachining process. The sensor was functionalized by depositing the detector polymers (P25DMA and PANI) onto the sense plate using a new deposition method. A noticeable difference in the sensor's response was observed after depositing the detector polymer. Hydrogen sulfide was detected after 15 minutes of releasing the gas. Different concentrations of formaldehyde and benzene were tested using P25DMA and PANI. We found that PANI could detect the formaldehyde down to 1 ppm in dry nitrogen, and it can detect the benzene down to 2 ppm. On the other hand, P25DMA could detect formaldehyde and benzene down to 5 ppm and 10 ppm respectively. The functionalized sensor with PANI could selectively detect formaldehyde in the presence of benzene as an interferent gas.

8.1.6 Electrostatic Bifurcation Underwater Sensor

An electrostatic bifurcation underwater sensor for detecting mercury has been designed and fabricated using PolyMUMPS processes. The sensor was characterized in air using LDV for both in-plane and out-of-plane motions. The results of modal analysis from the experiment and FEM match. Experimentally proved that the in-plane quality factors are significantly greater than their values for the out-of-plane natural frequencies.

Electrical measurements of the induced current were obtained for the sensor in air and underwater. Two peaks in the current measurements accompanied by $\sim 180°$ phase shift were obtained when the sensor was tested underwater. Those frequencies represent potential targets that can be used in the future for mercury sensing purposes.

8.2   Future Work

8.2.1   Electrostatic Bifurcation In-Plane Sensor Model

The mathematical model should be updated to solve for the damped EVP. Perturbation analysis as a solution method for the problem should be considered when the pressure in the boundary layer at the tip of the cantilever changes rapidly. As a part of the future work, we built the model using perturbation analysis to solve the motion and pressure mode shapes, Appendix A.

8.2.2   Electrostatic Bifurcation Underwater Sensor

Experimentally, the peaks in the frequency-response curve in air and underwater will be investigated optically under the LDV. The sensor will be functionalized with a suitable polymer to detect the mercury underwater. The sensor will be characterized experimentally before and after introducing the mercury to define the detection voltages or the frequency shifts. The results of the experimental tests will be compared to the mathematical results of the model.

References

[1] Sergey Edward Lyshevski. *MEMS and NEMS: systems, devices, and structures*. CRC press, 2002.

[2] M.I. Younis. *MEMS Linear and Nonlinear Statics and Dynamics*. Microsystems. Springer US, 2011.

[3] WG Pfann and RN Thurston. Semiconducting stress transducers utilizing the transverse and shear piezoresistance effects. *Journal of Applied Physics*, 32(10):2008–2019, 1961.

[4] ON Tufte, PW Chapman, and Donald Long. Silicon diffused-element piezoresistive diaphragms. *Journal of Applied Physics*, 33(11):3322–3327, 1962.

[5] Naoki Watanabe. *Fundamental study on wide-bandgap-semiconductor MEMS and photodetectors for integrated smart sensors*. PhD thesis, Kyoto University, 2013.

[6] Robert Bogue. Recent developments in MEMS sensors: A review of applications, markets and technologies. *Sensor Review*, 2013.

[7] S.D. Senturia. *Microsystem Design*. Springer US, 2007.

[8] Stanley Kon, Kenn Oldham, and Roberto Horowitz. Piezoresistive and piezoelectric MEMS strain sensors for vibration detection. In *Sensors and Smart Structures Technologies for Civil, Mechanical, and Aerospace Systems 2007*, volume 6529, page 65292V. International Society for Optics and Photonics, 2007.

[9] Li-Peng Wang, Richard A Wolf, Yu Wang, Ken K Deng, Lichun Zou, Robert J Davis, and Susan Trolier-McKinstry. Design, fabrication, and measurement of high-sensitivity piezoelectric microelectromechanical systems accelerometers. *Journal of microelectromechanical systems*, 12(4):433–439, 2003.

[10] Yoonho Seo, Donghwan Kim, and Neal A Hall. High-temperature piezoelectric pressure sensors for hypersonic flow measurements. In *2019 20th International Conference on Solid-State Sensors, Actuators and Microsystems & Eurosensors XXXIII (TRANSDUCERS & EUROSENSORS XXXIII)*, pages 2110–2113. IEEE, 2019.

[11] Tomás Manzaneque, Víctor Ruiz-Díez, Jorge Hernando-García, Elisabeth Wistrela, Martin Kucera, Ulrich Schmid, and José Luis Sánchez-Rojas. Piezoelectric MEMS resonator-based oscillator for density and viscosity sensing. *Sensors and Actuators A: Physical*, 220:305–315, 2014.

[12] Chunhua Cai, Junyan Tan, Di Hua, Ming Qin, and Nianfang Zhu. Piezoresistive temperature sensors fabricated by a surface micromachining CMOS MEMS process. *Scientific reports*, 8(1):1–11, 2018.

[13] Jiushuai Xu, Maik Bertke, Xiaojing Li, Haibo Mu, Hao Zhou, Feng Yu, Gerry Hamdana, Angelika Schmidt, Heiko Bremers, and Erwin Peiner. Fabrication of ZnO nanorods and Chitosan@ ZnO nanorods on MEMS piezoresistive self-actuating silicon microcantilever for humidity sensing. *Sensors and Actuators B: Chemical*, 273:276–287, 2018.

[14] Hongcai Zhang, Xueyong Wei, Yanyu Ding, Zhuangde Jiang, and Juan Ren. A low noise capacitive MEMS accelerometer with anti-spring structure. *Sensors and Actuators A: Physical*, 296:79–86, 2019.

[15] David Effa, Eihab Abdel-Rahman, and Mustafa Yavuz. Cantilever beam microgyroscope based on frequency modulation. In *2013 IEEE/ASME International Conference on Advanced Intelligent Mechatronics*, pages 844–849. IEEE, 2013.

[16] Md Nahid Hasan, Mark Pallay, and Shahrzad Towfighian. Threshold pressure sensing using parametric resonance in electrostatic MEMS. In *2019 IEEE SENSORS*, pages 1–4. IEEE, 2019.

[17] MS Al-Ghamdi, ME Khater, KME Stewart, Ayman Alneamy, Eihab M Abdel-Rahman, and Alexander Penlidis. Dynamic bifurcation MEMS gas sensors. *Journal of Micromechanics and Microengineering*, 29(1):015005, 2018.

[18] Majed Alghamdi. *Electrostatic MEMS bifurcation sensors*. University of Waterloo, 2018.

[19] Mahmoud Elsayed Khater, Eihab Mohamed Abdel-Rahman, and Ali Hasan Nayfeh. Methods and systems for detection using threshold-type electrostatic sensors, 2010. US Patent App. 12/791,293.

[20] Mahmoud E Khater, Eihab M Abdel-Rahman, and Ali H Nayfeh. A mass sensing technique for electrostatically-actuated MEMS. In *ASME 2009 International Design Engineering Technical Conferences and Computers and Information in Engineering Conference*, pages 655–661. American Society of Mechanical Engineers Digital Collection, 2009.

[21] ME Khater, M Al-Ghamdi, S Park, KME Stewart, EM Abdel-Rahman, A Penlidis, AH Nayfeh, AKS Abdel-Aziz, and M Basha. Binary MEMS gas sensors. *Journal of Micromechanics and Microengineering*, 24(6):065007, 2014.

[22] S.H. Strogatz. *Nonlinear Dynamics and Chaos: With Applications to Physics, Biology, Chemistry, and Engineering*. CRC Press, 2018.

[23] Hadi Yagubizade and Mohammad I Younis. The effect of squeeze-film damping on the shock response of clamped-clamped microbeams. *Journal of dynamic systems, measurement, and control*, 134(1), 2012.

[24] Minhang Bao and Heng Yang. Squeeze film air damping in MEMS. *Sensors and Actuators A: Physical*, 136(1):3–27, 2007.

[25] Majed Al-Ghamdi, Resul Saritas, Katherine Stewart, Alison Scott, Mahmoud Khater, Ayman Alneamy, Ahmad Abdel-Aziz, Hamidreza Nafissi, Eihab Abdel-Rahman, and Alexander Penlidis. Aqueous Media Electrostatic MEMS Sensors. In *2019 20th International Conference on Solid-State Sensors, Actuators and Microsystems & Eurosensors XXXIII (TRANSDUCERS & EUROSENSORS XXXIII)*, pages 1254–1257. IEEE, 2019.

[26] Ashok Kumar Pandey and Rudra Pratap. A comparative study of analytical squeeze film damping models in rigid rectangular perforated MEMS structures with experimental results. *Microfluidics and Nanofluidics*, 4(3):205–218, 2008.

[27] Kuan-Yu Hsieh, Jonathan Lee, and Michael S-C Lu. Design and characterization of a CMOS MEMS capacitive squeeze-film pressure sensor with high sensitivity. In *2020 IEEE 33rd International Conference on Micro Electro Mechanical Systems (MEMS)*, pages 626–629. IEEE, 2020.

[28] Yihan Tao, Xinxin Li, Tiegang Xu, Haitao Yu, Pengcheng Xu, Bin Xiong, and Changzheng Wei. Resonant cantilever sensors operated in a high-Q in-plane mode for real-time bio/chemical detection in liquids. *Sensors and actuators B: Chemical*, 157(2):606–614, 2011.

[29] Luke A Beardslee, Christopher Carron, Kemal S Demirci, Jonathan Lehman, Steven Schwartz, Isabelle Dufour, Stephen M Heinrich, Fabien Josse, and Oliver Brand. In-plane vibration of hammerhead resonators for chemical sensing applications. *ACS sensors*, 5(1):73–82, 2019.

[30] JC Greenwood. Silicon in mechanical sensors. *Journal of Physics E: Scientific Instruments*, 21(12):1114, 1988.

[31] James B Angell, Stephen C Terry, and Phillip W Barth. Silicon micromechanical devices. *Scientific American*, 248(4):44–55, 1983.

[32] W Merlijn van Spengen and Tjerk H Oosterkamp. A sensitive electronic capacitance measurement system to measure the comb drive motion of surface micromachined mems devices. *Journal of micromechanics and Microengineering*, 17(4):828, 2007.

[33] Sangtak Park, Mahmoud Khater, David Effa, Eihab Abdel-Rahman, and Mustafa Yavuz. Detection of cyclic-fold bifurcation in electrostatic MEMS transducers by motion-induced current. *Journal of Micromechanics and Microengineering*, 27(8):085007, 2017.

[34] Eric M Lawrence, Kevin E Speller, and Duli Yu. MEMS characterization using laser Doppler vibrometry. In *Reliability, Testing, and Characterization of MEMS/MOEMS II*, volume 4980, pages 51–63. International Society for Optics and Photonics, 2003.

[35] W. Osten. *Optical Inspection of Microsystems*. Optical Science and Engineering. CRC Press, 2018.

[36] Po-Chih Hung and A S Voloshin. In-plane strain measurement by digital image correlation. *Journal of the Brazilian Society of Mechanical Sciences and Engineering*, 25(3):215–221, 2003.

[37] Christian Rembe, Rishi Kant, and Richard S Muller. Optical measurement methods to study dynamic behavior in MEMS. In *Microsystems Engineering: Metrology and Inspection*, volume 4400, pages 127–138. International Society for Optics and Photonics, 2001.

[38] Man-Geun Kim, Kyoungwoo Jo, Hyuk-Sang Kwon, Wongun Jang, Youngsik Park, and Jong-Hyun Lee. Fiber-optic laser Doppler vibrometer to dynamically measure MEMS actuator with in-plane motion. *Journal of Microelectromechanical Systems*, 18(6):1365–1370, 2009.

[39] KL Turner, P Hartwell, and N MacDonald. Multi-dimensional MEMS motion characterization using laser vibrometry. *Digest of Technical Papers Transducers' 99*, 21, 1999.

[40] MSA-100-3D Micro System Analyzer. https://www.polytec.com/eu/vibrometry/products/microscope-based-vibrometers/msa-100-3d-micro-system-analyzer/. Accessed: 2020-02-12.

[41] Etienne Herth, Franck Lardet-Vieudrin, Florent Deux, Laurie Valbin, Emmanuelle Algré, Jochen Schell, and Heinrich Steger. Detection of out-of-plane and in-plane (XYZ) motions of piezoelectric microcantilever by 3D-Laser Doppler Vibrometry. In *2016 Symposium on Design, Test, Integration and Packaging of MEMS/MOEMS (DTIP)*, pages 1–4. IEEE, 2016.

[42] Robert Kowarsch, Wanja Ochs, Moritz Giesen, Alexander Dräbenstedt, Marcus Winter, and Christian Rembe. Real-time 3D vibration measurements in microstructures. In *Optical Micro-and Nanometrology IV*, volume 8430, page 84300C. International Society for Optics and Photonics, 2012.

[43] PSV-500-3D Scanning Vibrometer. https://www.polytec.com/us/vibrometry/products/full-field-vibrometers/psv-500-3d-scanning-vibrometer/. Accessed: 2020-02-17.

[44] Mary Gopanchuk, Mohamed Arabi, N Nelson-Fitzpatrick, Majed S Al-Ghamdi, Eihab Abdel-Rahman, and Mustafa Yavuz. Characterization of a Non-Interdigitated Comb Drive. In *ASME 2018 International Design Engineering Technical Conferences and Computers and Information in Engineering Conference*, pages V004T08A013–V004T08A013. American Society of Mechanical Engineers, 2018.

[45] Leader in Optical Measurement Equipment - Polytec. https://www.polytec.com/int/. Accessed: 2020-03-19.

[46] J-LA Yeh, C-Y Hui, and Norman C Tien. Electrostatic model for an asymmetric combdrive. *Journal of Microelectromechanical systems*, 9(1):126–135, 2000.

[47] Nouha Alcheikh, Lakshmoji Kosuru, Syed NR Kazmi, and Mohammad I Younis. In-plane air damping of nems and mems resonators. In *2018 IEEE 13th Annual International Conference on Nano/Micro Engineered and Molecular Systems (NEMS)*, pages 225–228. IEEE, 2018.

[48] Mohammad H Hasan, Fadi M Alsaleem, and Hassen M Ouakad. Novel threshold pressure sensors based on nonlinear dynamics of MEMS resonators. *Journal of Micromechanics and Microengineering*, 28(6):065007, 2018.

[49] M. E. Khater, K. Vummidi, E. M. Abdel-Rahman, A. H. Nayfeh, and S. Raman. Dynamic actuation methods for capacitive MEMS shunt switches. *Journal of Micromechanics and Microengineering*, 21(3):035009, 2011.

[50] M. Younis and F. Alsaleem. Exploration of new concepts for mass detection in electrostatically-actuated structures based on nonlinear phenomena. *Journal of Computational and Nonlinear Dynamics*, 4:033108, 2009.

[51] H. Ouakad, H. Al-Qahtani, and M. A. Hawwa. Influence of squeeze-film damping on the dynamic behavior of a curved micro-beam. *Advances in Mechanical Engineering*, 8:1–8, 2016.

[52] Mohammad I Younis and Ali H Nayfeh. Simulation of squeeze-film damping of microplates actuated by large electrostatic load. *Journal of Computational and Nonlinear Dynamics*, 2(3):232–241, 2007.

[53] Ali H Nayfeh and Mohammad I Younis. A new approach to the modeling and simulation of flexible microstructures under the effect of squeeze-film damping. *Journal of Micromechanics and Microengineering*, 14(2):170, 2003.

[54] I Isaac Hosseini, M Moghimi Zand, and M Lotfi. Dynamic pull-in and snap-through behavior in micro/nano mechanical memories considering squeeze film damping. *Microsystem Technologies*, 23(5):1423–1432, 2017.

[55] Fadi M Alsaleem, Mohammad I Younis, and Hassen M Ouakad. On the nonlinear resonances and dynamic pull-in of electrostatically actuated resonators. *Journal of Micromechanics and Microengineering*, 19(4):045013, 2009.

[56] Mehdi Ghommem, Fehmi Najar, Mohamed Arabi, Eihab Abdel-Rahman, and Mustafa Yavuz. A unified model for electrostatic sensors in fluid media. *Nonlinear Dynamics*, 101(1):271–291, 2020.

[57] Fehmi Najar, Mehdi Ghommem, and Abdessattar Abdelkefi. Multifidelity modeling and comparative analysis of electrically coupled microbeams under squeeze-film damping effect. *Nonlinear Dynamics*, 99(1):445–460, 2020.

[58] Ahmed A Shabana and Frederick F Ling. *Vibration of discrete and continuous systems*. Springer, 1997.

[59] Wolfram Mathematica: Modern Technical Computing. https://www.wolfram.com/mathematica/. Accessed: 2021-12-24.

[60] A.H. Nayfeh. *Introduction to Perturbation Techniques*. Wiley Classics Library. Wiley, 2011.

[61] P Eswaran and S Malarvizhi. MEMS capacitive pressure sensors: a review on recent development and prospective. *International Journal of Engineering and Technology (IJET)*, 5(3):2734–2746, 2013.

[62] Vinod Belwanshi and Anita Topkar. Quantitative analysis of temperature effect on SOI piezoresistive pressure sensors. *Microsystem Technologies*, 23(7):2719–2725, 2017.

[63] N Marsi, BY Majlis, AA Hamzah, and F Mohd-Yasin. The mechanical and electrical effects of MEMS capacitive pressure sensor based 3C-SiC for extreme temperature. *Journal of engineering*, 2014, 2014.

[64] Hui-Yang Yu, Ming Qin, Jian-Qiu Huang, and Qing-An Huang. A MEMS capacitive pressure sensor compatible with CMOS process. In *SENSORS, 2012 IEEE*, pages 1–4. IEEE, 2012.

[65] Bian Tian, Yulong Zhao, and Zhuangde Jiang. The novel structural design for pressure sensors. *Sensor Review*, 2010.

[66] Tamas Karpati, Andrea Edit Csikósné Pap, and Sandor Kulinyi. Prototype mems capacitive pressure sensor design and manufacturing. *Periodica Polytechnica Electrical Engineering*, 57(1):3–7, 2013.

[67] Ali H Nayfeh, Mohammad I Younis, and Eihab M Abdel-Rahman. Dynamic pull-in phenomenon in MEMS resonators. *Nonlinear dynamics*, 48(1):153–163, 2007.

[68] Mohammad I Younis, Eihab M Abdel-Rahman, and Ali Nayfeh. A reduced-order model for electrically actuated microbeam-based mems. *Journal of Microelectromechanical systems*, 12(5):672–680, 2003.

[69] Bashar K Hammad, Eihab M Abdel-Rahman, and Ali H Nayfeh. Modeling and analysis of electrostatic mems filters. *Nonlinear Dynamics*, 60(3):385–401, 2010.

[70] F Najar, AH Nayfeh, EM Abdel-Rahman, S Choura, and S El-Borgi. Nonlinear analysis of MEMS electrostatic microactuators: primary and secondary resonances of the first mode. *Journal of Vibration and Control*, 16(9):1321–1349, 2010.

[71] Vamsi C Meesala, Muhammad R Hajj, and Eihab Abdel-Rahman. Bifurcation-based MEMS mass sensors. *International Journal of Mechanical Sciences*, 180:105705, 2020.

[72] Dennis Denney. Control of sulfate-reducing bacteria in oil and gas pipelines. *Journal of Petroleum Technology*, 61(12):78–79, 2009.

[73] Joaquim Rovira, Neus Roig, Martí Nadal, Marta Schuhmacher, and José L Domingo. Human health risks of formaldehyde indoor levels: an issue of concern. *Journal of Environmental Science and Health, Part A*, 51(4):357–363, 2016.

[74] Tee L Guidotti. Hydrogen sulfide: advances in understanding human toxicity. *International journal of toxicology*, 29(6):569–581, 2010.

[75] CH Chou, World Health Organization, et al. *Hydrogen sulfide: human health aspects*. World Health Organization, 2003.

[76] Wei Ying Yi, Kin Ming Lo, Terrence Mak, Kwong Sak Leung, Yee Leung, and Mei Ling Meng. A survey of wireless sensor network based air pollution monitoring systems. *Sensors*, 15(12):31392–31427, 2015.

[77] Rami Mannila, Risto Hyypiö, Marko Korkalainen, Martti Blomberg, Hannu Kattelus, and Anna Rissanen. Gas detection with microelectromechanical fabry-perot interferometer technology in cell phone. In *Next-Generation Spectroscopic Technologies VIII*, volume 9482, page 94820P. International Society for Optics and Photonics, 2015.

[78] Michael Blaschke, Thomas Tille, Phil Robertson, Stefan Mair, Udo Weimar, and Heiko Ulmer. MEMS gas-sensor array for monitoring the perceived car-cabin air quality. *IEEE Sensors Journal*, 6(5):1298–1308, 2006.

[79] Saeb Mousavi, Kyungnam Kang, Jaeho Park, and Inkyu Park. A room temperature hydrogen sulfide gas sensor based on electrospun polyaniline–polyethylene oxide nanofibers directly written on flexible substrates. *RSC advances*, 6(106):104131–104138, 2016.

[80] Iftikhar M Ali, Ahmed M Shano, and Nabeel A Bakr. H_2S gas sensitivity of pani nano fibers synthesized by hydrothermal method. *Journal of Materials Science: Materials in Electronics*, 29(13):11208–11214, 2018.

[81] Kai-Ming Hu, Wen-Ming Zhang, Xi Shi, Han Yan, Zhi-Ke Peng, and Guang Meng. Adsorption-induced surface effects on the dynamical characteristics of micromechanical resonant sensors for in situ real-time detection. *Journal of Applied Mechanics*, 83(8), 2016.

[82] T Thundat, EA Wachter, SL Sharp, and RJ Warmack. Detection of mercury vapor using resonating microcantilevers. *Applied Physics Letters*, 66(13):1695–1697, 1995.

[83] Hendrik Schlicke, Sophia C. Bittinger, Malte Behrens, Mazlum Yesilmen, Hauke Hartmann, Clemens J. Schröter, Gregor T. Dahl, and Tobias Vossmeyer. Electrostatically actuated membranes of cross-linked gold nanoparticles: Novel concepts for electromechanical gas sensors. *Proceedings*, 1(4), 2017.

[84] V Dam, D Wouters, W Knoben, SH Brongersma, and R van Schaijk. Polymer coated MEMS resonator for room temperature NH3 sensing. In *IEEE Sensors*, pages 194–197. IEEE, 2014.

[85] Sangjun Park, Inug Yoon, Sungwoo Lee, Hyojung Kim, Ji-Won Seo, Yoonyoung Chung, Alexander Unger, Mario Kupnik, and Hyunjoo J Lee. CMUT-based resonant gas sensor array for VOC detection with low operating voltage. *Sensors and Actuators B: Chemical*, 273:1556–1563, 2018.

[86] Maira Possas-Abreu, Farbod Ghassemi, Lionel Rousseau, Emmanuel Scorsone, Emilie Descours, and Gaelle Lissorgues. Development of diamond and silicon mems sensor arrays with integrated readout for vapor detection. *Sensors*, 17(6):1163, 2017.

[87] Vijay Kumar, Yushi Yang, J William Boley, George T-C Chiu, and Jeffrey F Rhoads. Modeling, analysis, and experimental validation of a bifurcation-based microsensor. *Journal of microelectromechanical systems*, 21(3):549–558, 2012.

[88] Allen Cowen, Busbee Hardy, Ramaswamy Mahadevan, and Steve Wilcenski. Poly-MUMPs design handbook. *MEMSCAP Inc.: Durham, NC, USA*, 2011.

[89] COMSOL: Multiphysics Software for Optimizing Designs. https://www.comsol.com/. Accessed: 2020-03-19.

[90] G Müller, A Friedberger, P Kreisl, S Ahlers, O Schulz, and T Becker. A MEMS toolkit for metal-oxide-based gas sensing systems. *Thin Solid Films*, 436(1):34–45, 2003.

[91] Terry L Miller and MJ380188 Wolin. A serum bottle modification of the hungate technique for cultivating obligate anaerobes. *Applied microbiology*, 27(5):985–987, 1974.

[92] JR Postgate. *The sulphate-reducing bacteria*. Cambridge University Press, 1984.

[93] Flemming Vester and Kjeld Ingvorsen. Improved most-probable-number method to detect sulfate-reducing bacteria with natural media and a radiotracer. *Applied and Environmental Microbiology*, 64(5):1700–1707, 1998.

[94] Katherine ME Stewart and Alexander Penlidis. Designing polymeric sensing materials for analyte detection and related mechanisms. In *Macromolecular Symposia*, volume 360, pages 123–132. Wiley Online Library, 2016.

[95] Derek CG Muir, R Wagemann, BT Hargrave, David J Thomas, DB Peakall, and RJ Norstrom. Arctic marine ecosystem contamination. *Science of the Total Environment*, 122(1-2):75–134, 1992.

[96] Raphael A Lavoie, Ariane Bouffard, Roxane Maranger, and Marc Amyot. Mercury transport and human exposure from global marine fisheries. *Scientific reports*, 8(1):6705, 2018.

[97] Giuseppe Genchi, Maria Stefania Sinicropi, Alessia Carocci, Graziantonio Lauria, and Alessia Catalano. Mercury exposure and heart diseases. *International journal of environmental research and public health*, 14(1):74, 2017.

[98] UNEP Chemicals Branch. The global atmospheric mercury assessment: Sources. *Emissions and Transport, Geneva: UNEP-Chemicals*, 2008.

[99] U.S. Environmental Protection Agency. *2014 National Emissions Inventory, version 2 Technical Support Document*. U.S. Environmental Protection Agency, 2018.

[100] Environment and Climate Change Canada. Canadian mercury science assessment: summary of key results, February 2016.

[101] Isabelle Dufour, Fabien Josse, Stephen M Heinrich, Claude Lucat, Cédric Ayela, Francis Ménil, and Oliver Brand. Unconventional uses of microcantilevers as chemical

sensors in gas and liquid media. *Sensors and Actuators B: Chemical*, 170:115–121, 2012.

[102] MEMS Pro. https://www.softmems.com/mems_pro.html. Accessed: 2020-02-04.

[103] Contour Elite I - Overview. https://www.bruker.com/products/surface-and-dimensional-analysis/3d-optical-microscopes/3d-surface-metrology/contour-elite-i/overview.html. Accessed: 2020-03-19.

[104] 50 MHz Lock-in Amplifier | Zurich Instruments. https://www.zhinst.com/americas/products/hf2li-lock-amplifier. Accessed: 2020-03-19.

[105] S.S. Zumdahl and D.J. DeCoste. *Chemical Principles*. Cengage Learning, 2016.

[106] Dan Sameoto, Ted Hubbard, and Marek Kujath. Operation of electrothermal and electrostatic MUMPs microactuators underwater. *Journal of Micromechanics and Microengineering*, 14(10):1359, 2004.

[107] Andrew P Gregory and RN Clarke. *Tables of the complex permittivity of dielectric reference liquids at frequencies up to 5 GHz*. National Physical Laboratory, 2012.

[108] Standard Infuse/Withdraw Pump 11 Pico Plus Elite Programmable Syringe Pump - Microfluidics - Syringe Pumps - Pumps. https://www.harvardapparatus.com/pumps-liquid-handling/syringe-pumps/microfluidics/standard-infuse-withdraw-pump-11-pico-plus-elite-programmable-syringe-pump.html. Accessed: 2020-03-24.

[109] Abdelhamid Maali, Cedric Hurth, Rodolphe Boisgard, Cédric Jai, Touria Cohen-Bouhacina, and Jean-Pierre Aimé. Hydrodynamics of oscillating atomic force microscopy cantilevers in viscous fluids. *Journal of Applied Physics*, 97(7):074907, 2005.

[110] Mohamed Youssry, Naser Belmiloud, Benjamin Caillard, Cédric Ayela, Claude Pellet, and Isabelle Dufour. A straightforward determination of fluid viscosity and density using microcantilevers: From experimental data to analytical expressions. *Sensors and Actuators A: Physical*, 172(1):40–46, 2011.

Appendix A

Boundary-Layer Problem

A.1 Sensor Model

The sensor structure is described in section 4.1 and Figure 4.1. Following Euler-Bernoulli beam assumptions and accounting for the added mass A_m, linear viscous damping $\hat{c}\dot{w}$, and nonlinear damping of the fluid $\bar{P}(\hat{x}, \hat{t})h$, the equation of motion governing the in-plane deflection $\hat{w}(\hat{x}, \hat{t})$ of the electrostatic sensor, depending on the operating mode is given by

$$\left(\rho b h (1 + A_m)\right)\frac{\partial^2 \hat{w}(\hat{x}, \hat{t})}{\partial \hat{t}^2} + \hat{c}\frac{\partial \hat{w}(\hat{x}, \hat{t})}{\partial \hat{t}} + EI\frac{\partial^4 \hat{w}(\hat{x}, \hat{t})}{\partial \hat{x}^4} = F_e - \bar{P}(\hat{x}, \hat{z}, \hat{t})h \qquad (A.1)$$

subjected to two boundary conditions at the fixed-end:

$$\hat{w}(0, \hat{t}) = 0 \qquad \text{and} \qquad \frac{\partial \hat{w}(0, \hat{t})}{\partial \hat{x}} = 0 \qquad (A.2)$$

and two boundary conditions at the free-end:

$$\frac{\partial^2 \hat{w}(l, \hat{t})}{\partial \hat{x}^2} = 0 \qquad \text{and} \qquad \frac{\partial^3 \hat{w}(l, \hat{t})}{\partial \hat{x}^3} = 0 \qquad (A.3)$$

where ρ is the microbeam density, E is Young's modulus, I is the second moment of area of the beam, and A_m is the added mass, and c is the linear viscous damping coefficient. The added mass and the linear viscous damping coefficient are given by [109]

$$A_m = \frac{1}{\rho b h} \frac{\pi \rho_f h^2}{4} \left(a_1 + a_2 \sqrt{\frac{2\eta_{eff}}{2\pi \rho_f f h^2}} \right)$$

$$c = \frac{\pi \rho_f h^2}{4} 2\pi f \left(b_1 \sqrt{\frac{2\eta_{eff}}{2\pi \rho_f f h^2}} + b_2 \frac{2\eta_{eff}}{2\pi \rho_f f h^2} \right)$$

(A.4)

where $a_1 = 1.0553$, $a_2 = 3.7997$, $b_1 = 3.8018$, and $b_2 = 2.7364$, ρ_f and η_{eff} are the density and viscosity of the fluid, respectively, and f is the natural frequency of the sensor. The latter is obtained by solving the nonlinear algebraic equation [110]

$$f - \frac{f_v}{\sqrt{1 + A_m}} = 0$$

(A.5)

where $f_v = \frac{\beta^2}{2\pi l^2} \sqrt{\frac{EI}{\rho b h}}$ is the sensor natural frequency in vacuum and the mode number β. The electrostatic force term (F_e) in eq A.1 can be calculated as:

$$F_e = \frac{\epsilon_r \epsilon_\circ h V^2}{2(d - \hat{w}(\hat{x}, \hat{t}))} \left(1 + \frac{0.65}{h} (d - \hat{w}(\hat{x}, \hat{t})) \right)$$

(A.6)

where $\epsilon_\circ$ and ϵ_r are the permittivities of the vacuum and the viscous medium, respectively. The squeeze-film damping force, $\bar{P}$ is governed by the two-dimensional compressible Reynolds equation

$$\frac{\partial}{\partial \hat{x}} \left(H^3(\hat{x}, \hat{t}) \bar{P}(\hat{x}, \hat{z}, \hat{t}) \frac{\partial \bar{P}(\hat{x}, \hat{z}, \hat{t})}{\partial \hat{x}} \right) + \frac{\partial}{\partial \hat{z}} \left(H^3(\hat{x}, \hat{t}) \bar{P}(\hat{x}, \hat{z}, \hat{t}) \frac{\partial \bar{P}(\hat{x}, \hat{z}, \hat{t})}{\partial \hat{z}} \right)$$
$$= 12 \, \eta_{eff} \left(H(\hat{x}, \hat{t}) \frac{\partial \bar{P}(\hat{x}, \hat{z}, \hat{t})}{\partial \hat{t}} + \bar{P}(\hat{x}, \hat{z}, \hat{t}) \frac{\partial H(\hat{x}, \hat{w})}{\partial \hat{t}} \right)$$

(A.7)

where $\bar{P}$ is the absolute pressure and H is the variable distance between the beam and the side electrode. The pressure equation is subjected to zero flux at the fixed edge and trival pressure boundary conditions at the free ends:

$$\frac{\partial \bar{P}(0, \hat{z}, \hat{t})}{\partial \hat{x}} = 0$$
$$\bar{P}(l, \hat{z}, \hat{t}) = P_a$$
$$\bar{P}(\hat{x}, 0, \hat{t}) = P_a \tag{A.8}$$
$$\bar{P}(\hat{x}, h, \hat{t}) = P_a$$

where P_a is the surrounding pressure. In the case of working in air, P_a is the atmospheric pressure. H and $\bar{P}$ can be expressed as

$$H(\hat{x}, \hat{t}) = d - \hat{w}(\hat{x}, \hat{t})$$
$$\bar{P}(\hat{x}, \hat{z}, \hat{t}) = P_a + \hat{P}(\hat{x}, \hat{z}, \hat{t}) \tag{A.9}$$

The in-plane displacement of the sensor $\hat{w}(\hat{x}, \hat{t})$ can be decomposed into a static displacement $(\hat{w}_s(\hat{x}))$ and dynamic displacement $\hat{u}(\hat{x}, \hat{t})$.

$$\hat{w}(\hat{x}, \hat{t}) = \hat{w}_s(\hat{x}) + \hat{u}(\hat{x}, \hat{t}) \tag{A.10}$$

The pressure equation can be linearized by substituting Eqs. A.9 and A.10 into A.7 and A.8 and dropping the nonlinear terms. The linearized pressure equation can be written as

$$\frac{\partial^2}{\partial \hat{x}^2} \bar{P}(\hat{x}, \hat{z}, \hat{t}) + \frac{\partial^2}{\partial \hat{z}^2} \bar{P}(\hat{x}, \hat{z}, \hat{t}) = \frac{12 \, \eta_{eff}}{p_a d^3} \left(d \frac{\partial \bar{P}(\hat{x}, \hat{z}, \hat{t})}{\partial \hat{t}} + p_a \frac{\partial \hat{w}(\hat{x}, \hat{t})}{\partial \hat{t}} \right) \tag{A.11}$$

$$\frac{\partial \bar{P}(0, \hat{z}, \hat{t})}{\partial \hat{x}} = 0$$
$$\bar{P}(l, \hat{z}, \hat{t}) = 0$$
$$\bar{P}(\hat{x}, h, \hat{t}) = 0 \tag{A.12}$$
$$\bar{P}(\hat{x}, 0, \hat{t}) = 0$$

Next, we introduce the following parameters to nondimensionalize the system of governing equations.

112

$$x = \frac{\hat{x}}{l}, \ z = \frac{\hat{z}}{l}, \ w = \frac{\hat{w}}{d}, \ t = \frac{\hat{t}}{\tau}, \ P = \frac{\hat{P}}{P_a}, \ \tau = \sqrt{\frac{\rho b h l^4}{EI}} \tag{A.13}$$

The system of governing equations in dimensionless form can be written as:

$$(1 + A_m)\frac{\partial^2 w}{\partial t^2} + C\frac{\partial w}{\partial t} + \frac{\partial^4 w}{\partial x^4} = \alpha_1 V^2 \frac{1 + \alpha_2(1 - w)}{(1 - w)^2} - \alpha_p P \tag{A.14}$$

subjected to the following boundary conditions:

$$
\begin{aligned}
w(0, t) &= 0 \\
\frac{\partial w(0, t)}{\partial x} &= 0 \\
\frac{\partial^2 w(1, t)}{\partial x^2} &= 0 \\
\frac{\partial^3 w(1, t)}{\partial x^3} &= 0
\end{aligned}
\tag{A.15}
$$

and

$$\frac{\partial^2}{\partial x^2}P(x, z, t) + \frac{\partial^2}{\partial z^2}P(x, z, t) = \sigma\left(\frac{\partial P(x, z, t)}{\partial t} + \frac{\partial w(x, t)}{\partial t}\right) \tag{A.16}$$

subjected to two boundary conditions:

$$
\begin{aligned}
\frac{\partial P(0, z, t)}{\partial x} &= 0 \\
P(1, z, t) &= 0 \\
P(x, 0, t) &= 0 \\
P(x, h/l, t) &= 0
\end{aligned}
\tag{A.17}
$$

where:

$$C = \frac{cl^4}{EI\tau}, \ \alpha_1 = \frac{6\epsilon_r\epsilon_o l^4}{Eb^3 d^3}, \ \alpha_2 = 0.65\frac{d}{b}, \ \alpha_p = \frac{P_a l^4 h}{EId}, \ \sigma = \frac{12\eta_{eff} l^2}{P_a \tau d^2} \tag{A.18}$$

113

A.1.1 Linear EVP

To derive the linear eigenvalue problem, we drop the nonlinear and forcing terms in Equation A.14 and obtain

$$\frac{\partial^4 u}{\partial x^4} + \alpha_3 P = (1 + A_m)\frac{\partial^2 u}{\partial t^2} \tag{A.19}$$

$$
\begin{aligned}
u(0) &= 0 \\
\frac{du(0)}{dx} &= 0 \\
\frac{d^2 u(1)}{dx^2} &= 0 \\
\frac{d^3 u(1)}{dx^3} &= 0
\end{aligned}
\tag{A.20}
$$

The pressure equation and its corresponding boundary condition will not change. Assume the solution in the form:

$$
\begin{aligned}
u(x,t) &= \phi(x)e^{i\omega_n t} \\
P(x,t) &= \psi(x)e^{i\omega_n t}
\end{aligned}
\tag{A.21}
$$

where $\phi(x)$ and $\psi(x)$ are the nth mode shapes of the beam and the pressure, respectively, and ω_n is the corresponding non-dimensional natural frequency. Next, we substitute equationsA.21 into equations A.19, A.20, A.16, and A.17 to obtain

$$\phi_n^{(4)}(x) + \alpha_3\psi_n(x,z) = -\omega_n^2(1 + A_m)\phi_n(x) \tag{A.22}$$

$$
\begin{aligned}
\phi_n(0) &= 0 \\
\phi_n'(0) &= 0 \\
\phi_n''(1) &= 0 \\
\phi_n^{(3)}(1) &= 0
\end{aligned}
\tag{A.23}
$$

114

$$\frac{\partial}{\partial x}\Big[\psi'_n(x,z)\Big] + \frac{\partial}{\partial z}\Big[\psi'_n(x,z)\Big] = i\omega_n\sigma\Big[\psi_n(x,z) - \phi_n(x)\Big] \tag{A.24}$$

$$\begin{aligned} \psi'_n(0,z) &= 0 \\ \psi_n(1,z) &= 0 \\ \psi_n(x,0) &= 0 \\ \psi_n(x,h/l) &= 0 \end{aligned} \tag{A.25}$$

A.1.2 Perturbation Analysis

Divide Eq. A.24 by $\omega_n\sigma$ we get

$$\epsilon\frac{\partial^2\psi_n}{\partial x^2} + \epsilon\frac{\partial^2\psi_n}{\partial z^2} = i(\psi_n - \phi_n) \tag{A.26}$$

Where $\epsilon = 1/\omega_n\sigma$. Applying the perturbation method, we assume

$$\begin{aligned} \psi_n &= \psi_0 + \epsilon\psi_1 \\ \phi_n &= \phi_0 + \epsilon\phi_1 \end{aligned} \tag{A.27}$$

By substituting from Eq. A.27 into Eq. A.26 and comparing the coefficients of ϵ^0, we get the outer expansion as:

$$\psi_n = \phi_n \tag{A.28}$$

Eq. A.28 satisfy the boundary conditions at fixed support ($x = 0$) but it does not satisfy the other boundary conditions. To get the inner expansion at $z = 0$. We expand the z by using $\zeta = \frac{z}{\sqrt{\epsilon}}$. We substitute into Eq. A.26 and comparing the coefficients of ϵ^0, we get

$$\frac{\partial^2\psi_0}{\partial\zeta^2} = i(\psi_0 - \phi_0) \tag{A.29}$$

Solving Eq. A.29 and applying the boundary condition at $z = 0$, we get

$$\psi^i(x, z) = \phi(x) - \phi(x)e^{-\left(\frac{1+i}{\sqrt{2}}\right)\varsigma} \tag{A.30}$$

We repeat the same procedure for the boundary condition at $z = h/l$. Expanding this region by using $\xi = \frac{h/l - z}{\sqrt{\epsilon}}$, we get

$$\psi^i(x, z) = \phi(x) - \phi(x)e^{-\left(\frac{1+i}{\sqrt{2}}\right)\xi} \tag{A.31}$$

Expanding this region around $x = 1$ by using $\beta = \frac{1-x}{\sqrt{\epsilon}}$, we get

$$\psi^i(x, z) = \phi(x) - \phi(x)e^{-\left(\frac{1+i}{\sqrt{2}}\right)\beta} \tag{A.32}$$

The total solution of the pressure mode shapes can be obtained by collecting the outer solution with the three inner solutions as

$$\psi^i(x, z) = \phi(x) - \phi(x)e^{-\left(\frac{(1+i)(1-x)}{\sqrt{2\epsilon}}\right)} - \phi(x)e^{-\left(\frac{(1+i)z}{\sqrt{2\epsilon}}\right)} - \phi(x)e^{-\left(\frac{(1+i)(h/l-z)}{\sqrt{2\epsilon}}\right)} \tag{A.33}$$

A.2   Results

Figures A.1, A.2, and A.3 show the first pressure mode shape from different perspectives.
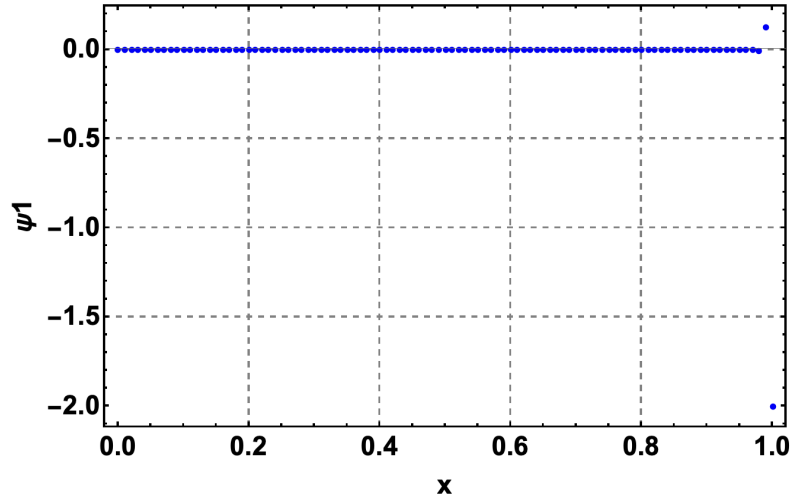
116

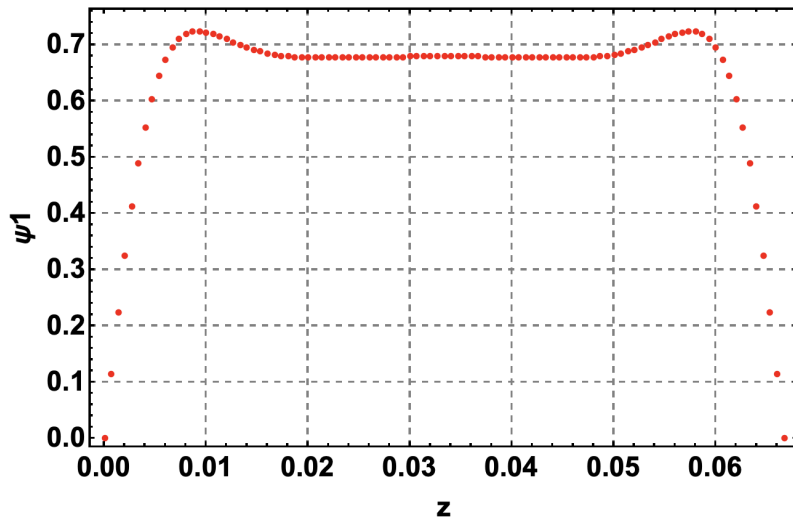Figure A.1: First pressure mode shape along x while $z = h/2l$

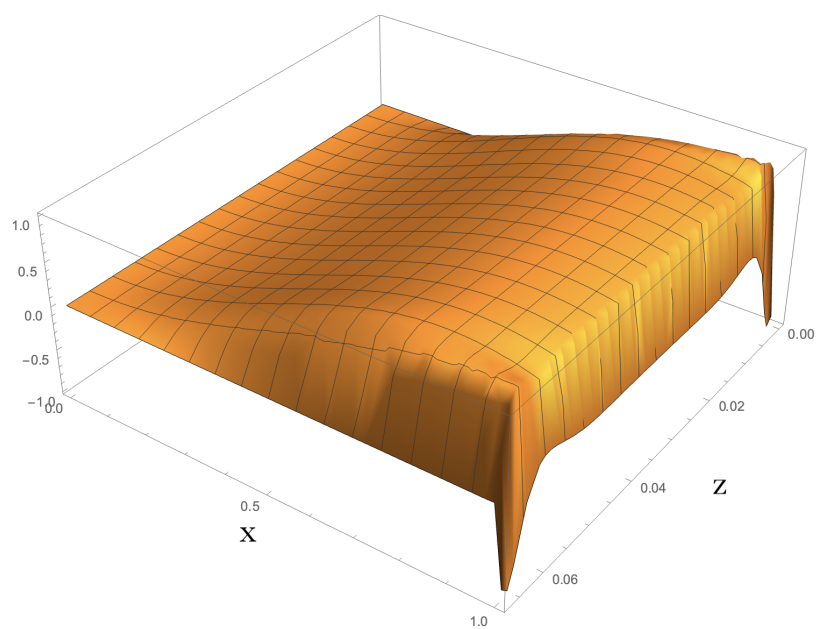Figure A.2: First pressure mode shape along z while $x = 0.5$

117

Figure A.3: First mode shape of the pressure (3D)

Appendix B

PolyMUMPs

PolyMMUMPS is a standard multiuser surface micromachining process. It consists of three structural layers of polysilicon(Poly0, Poly1, and Poly2) on top of silicon nitride layer which acts as an electrical isolation layer. Two Phosphosilicate Glass (PSG) layers are used as sacrificial layers between the structural layers. A layer of gold can be deposited on top of the poly2 layer. Thus the process consists of seven layers and twelve masks as described in tables B.1 and B.2.

Table B.1: Thicknesses of the structural and sacrificial layers of PolyMUMPS are arranged in order from the base to the top layer

Layer number	Material Layer	Thickness (μm)
1	Nitride	0.6
2	Poly0	0.5
3	Oxide1	2.0
4	Poly1	2.0
5	Oxide2	0.75
6	Poly2	1.5
7	Metal	0.5

The fabrication process starts with a wafer which is covered by a silicon nitride layer. Then subsequent fabrication steps of depositing, etching, and metal off are carried out on the wafer to reach the final MEMS structure. Table B.3 shows PolyMUMPs fabrication steps.

Table B.2: PolyMUMPS masks arranged in order of utilization during the fabrication process

Mask number	Name	Type
1	Poly0	Light
2	Hole0	Dark
3	Dimple	Dark
4	Anchor1	Light
5	Poly1	Dark
6	Hole1	Dark
7	Poly1_Poly2_Via	Light
8	Anchor2	Light
9	Poly2	Dark
10	Hole2	Dark
11	Metal	Dark
12	HoleM	Dark

Table B.3: Procedure of the PolyMUMPS process and the masks used in each step

Step number	Description	Mask Name
1	Wafer	–
2	Nitride	–
3	Deposit Poly0	–
4	Etch Poly0	Poly0
5	Etch holes in Poly0	Hole0
6	Deposit Oxide1	–
7	Etch Dimple	Dimple
8	Etch Anchor1	Anchor1
9	Deposit Poly1	–
10	Etch Poly1	Poly1
11	Etch holes in Poly1	Hole1
12	Deposit Oxide2	–
13	Etch Poly1_Poly2_Via	Poly1_Poly2_Via
14	Etch Anchor2	Anchor2
15	Deposit Poly2	–
16	Etch Poly2	Poly2
17	Etch holes in Poly2	Hole2
18	Deposit Metal	–
19	Metal lift off	Metal
20	Open holes in the metal	HoleM
21	Sacrificial etch	–

Appendix C

Underwater sensor: Second Generation Prototype

After testing the original design of the underwater sensor, it was noted that the sensor's response (peaks of velocity and displacement) was small. The stiction problem was affecting most of the sensors on the chip even without external excitation. The cantilever top surface's area wasn't large enough to carry an appropriate amount of the detecting polymer. So, a new design for the underwater sensor was implemented to update the original design and overcome its limitation. The second generation of the underwater sensors was designed to meet the following criteria.

First, increasing the sensor's response under low actuation voltages. To do this, we increased the parallel plate surface area by replacing the microcantilever with three microcantilevers facing three side electrodes. This will amplify the actuation force by about three times its original value in the original design. Second, a sense plate was added at the free end of the cantilever. The sense plate was made from Poly1, and a frame of Poly2 was deposited onto it to improve its capacity for carrying detector polymer. The sense plate was designed to be $120\,\mu$m length and $30\,\mu$m width. Finally, ten small dimples were added underneath the sense plate to prevent the plate from sticking to the substrate. The second generation of the underwater sensors is shown in Figure C.1.

A FEM modal analysis of the sensor was carried out using the same procedure described in Section 7.1.2. The statistics of the mesh were 16079 tetrahedral elements, 10857 triangular elements, 3279 edge elements, and 272 vertex elements. The minimum element size was 1.5μm. The FEM solver solved for 96042 DOF, and the first 50 eigenfrequencies were calculated.
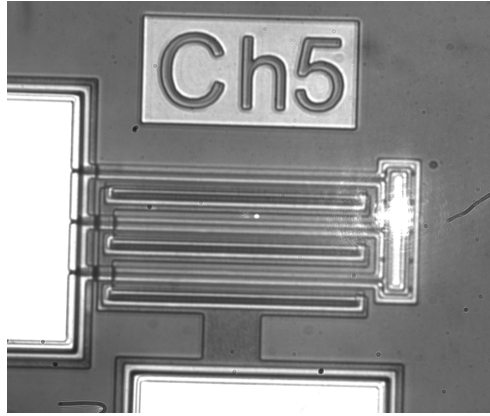
Figure C.1: Second-generation of the underwater sensors

Because the second generation of the underwater sensor has three microcantilevers instead of one, we found that many mode shapes were moving only one or two microcantilevers. The results of the FEM simulation are summarized in Table C.1 and only contain the natural frequencies that correspond to whole structure motion.

Table C.1: Natural frequencies of the second generation sensors

	Out-of-plane (MHz)	In-plane (MHz)	Twisting(MHz)
1	0.0705	0.288	0.220
2	0.545	1.87	5.4
3	1.61	4.68	10.9
4	3.17	9.47	
5	5.132	14.7	
6	7.49		

Glossary

COMSOL a cross-platform finite element analysis, solver and multiphysics simulation software xv, 19, 52, 72, 83

MEMSPro a computer-aided design tool suite for the design and analysis of MicroElectroMechanical System xv, 72, 83

Piranha/RCA a standard set of wafer cleaning steps needed before the microfabrication process xv, 20

PolyMUMPs a standard multiuser surface micromachining process. It consists of three structural layers of polysilicon(Poly0, Poly1, and Poly2) on top of the silicon nitride layer, which acts as an electrical isolation layer. The main features of the PolyMUMPS are summarized in Appendix B xv, 72, 83, 97

SolidWorks a solid modeling computer-aided design and computer-aided engineering program published by Dassault Systèmes xv, 8